Theoretical Study of Gilbert Damping and Spin Dynamics in Spintronic Devices

A DISSERTATION

SUBMITTED TO THE FACULTY OF THE GRADUATE SCHOOL

OF THE UNIVERSITY OF MINNESOTA

BY

Tao Qu

IN PARTIAL FULFILLMENT OF THE REQUIREMENTS

FOR THE DEGREE OF

Doctor of Philosophy

Randall H. Victora

August, 2017

Acknowledgements

There are many people that have earned my gratitude for their contribution to my time in graduate school. I would like to use this opportunity to express my sincere thanks to those people who have supported and advised me during my Doctoral study.

I would like to extend by deepest appreciation to Prof. Victora. As a thesis advisor, he teaches me not only the knowledge of spintronic physics, but also the way to explore the new area and the ability to solve open questions. As a friend, he gives me invaluable support in all the difficult times I went through. Without his guidance and encouragement, I would never struggle through the dilemma and gone this far.

During my stay at the Universifty of Minnesota, I have also received much help and advice from Prof. Allen Goldman and Prof. Jianping Wang. They demonstrate a selfless commitment to furthering the best interests of the students.

For this, I am greatly indebted to them.

I am also very thankful to my committee members, Prof. Paul Crowell, Prof. Allen Goldman and Prof. Jorge Vinals for their valuable advices and suggestions to my projects in both my thesis preliminary and final oral exams.

I want to thank all the friends in Physics and Electrical engineering department. I enjoy all the interdiscipline conversations that open another view point of my project.

Lastly, I want to express my love and thanks to my family. They stay by my side at every challenge I faced.

I have a lot of good memories in University of Minnesota. It is my honor and privilege to be a student in University of Minnesota.

Dedication

To my family, as heaven maintains vigor through movements, I should constantly

strive for self-perfection

Abstract

The determination of damping mechanisms is one of the most fundamental problems of magnetism. It represents the elimination of the magnetic energy and thus has broad impact in both science and technology. The dynamic time scale in spintronic devices is controlled by the damping and the consumed power depends on the damping constant squared. In recent years, the interest in high perpendicular anisotropy materials and thin film structures have increased considerably, owing to their stability over a wide temperature range when scaling devices to nanometer length scales. However, the conventional measurement method-Ferromagnetic resonance (FMR) can not produce accurate damping results in the high magnetic crystalline anisotropy materials/structures, and the intrinsic damping reported experimentally diverges among investigators, probably due to the varying fabrication techniques. This thesis describes the application of the Kambersky torque correlation technique, within the tight binding method, to multiple materials with high perpendicular magnetic anisotropy ($\sim 10^7$ erg/cm^3), in both bulk and thin film structures. The impact of the inevitable experimental defects on the energy dissipation is identified and the experimental damping divergence among investigators due to the material degree of order is explained. It is demonstrated that

this corresponds to an enhanced DOS at the Fermi level, owing to the rounding of the DOS with loss of long-range order. The consistency of the predicted damping constant with experimental measurement is demonstrated and the interface contribution to the energy damping constant in potential superlattices and heterostructures for spintronic devices is explored. An optimized structure will be a tradeoff involving both anisotropy and damping.

The damping related spin dynamics in spintronic devices for different applications is investigated. One device is current perpendicular to planes(CPP) spin valve. Incoherent scattering matrices are applied to calculate the angle dependent magnetoresistantce and obtain analytic expressions for the spin valve. The non-linearity of magnetoresistance can be quantitatively explained by reflected electrons using only experimental spin polarization as input. The other device is a spin-transfer-torque nano-oscillator. The Landau-Lifshitz-Gilbert equation is applied and the synchronization requirement for experimentally fabricated non-identical multi spintronic oscillators is explored. Power enhancement and noise decrease for the synchronized state is demonstrated in a temperature range. Through introducing combined electric and magnetic coupling effect, a design for an optimized feasible nanopillar structure suitable for thin-film deposition is developed.

Contents

List of Tables

List of Figures

xix

Chapter 1

Introduction

1.1 Spin and Ferromagnetism

Spin is an internal degree of freedom of an electron that gives rise to its intrinsic magnetic moment, measured in Bohr magneton (μ_B=0.927×10^{-20} erg/Oe). Through the spin-orbit interaction(SOI), both spin and orbital moments can contribute to the total magnetism of an atom. In solid state materials, electrons interact with each other under two basic principles: the Coulomb repulsion between electrons and the constraints imposed by the Pauli exclusion principle. The electron-electron interaction Hamiltonian can be written as 1.1[12].

$$H_{ee} = \sum_{\boldsymbol{k}\sigma} \left(\frac{\hbar^2 k^2}{2m} \right) c_{\boldsymbol{k}\sigma}^+ c_{\boldsymbol{k}\sigma} + \frac{1}{2} \sum_{\boldsymbol{k},\boldsymbol{k}',\boldsymbol{q}} V_{\boldsymbol{q}} c_{\boldsymbol{k}+\boldsymbol{q}\sigma}^+ c_{\boldsymbol{k}'-\boldsymbol{q}\sigma'}^+ c_{\boldsymbol{k}\sigma} c_{\boldsymbol{k}'\sigma'} \quad , \qquad (1.1)$$

For the special case of localized electrons in orthogonal orbitals, such as transition materials or its alloys, Dirac showed that the effect of the Pauli principle was equivalent to an Heisenberg exchange Hamiltonian, modeled as an interaction of spins on different atomic sites, in Eq.1.2[13]. When J>0, neighbour spins prefer aligned states and have lower energy. Solving the Hamiltonian including the exchange interaction, the electronic states hybridize and form bands. In materials with tightly bound 4f or 3d orbitals, such as iron, cobalt and nickel, the localized 4f or 3d state forms narrow bands, so that the exchange splitting can stabilize a spin-polarized ferromagnetic state, by generating a self-consistent shift of the majority-electron-spin band to lower energy than the minority-electron-spin states. This compensates the kinetic energy of electrons occupying the band with the same spin state, shown in Fig 1.1(a). This long-range ordering of the atomic moments from the electrons characterizes the ferromagnetic materials, even in the absence of an external field, shown in Fig 1.1(b). In most materials, the exchange effect is weak and the hybridization band is wide, the electrons prefer to occupy the low kinetic energy states in both spin polarizations, known as paramagnetism, in Fig 1.1(b).

$$H_{ex} = -2 \sum_{i<j} J_{ij} S_i \cdot S_j \quad , \tag{1.2}$$

The spontaneous long-range magnetization of a ferromagnet is destroyed by
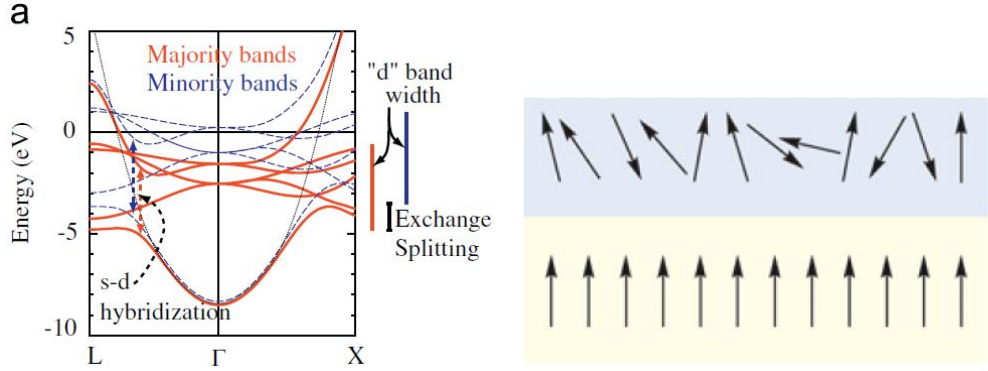
Figure 1.1: (a). Model band structures for ferromagnets. The solid red (dashed blue) curves give the majority (minority) bands along two high symmetry directions through the Brillouin zone center, Γ. The bands are calculated in the LSDA for face-centered cubic (fcc) Co. The dotted black curve shows what the energy of the sp band would be if it were not hybridized with the d bands. The bars to the right of (a) show the width of the d bands and the shift between the majority and minority bands. (b)Paramagnetic (upper) and ferromagnetic (lower) spin moments in lattice real space, assuming the lattice temperature is zero.

temperature, beyond the Curie temperature T_c. Above the Curie temperature, the number of magnon with $\boldsymbol{k} = 0$ wavevector, representing the spontaneous magnetization magnitude, is zero, as shown in Fig 1.2. The magnon distribution, behaving as bosons, can be obtained applying Bose-Einstein statistics of the spin wave accurately. Where ω_k eqauls to the intrinsic frequency of the spin wave, the state occupation number is

$$n_{\omega_k} = \frac{1}{e^{(\hbar\omega_k - \mu)/k_B T} - 1} \quad , \tag{1.3}$$

For high temperature, the statistics can be described by Boltzmann distribution
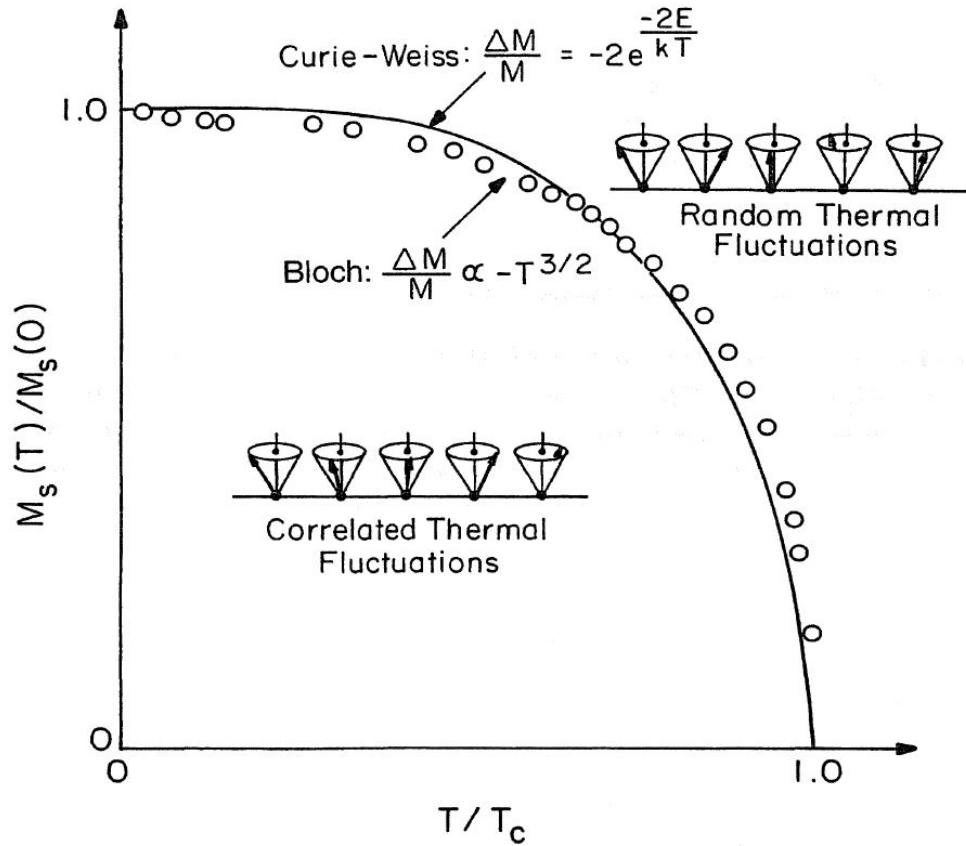
Figure 1.2: Reduced magnetization versus reduced temperature for nickel. the inset shows the spin wave configuration for non-zero lattice temperature.

$\propto e^{-\hbar\omega_k/k_B T}$.

1.2 Anisotropic Magnetic Materials

The preference for the spontaneous magnetization to lie in a particular direction in a material is called magnetic anisotropy. The magnetization responds differently to the external applied magnetic field H_{ext} when the field is in various directions,

known as the hysteresis loop in Fig. 1.3.
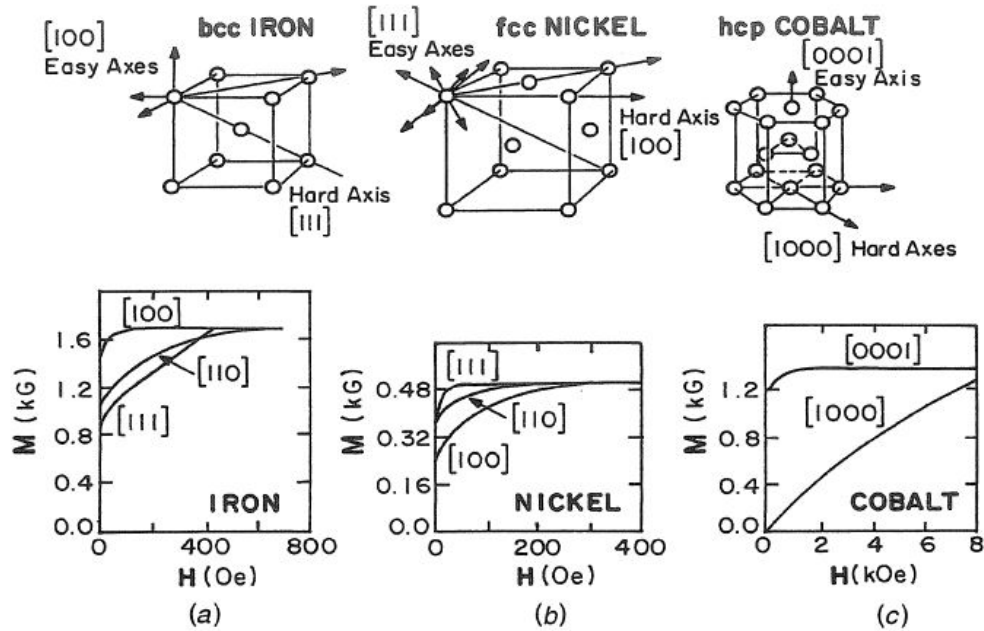
Figure 1.3: Crystal structures showing easy (energy minimum) and hard magnetization directions for Fe(a), Ni(b) and Co(c), above. Respective hysteresis loops, below, show the magnetization response to the applied field in various directions. Figures from Ref. [1]

Aside from the shape anisotropy produced by the magnetostatic effect from the un-neutralized magnetic charges existing on the surface or within the magnetic body, the magnetocrytalline anisotropy is not related to the material size and is determined only by the intrinsic material properties. Its origin lies in the coupling of the spin to the electronic orbital shape and orientation through SOI and the non-zero orbital moment ($L_z \neq 0$) interacting with the local crystalline

electric field. The crystalline field needs to be asymmetric so certain spin orienta-
tions are energetically preferred. Thus the magnetocrystalline anisotropy (MAE)
is roughly related to the asymmetry of the electronic states and the SOI strength
of the consistent atoms in the ferromagnetic materials. This is demonstrated by
the high perpendicular MAE in the CoFe/MgO attributed to the interfacial sym-
metry breaking and Fe(Co) 3d-O 2p orbitals hybridization[14, 15]. Also, materials
containing heavy metals shows large MAE, e.g. $L1_0$ FePt, superlattice Co/Pt ori-
ented along the [111] axis. In the transition metal atoms, magnetic anisotropy
is usually treated by examining the energy splitting of the valence states, as the
valence states are the main source producing spin and orbital moment, and adding
SOI as a perturbation. The common forms of MAE can be cubic, in Eq. 1.4 or
uniaxial, in Eq. 1.5. For the cubic MAE, the energy minimum lies in the axis
$< 100 >$. Known materials are bcc Fe, fcc FeNi alloys and bcc FeCo alloys. For
the uniaxial cases like Co, $Fe_{14}Nd_2B_1$ and $L1_0$ alloys, the energy surface has a
minimum on the c axis.

$$E = E_0 + K_1(\alpha_1^2\alpha_2^2 + \alpha_2^2\alpha_3^2 + \alpha_3^2\alpha_1^2) + K_2(\alpha_1^2\alpha_2^2\alpha_3^2) \quad , \tag{1.4}$$

where α_1, α_2, and α_3, are direction angles of the magnetization along the three
coordinate axes

$$E = E_0 + K_{\mu 1} \sin^2(\theta) + K_{\mu 2} \sin^4(\theta) \quad , \tag{1.5}$$

where θ is the angle between the magnetization vector and the c axis.

1.3 Spin Transport Effect

Electrical transport properties in magnetic materials are closely connected with the magnetic properties. The conduction electrons in metals typically consist of states with s or p type, while f states participates hardly in conduction as they are highly localized atomic state. However, d state is intermediate and can affect conduction to some extent. Hybridization of s and d states brings a degree of orbital angular momentum to the conduction process. Empty d states can be occupied temporarily by conduction electrons, providing a spin-dependent and orbital angular momentum dependent scattering process. In insulating materials, mostly oxides, the transport is often governed by thermally activated electrons from s-d or p-d bonds and is intimately connected with magnetism by the exchange effect. These magnetic dependent transports are both valuable probes of magnetism in materials and applied widely in many spintronic devices. We will introduce some important spin transport effect in this section, e.g. giant magnetoreistance, tunneling magnetoreistance.

1.3.1   Giant Magnetoresistance

A typical GMR device consists of at least two layers of ferromagnetic materials (FM) separated by a nonmagnetic metal (NM) as a spacer[2]. The GMR presents a lower resistance (R_P) when the orientations of the magnetizations in the two FM layers are parallel and higher resistance (R_{AP}) when antiparallel, where the magnetoresistance (MR) ratio is defined as $MR = (R_{AP} - R_P)/R_P$. The MR ratio can reach 100% or more in multilayers with a high number of F/M periods[16]. In the two-current conduction model proposed by Fert and Campbell, when the two magnetic layers are magnetized parallel, the spin-up electrons can travel through the sandwich nearly unscattered, providing a conductivity shortcut and a low resistance. On the contrary, in the antiparallel case, both spin-up and spin-down electrons undergo collisions in one FM layer or the other, giving rise to a high resistance, as shown in Fig. 1.4. In the limit where the spin diffusion length is much longer than the mean free path, the Boltzmann model reduces to a macroscopic transport model. The spin is accumulated at the interfaces and the spin-dependent electrochemical potential shows a diffusion type, scaling by the spin diffusion length. The electrical resistance related with magnetic state can be expressed by macroscopic transport coefficients, conductivty and spin diffusion length, in Eq. 1.6[17].
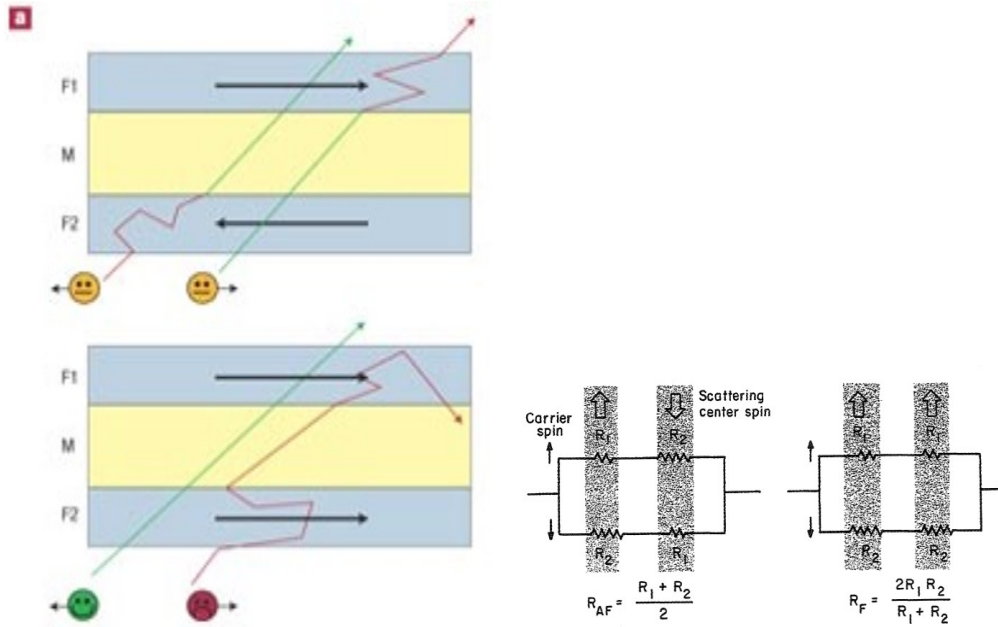
Figure 1.4: This drawing shows a GMR device with two ferromagnetic (FM) layers separated by a nonmagnetic (NM) layer. When the magnetizations in the two ferromagnetic layers are aligned, as shown in the diagram on the left, half the electrons experience relatively little scattering, leading to a substantial reduction in resistance. Figures from Ref. [1, 2]

$$R_P = R_{AP} - \frac{(\beta \rho_F^*[t_F M + 2\gamma r_b^* M)^2}{R_{AP}} \quad , \tag{1.6}$$

where β is a bulk spin asymmetry resistivity coefficient in the FM layer, ρ_F is the bulk FM layer resisitivity. Thus spin-dependent bulk resistivity $\rho_{\uparrow(\downarrow)} = 2\rho_F^*[1 - (+)\beta]$. γ is an interfacial spin asymmetry coefficient, r_b^* is the interfacial resistance. The spin-dependent interface resistance $r_{\uparrow(\downarrow)} = 2r_b^*[1 - (+)\gamma]$. M is the period number of FM/NM bilayer. t_F and t_N are the thickness of the FM and NM layer respectively. This simplified equation is in the limit where the layer thicknesses

are much smaller than the spin diffusion length.

1.3.2   Tunneling magnetoresistance

Inserting a thin non-magnetic insulating layer to replace the non-magnetic metallic spacer layer in the previous giant magnetoresistance effect, yields a big step forward in the magnetoresistance ratio. The electrons tunnel from one ferromagnetic layer to the other through the insulating layer, thus the spins are conserved, as shown in Fig. 1.5(a). A single-crystal MgO barrier is found to be an optimized option in obtaining much higher tunneling effect[18, 19]. With a MgO barrier, the tunneling current is carried by evanescent waves of several well-defined symmetries. Exprimental results show the tunneling magnetoresistance ratio (TMR) can be 1010% at 5K, and 500% at room temperature[3],shown in Fig. 1.5(b). This high TMR can be calculated through the real-space Kubo formula in terms of one-electron Green's functions at the Fermi surface[20]. The total conductance Γ^σ in a spin channel σ, as a reverse of the resistivity, is shown in Eq. 1.7. The decay of the electron wave is much slower and the transmission higher for the evanescent waves of specific symmetry. Thus the TMR is strongly related with the majority- and minority-spin surface spectral densities of the magnetic layer and the complex MgO Fermi surface.
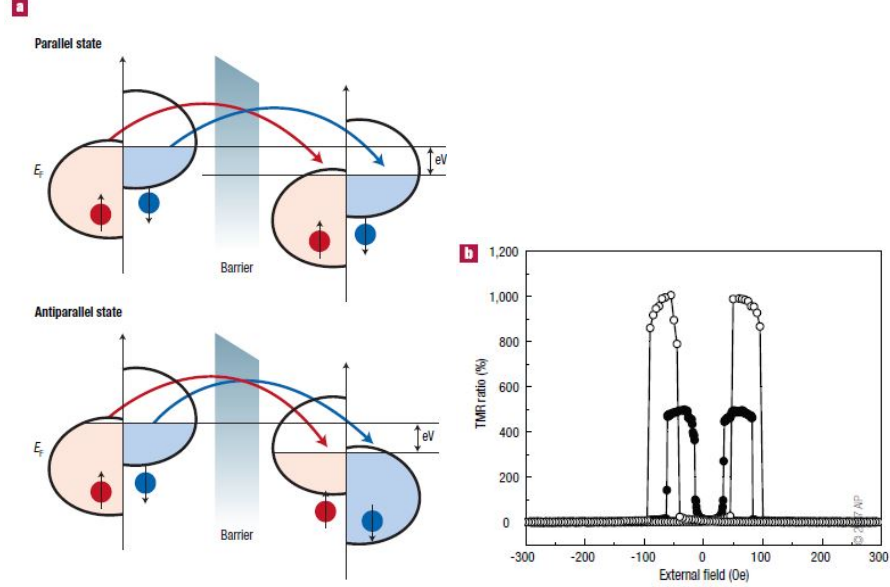
Figure 1.5: a, Schematic representation of the tunnel magnetoresistance in the case of two identical ferromagnetic metal layers separated by a non-magnetic amorphous insulating barrier. The tunnelling process conserves the spin. When electron states on each side of the barrier are spin-polarized, then electrons will more easily find free states to tunnel to when the magnetizations are parallel (top picture) than when they are antiparallel (bottom picture). b, High TMR$=(R_{max}-R_{min})/R_{min}$ for the magnetic stack $\{(Co_{25}Fe_{75})_{80}B_{20}$ (4 nm)/MgO (2.1 nm)/$(Co_{25}Fe_{75})_{80}B_{20}$ (4.3 nm)$\}$ annealed at 475 C after growth, measured at room temperature (filled circles) and at 5 K (open circles). (a) is from Ref. [2]. (b) is from Ref. [3].

$$\Gamma^{\sigma} = \frac{4e^2}{h} \sum_{\mathbf{k}_{\parallel}} Tr([\mathbf{T}_{\sigma}Im\mathbf{G}_0^{\sigma}(\mathbf{k}_{\parallel})].[\mathbf{T}_{\sigma}^{\dagger}Im\mathbf{G}_1^{\sigma}(\mathbf{k}_{\parallel})]) \ , \tag{1.7}$$

1.3.3 Spin Transfer Torque

In the previous magnetoresistance effects, the orientations of the magnetization

for ferromagnetic elements can determine the amount of current flow through the

interactions of spins and electrons. With the same interactions, the electronic current can also manipulate the spin orientations. This last effect, named as spin transfer torque, has been predicted by Slonczewski[21] and Berger[22] independently. For sufficiently large current flowing perpendicular to the plane in a metallic multilayer, it can generate a spin transfer torque strong enough to reorient the magnetization in one of the layers. Experimental proof of spin-transfer-torque driven magnetic switching is shown in a metallic multilayer and a magnetic tunnel junction[23, 24], in Fig. 1.6.
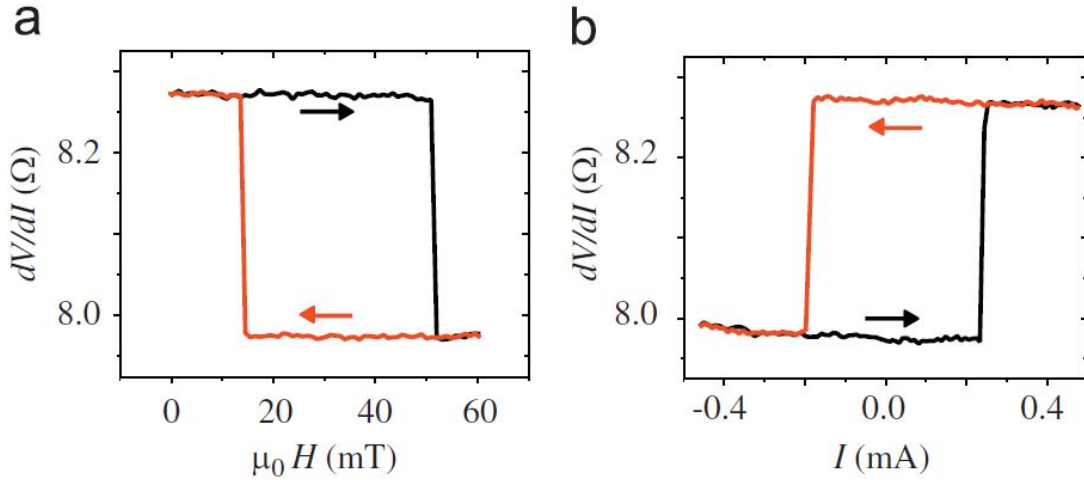
Figure 1.6: Comparison of magnetic switching at room temperature as driven by applied magnetic fields and by spin transfer torques. (a) Switching for an all-metal nanopillar sample consisting of the layers 20nm {$Ni_{81}Fe_{19}$/12nm Cu/4.5nm $Ni_{81}Fe_{19}$}, as the magnetization of the thinner (free) magnetic layer is aligned parallel and antiparallel to the thicker magnetic layer by an applied magnetic field. (b) Spin-torque-driven switching by an applied current in the same device, with a constant magnetic field applied to give zero total field acting on the free layer. Data for (a) and (b) are from Ref. [4].

The spin transfer torque arises whenever the flow of spin-angular momentum through a sample is not constant, but has sources or sinks. When a spin current (created by spin filtering from one magnetic thin film) is filtered again by another magnetic thin film whose moment is not collinear with the first, the second magnet necessarily absorbs a portion of the spin-angular momentum that is carried by the electron spins, thus changes its orientation. This spin transfer torque is related with the spin current density $\mathbf{Q}$, which is the outer product of the average electron velocity and spin density. For a simplified single electron model, $\mathbf{Q}=\mathbf{v}\otimes\mathbf{s}$. Applying a single-electron wave function ψ, the spin current density is

$$\mathbf{Q} = \frac{\hbar^2}{2m} Im(\psi^*\sigma \otimes \nabla\psi) \ , \qquad (1.8)$$

where m is the electron mass, σ is the Pauli spin vector. Based on the conservation of the angular momentum, the spin transfer torque can be computed through determining the net flux of non-equilibrium spin current through the surfaces of that volume, shown in Eq. 1.9.

$$\mathbf{N}_{st} = -\int_{surface} d^2R\hat{n} \cdot \mathbf{Q} \ , \qquad (1.9)$$

where the surface is the surface area of the ferromagnet, R is the in surface position and $\hat{n}$ is the interface normal vector of the ferromagnetic surface. Consider the magnetizations in the two adjacent ferromagnet layeys are noncollinear with an angle θ,shown in Fig 1.7 the incident Ψ_{in} , transmitted Ψ_{trans} and reflected Ψ_{refl}

wave functions are

$$\Psi_{in} = \frac{e^{\imath k x}}{\sqrt{\Omega}} \left(\cos(\theta/2)|\uparrow\rangle + \sin(\theta/2)|\downarrow\rangle\right) ; \tag{1.10}$$

$$\Psi_{trans} = \frac{e^{\imath k x}}{\sqrt{\Omega}} \left(t_{\uparrow}\cos(\theta/2)|\uparrow\rangle + t_{\downarrow}\sin(\theta/2)|\downarrow\rangle\right) ; \tag{1.11}$$

$$\Psi_{refl} = \frac{e^{\imath k x}}{\sqrt{\Omega}} \left(r_{\uparrow}\cos(\theta/2)|\uparrow\rangle + r_{\downarrow}\sin(\theta/2)|\downarrow\rangle\right) . \tag{1.12}$$

where $t_{\uparrow/\downarrow}$ and $r_{\uparrow/\downarrow}$ are the transmission and reflection amplitudes for spin-up (spin-down) electrons respectively, and Ω is the ferromagnet volume.

The spin transfer torque $\mathbf{N}_{st}$ on the ferromagnetic sink is equal to the net spin current transferred from the electrons, computed from the flows of spin density for the incident $\mathbf{Q}_{in}$, transmitted $\mathbf{Q}_{trans}$ and reflected $\mathbf{Q}_{refl}$ parts of the wave functions. In the simplified single electron model, the $\mathbf{N}_{st}$ is given as

$$\begin{aligned}
\mathbf{N}_{st} &= A\hat{\mathbf{x}} \cdot (\mathbf{Q}_{in} + \mathbf{Q}_{refl} - \mathbf{Q}_{trans}); \\
&= \frac{A}{\Omega}\frac{\hbar^2 k}{2m}\sin(\theta)\left[1 - Re(t_{\uparrow}t_{\downarrow}^* + r_{\uparrow}r_{\downarrow}^*)\right]\hat{\mathbf{x}}; \\
&\quad -\frac{A}{\Omega}\frac{\hbar^2 k}{2m}\sin(\theta)Im(t_{\uparrow}t_{\downarrow}^* + r_{\uparrow}r_{\downarrow}^*)\hat{\mathbf{y}}. \tag{1.13}
\end{aligned}$$

At a metallic interface, it is reasonable to neglect $Im(t_{\uparrow}t_{\downarrow}^*)$, $Im(r_{\uparrow}r_{\downarrow}^*)$, $Re(r_{\uparrow}r_{\downarrow}^*)$ and $Re(t_{\uparrow}t_{\downarrow}^*)$ due to dephasing when summing all contributions from around the Fermi surface. Thus on average for a one electron model, the spin transfer torque $\mathbf{N}_{st}$ is written as

$$\mathbf{N}_{st} = \frac{A}{\Omega}\frac{\hbar^2 k}{2m}\sin(\theta)\hat{\mathbf{x}}; \tag{1.14}$$
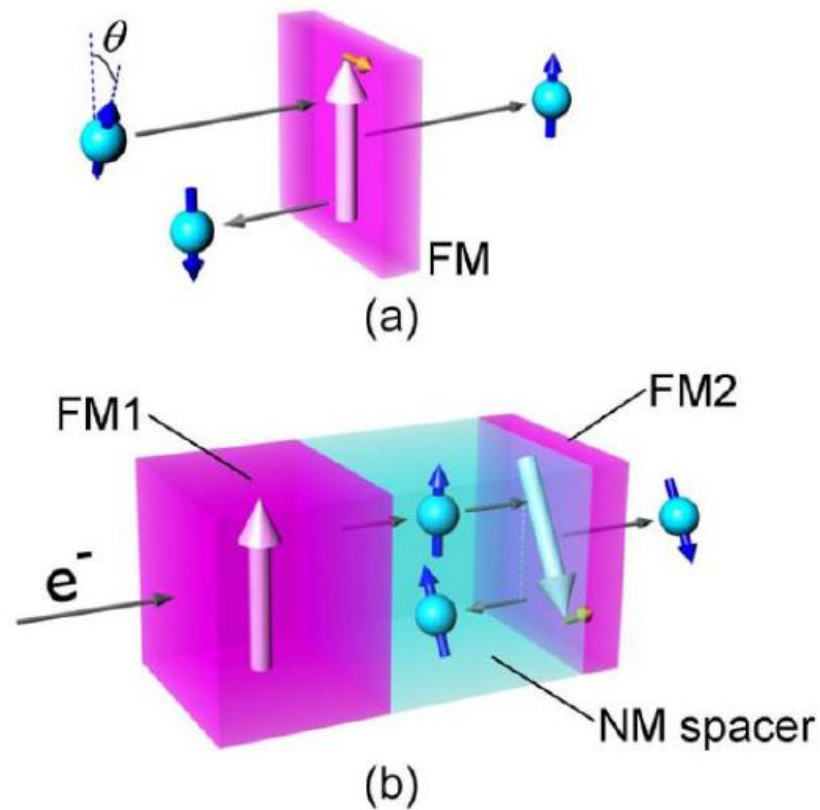
Figure 1.7: A spin-polarized current enters a ferromagnet. The interaction between the spin-polarized current and the magnetization causes a change in the spin direction of the outgoing electron compared with the incident electron. The difference in spin polarization causes torques on the ferromagnet. The figures are from Ref. [5].

The torque is dependent on the angle θ between two adjacent ferromagnets and inversely proportional to the volume of the ferromagnet. This result in Eq. 1.14 is accurate for metallic interfaces, like Fe/Ag or Cu/Co. But in magnetic semiconductors or at a ferromagnetic metal/insulator interface, like Fe/MgO, the phase of the wave function is consistent after scattering at the interface, and will introduce

an extra term into the spin transfer torque. In a more systematic and accurate approach, we can start with the equation of motion and consider the Hamitonian with interaction electrons under second quantization. The charge density $\hat{n}$ and spin density operators $\hat{\mathbf{s}}$ are

$$\hat{n} = (-e)\sum_{\sigma} \hat{\psi}_{\sigma}^{\dagger}(\mathbf{r})\hat{\psi}_{\sigma}(\mathbf{r}); \tag{1.15}$$

$$\hat{\mathbf{s}} = \frac{\hbar}{2}\sum_{\sigma,\sigma'} \hat{\psi}_{\sigma}^{\dagger}(\mathbf{r})\sigma_{\sigma,\sigma'}\hat{\psi}_{\sigma}(\mathbf{r}); \tag{1.16}$$

in terms of the creation $\hat{\psi}_{\sigma}^{\dagger}$ and destruction $\hat{\psi}_{\sigma}$ operators for an electron at point $\mathbf{r}$ and spin σ. With the equation of motion, we can derive the time evolving electron charge density and spin density. The spin transfer torque can be integrated into the Landau-Lifthitz-Gilbert equation to describe the spin dynamics. If spin-orbit coupling is included into the Hamiltonian, it will produce extra torque terms, such as spin-orbit torque. One last important point is the spin current can flow within devices even with no net charge current, thus spin transfer torque can be applied to magnetization elements which do not carry any charge current.

1.4 Spin Dynamics

When a magnetic configuration is applied a magnetic field, the configuration can be out of equilibrium, that its free energy is excited and will evolve in time to reach the energy minimization. Landau and Lifthitz proposed a dynamical model

derived from the equation of motion[25], in which the free energy is conserved. This term describes the magnetization precessing around the instantaneous local effective field. Gilbert introduced a phenomenological damping term, representing the energy dissipation. This term was said to be originated from the relativistic interaction between magnetic moment and the crystal in the original paper, [26]. Nowadays this term remains complicated and doesn't have an accurate explanation. We will discuss the multiple sources causing this term in the following section. When a spin current flows in the magnetic device in addition to the magnetic field, a spin transfer torque term is generally inserted into the Laundau-Lifthitz-Gilbert equation, as an additional contribution. This term can compensate the damping term and induce stable magnetization precession. In a recent study, the strong spin-orbit interaction in heavy metals can cause a similar effect as spin transfer torque, but different origin. These effects are named spin-orbit torque, that can be used to optimize the spin transfer torque applied in spintronic devices.

1.4.1   Landau-Lifshitz Equation

The motion of spin $\mathbf{S} = S_i \hat{e}_i$ can be derived by the equation of motion with dissipation energy neglected, in Eq. 1.17. The atomic magnetic moment $\mu_a = -$

$g\mu_b\mathbf{S}$, where g is the dimension less g-factor, μ_B is the Bohr magnet.

$$\frac{dS_i}{dt} = \frac{1}{\imath\hbar}[S_i, \mathscr{H}] = \frac{g\mu_B}{\imath\hbar}[S_i, S_j]H_j = \frac{g\mu_B}{\hbar}\epsilon_{ijk}S_kH_j; \tag{1.17}$$

where H_j is the magnetic field vector, the commutator of the spin is $[S_i, S_j] = \imath\epsilon_{ijk}S_k$. In a ferromagnetic material near $0K$, the average magnetization $\mathbf{M}$ can be written as: $\mathbf{M}$=-$ng\mu_B\mathbf{S}$, where n is the density. Thus the equation of motion of the magnetic moment is:

$$\frac{d\mathbf{M}}{dt} = -\gamma_0(\mathbf{M} \times \mathbf{H}); \tag{1.18}$$

where the constant γ_0 is the gyromagnetic ratio and usually takes the value as $1.76 \times 10^7 Oe^{-1}s^{-1}$. γ_0 can be deviated from this value in some materials if the orbital angular momentum is non-zero and contribute to the magnetization.

The effective magnetic field can be derived from the free energy $\mathscr{F}$, which includes the external magnetic field Zeeman energy $\mathscr{E}_{Zeeman}$, the anisotropy energy $\mathscr{E}_{ani}$ in the previous section, the exchange energy $\mathscr{E}_{ex}$ of Heiseberg model, the magnetostatic interaction energy $\mathscr{E}_{stat}$ and the magneto-elastic energy $\mathscr{E}_{strain}$:

$$\mathscr{F}(\mathbf{m}) = \mathscr{F}_0 + \mathscr{E}_{Zeeman} + \mathscr{E}_{ani} + \mathscr{E}_{ex} + \mathscr{E}_{stat} + \mathscr{E}_\sigma; \tag{1.19}$$

$$\mathscr{E}_{Zeeman} = -\int\int\int d^3\mathbf{r} M_s\hat{m}(\mathbf{r}) \cdot \mathbf{H}_{ext}(\mathbf{r}); \tag{1.20}$$

$$\mathscr{E}_{ani} = \int\int\int d^3\mathbf{r} \left(K^1_{ij}m_im_j + K^2_{ijkl}m_im_jm_km_l + o(m^6)\right); \tag{1.21}$$

$$\mathscr{E}_{ex} = \int\int\int d^3\mathbf{r}(A_{ij}(\partial_i m_l)(\partial_j m_l)); \tag{1.22}$$

$$\mathcal{E}_{stat} \quad = \quad 2\pi M_s^2 \sum_{\mathbf{r}} V_{\mathbf{r}} \sum_{\mathbf{r'}} \hat{\mathbf{m}}_{\mathbf{r}} \cdot \tilde{N}(\mathbf{r}, \mathbf{r'}) \cdot \hat{\mathbf{m}}_{\mathbf{r}}; \tag{1.23}$$

$$\mathcal{E}_{strain} \quad = \quad -\int \int \int d^3 \mathbf{r} \, a_{ijkl} t_{ij} m_k m_l; \tag{1.24}$$

where the magnetization vector $\mathbf{M} = M_s \hat{m}$, $\mathbf{H}_{ext}(\mathbf{r})$ is the space-dependent external magnetic field. K_{ij}^1 is the first order and K_{ijkl}^2 is the second order anisotropy parameter. A_{ij} is the exchange constant. $\tilde{N}(\boldsymbol{r}, \boldsymbol{r'})$ is the mangetostatic tensor. t_{ij} is the elastic strain tensor, and a_{ijkl} is the magnetostriction coefficient that links the magnetic property and the mechanical property in a solid. The effective field in the Landau-Lifshitz equation at a specific position $\boldsymbol{r}$ can be found by the variation $\mathbf{H}_{eff}(\boldsymbol{r}) = -\partial \mathcal{F} / \partial (M_s \hat{m}(\boldsymbol{r}))$.
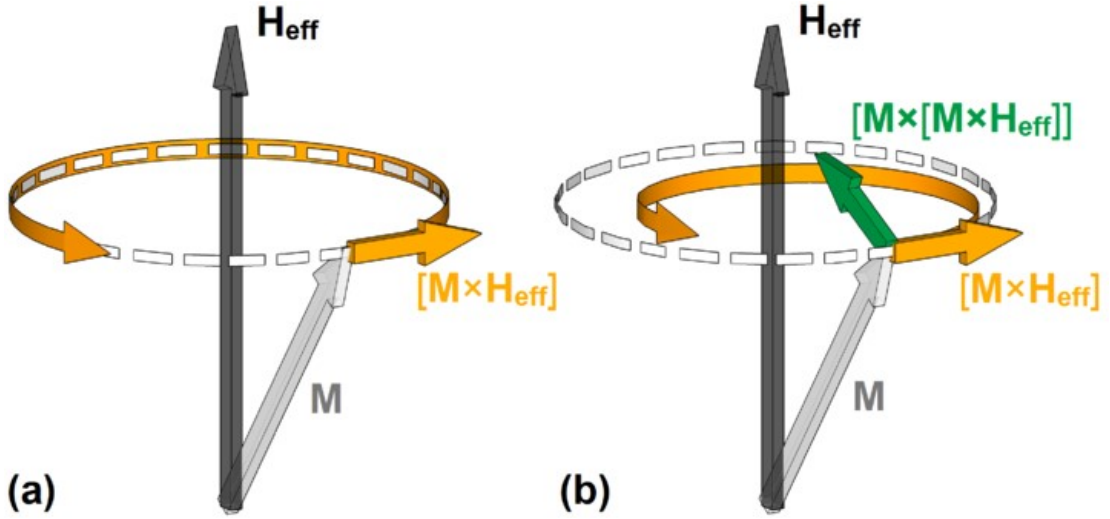
Figure 1.8: Illustration of the magnetization precession for (a) energy conserving and (b) energy dissipating motions.

1.4.2   Landau-Lifshitz-Gilbert Equation

Gilbert introduced a damping term by the dissipative Lagrange equation with a
Rayleigh dissipation function [26]:

$$\frac{d}{dt}\frac{\partial\mathscr{L}[\mathbf{M},\dot{M}]}{\partial\dot{M}} - \frac{\partial\mathscr{L}[\mathbf{M},\dot{M}]}{\partial\mathbf{M}} + (-\mathbf{H}_{eff} + \eta\dot{M}) \;=\; 0 \; ; \qquad (1.25)$$

$$\frac{\partial\mathbf{M}}{\partial t} \;=\; -\gamma_0\mathbf{M}\times\mathbf{H}_{eff} + \frac{\alpha}{M_s}\mathbf{M}\times\frac{\partial\mathbf{M}}{\partial t} \; . \qquad (1.26)$$

where α is the damping constant, representing the energy dissipation capability.
Using vector analysis, the Landau-Lifshitz-Gilbert can be rewritten as:

$$\frac{d\mathbf{M}}{dt} = -\frac{\gamma_0}{1+\alpha^2}(\mathbf{M}\ \times\ \mathbf{H}_{eff}) - \frac{\gamma_0}{1+\alpha^2}\frac{\alpha}{M_s}\mathbf{M}\ \times\ (\mathbf{M}\ \times\ \mathbf{H}_{eff}) \; . \qquad (1.27)$$

The first term on the right side causes magnetization to precess around the effec-
tive field. The second term is usually named as the damping torque, which aligns
the magnetization with the effective field, shown in Fig. 1.8(b). The LLG equation
has become the equation of choice for describing magnetization dynamics in part
because it can accurately model the results of a variety of measurements, but also
due to the familiar viscous form of the damping term and the convenience of the
dimensionless damping constant α.

With the energy dissipation term, the magnetization shows a damped motion
when its initial configuration is out of equilibrium. Fig 1.9 shows an example
trajectory of a magnetization vector subject to LLG dynamics. In Fig. 1.10(a)

we plot the projection of the magnetization onto the transverse x-axis versus time to show clearly that the magnetization follows the classic motion of a damped oscillator. Applying a Fourier transformation to the damped oscillation yields a Lorentzian shaped peak in the frequency space, as shown in Fig. 1.10(b). The center of the Lorentzian is the resonant frequency ($f_{res} = \gamma H_{eff}/(2\pi)$) of the magnetization while the Lorentzian width Δf is determined by the damping constant, $\Delta f = 2\gamma H_{eff}/(2\pi)$.

1.4.3 Landau-Lifshitz-Gilbert-Slonczewski Equation

For the case of a symmetric two-magnetic-layer device with a metal spacer, Slonczewski[27] calculated the spin transfer torque using a simplified Boltzmann equation. The spin transfer torque on the free-layer magnetization $\mathbf{M}$, produced by the spin current due to the misalignment with fixed layer magnetization $\mathbf{M}_{fixed}$ can be described by adding an additional term to the LLG equation, sometimes named as Landau-Lifshitz-Gilbert-Slonczewski (LLGS) equation:

$$\frac{\partial \mathbf{M}}{\partial t} = -\gamma_0 \mathbf{M} \times \mathbf{H}_{eff} + \frac{\alpha}{M_s} \mathbf{M} \times \frac{\partial \mathbf{M}}{\partial t} + \eta(\theta) \frac{\mu_B I}{e\mathscr{V}} \hat{\mathbf{M}} \times (\hat{\mathbf{M}} \times \hat{\mathbf{M}}_{fixed}) \ . \quad (1.28)$$

where I is the current, $\mathbf{V}$ is the free-layer volume on which the spin torque acts, $\eta(\theta) = q/(A + B\cos\theta)$, $\hat{\mathbf{M}}$ and $\hat{\mathbf{M}}_{fixed}$ are unit vectors in the directions of $\mathbf{M}$ and $\mathbf{M}_{fixed}$, and $\cos\theta = \hat{\mathbf{M}} \cdot \hat{\mathbf{M}}_{fixed}$. All of the details of the layer structure are
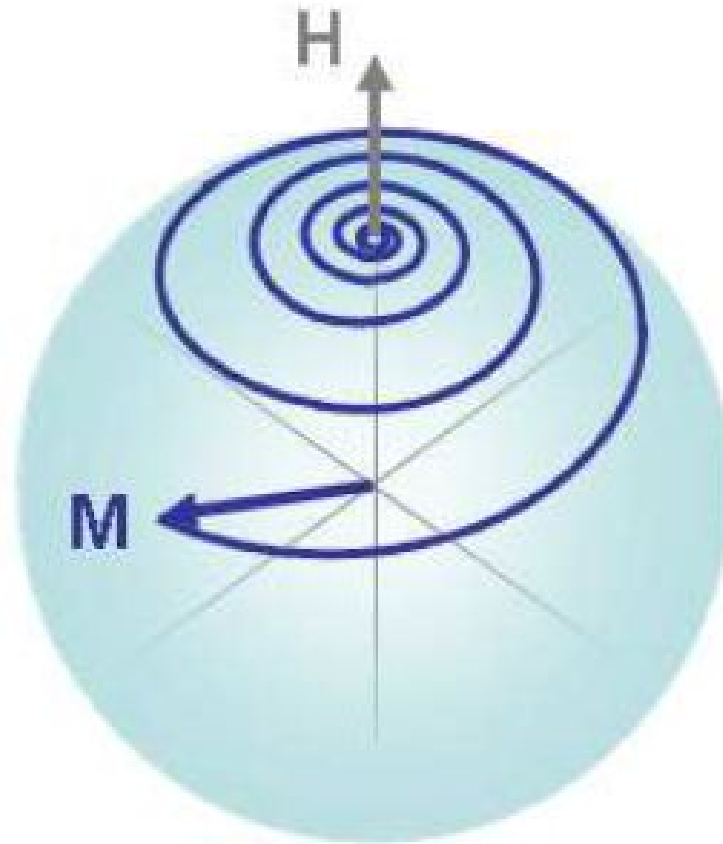
Figure 1.9: Magnetization trajectory dictated by the LLG equation. As the magnetization vector precesses around the effective field, it loses energy and aligns with the field direction finally.

in the constants q, A, and B. The direction of spin transfer torque indicated by

Eq. 1.28 is the same as that from the simple picture of Eq. 1.14, based on the

approximately complete absorption of the transverse spin current by the magnetic

free layer. When the current has the sign corresponding to electrons flowing from

the fixed layer to the free layer in a multilayer like Co/Cu/Co, the electron spin

moment incident on the free layer is in the same direction with $\mathbf{M}_{fixed}$. The
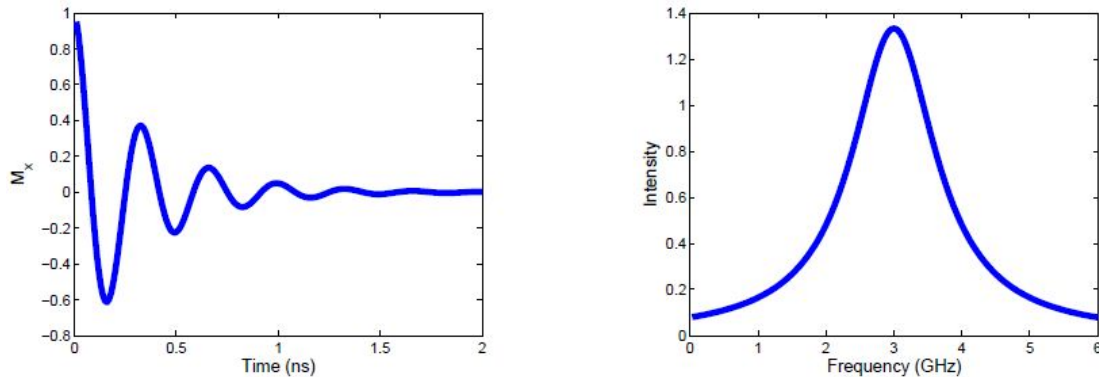
Figure 1.10: Magnetization dynamics in (a) the time domain and (b) the frequency domain. (a) shows the projection of a transverse component of the magnetization as a function of time. The transverse component behaves as a damped oscillation. (b) shows the signal in the frequency domain, through Fourier transformation of the time domain.

double cross product in Eq. 1.28 represents just the transverse component. The spin transfer torque has the same direction as the damping torque. In this case, no spin instability is induced by the flowing current. The magnetic state $\mathbf{M}$ simply spirals more rapidly back to the direction of $\mathbf{H}_{eff}$, due to the increase of the effective damping torque. When the current is reversed, it is the electrons reflected from the fixed layer that apply a torque to the free layer; their moments are on average oriented antiparallel to $\mathbf{M}_{fixed}$ on account of the reflection. Therefore the transverse component of spin current incident on the free layer has an opposite direction with the damping torque, shown in Fig 1.11. For small current, the spin transfer torque is weak and not comparable with the damping torque. $\mathbf{M}$ still aligns back to the direction of $\mathbf{H}_{eff}$, although with a slower speed, shown in

Fig 1.12(b). However, with sufficiently large current, the spin transfer torque can drive **M** away from equilibrium. **M** can achieve a state of dynamical equilibrium, precessing continuously at some fixed average angle, shown in Fig 1.12(c). In this state, the energy gained from the spin torque during the cycle of precession is balanced by the energy lost to damping. With a higher current so that the spin transfer torque overcomes the damping torque, it amplifies the deviations of **M** from equilibrium until **M** is reversed, in Fig 1.12(d).

In a magnetic tunnel junction, an additional contribution $N_{st\perp}$ to the spin transfer torque is perpendicular to the magnetization in the form

$$\vec{N}_{st\perp} = \eta_{\perp}(\theta)\frac{\mu_B I}{e\mathbf{V}}\hat{\mathbf{M}} \times \hat{\mathbf{M}}_{fixed}; \qquad (1.29)$$

due to the phase coherence of transverse spin density when averaging over the Fermi surface. Ab initio techniques find this perpendicular component of the spin transfer torque is small for the metallic multilayer devices, through computation of the transmission and reflection scattering wavefunctions. Thus we can write the LLGS equation in a magnetic tunnel junction by adding an additional perpendicular torque, shown below

$$\frac{\partial \mathbf{M}}{\partial t} = -\gamma_0\mathbf{M}\times\mathbf{H}_{eff}+\frac{\alpha}{M_s}\mathbf{M}\times\frac{\partial \mathbf{M}}{\partial t}+\eta_1(\theta)\frac{\mu_B I}{e\mathbf{V}}\hat{\mathbf{M}}\times(\hat{\mathbf{M}}\times\hat{\mathbf{M}}_{fixed})+\eta_2(\theta)\frac{\mu_B I}{e\mathbf{V}}\hat{\mathbf{M}}\times\hat{\mathbf{M}}_{fixed};$$

$$(1.30)$$
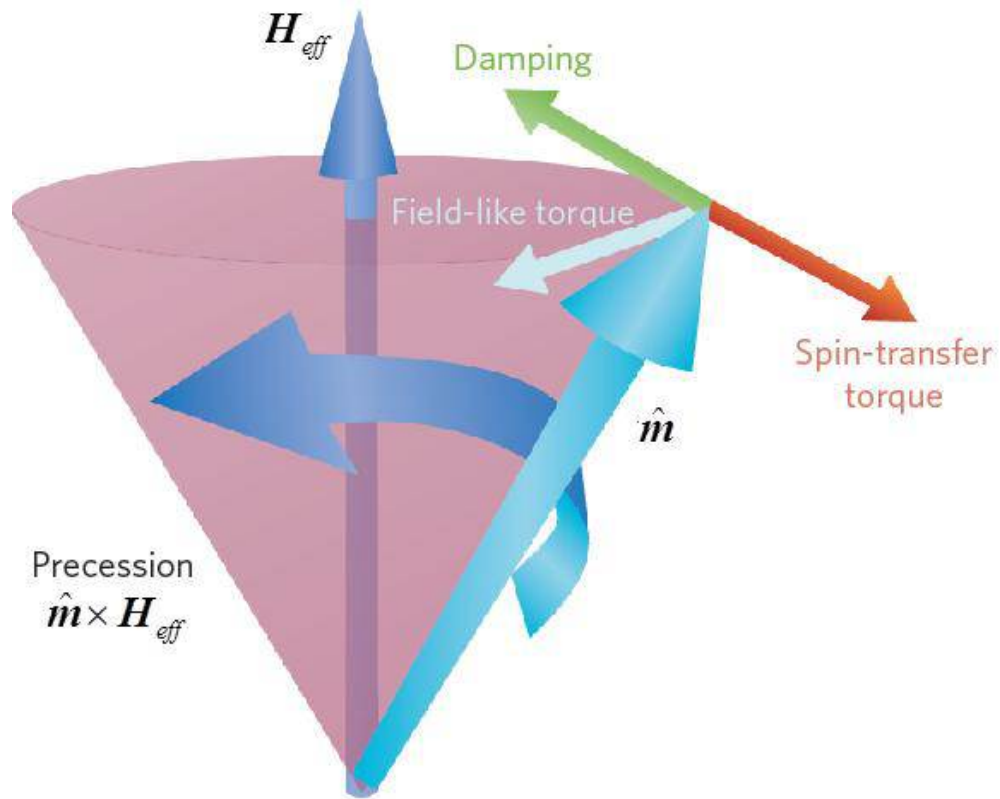
Figure 1.11: The magnetization $\hat{m}$ precesses about the effective field direction $\mathbf{H}_{eff}$. The red arrow illustrates the spin transfer torque, which direction is dependent on the sign of the flowing electric current. The light-blue arrow is the field-like torque, which is negligible in GMR structure but needs to be considered in the TMR structure. The figure is from Ref. [6]

1.5   Probing Magnetization Dynamics

Magnetization dynamics has been a difficult issue because the time scale of the

dynamics is nanosecond and the sample size is less than 100 nms. The unit-less

damping constant α is usually measured to represent the magnetization dynamics
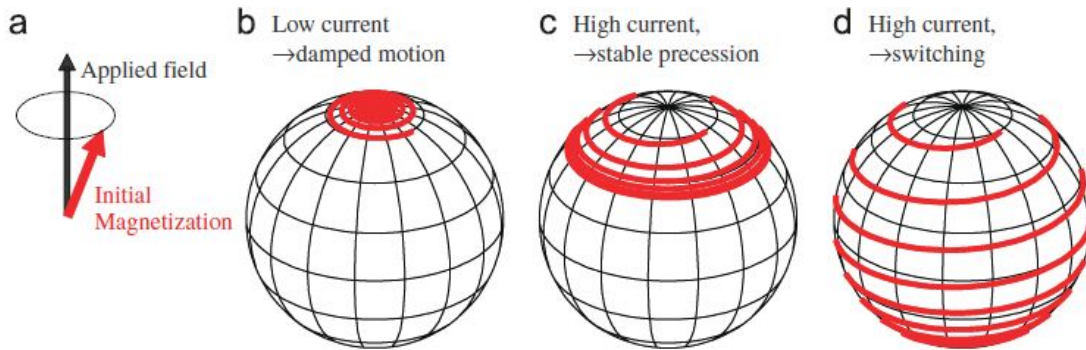
Figure 1.12: Trajectories of spin-torque-driven dynamics for the magnetization vector **M**. (a) Initial magnetic configuration assumed for panels (b,c,d), with the free-layer magnetization slightly misaligned from $\hat{z}$, for example due to a thermal fluctuation. (b) For currents below a critical current, **M** spirals back toward the low energy $\hat{z}$ direction on account of magnetic damping. For currents larger than the critical value, the spin-transfer torque causes the effective damping to become negative. The ultimate result can be either stable steady-state precession at large precession angle (c) or magnetic reversal (d).

as it determines the time of the system recovering the equilibrium state. Historically, α is measured in the frequency domain by the ferromagnetic resonance technique. This technique is limited at high frequency measurement range for decreased signal to noise ratio. With the development of ultrafast electronic circuits, pulse generators, and oscilloscope, newer techniques can probe the magnetization dynamics directly and the damping constant can be derived from the measurement in the time domain. These new techniques include pulsed inductive microwave magnetometry, magneto-optical Kerr effect and X-ray circular dichroism. In this section, I will outline some of these measurement techniques and the physics parameters they can measure.

1.5.1 Spin Torque Ferromagnetic Resonance

During a typical spin-torque ferromagnetic resonance (ST-FMR) experiment, a microwave current at GHz frequency is injected into a thin film samplein one side of the bias tee. A precessing $\vec{M}$ generates a dc voltage, measured by nanovolt-meter, shown in Fig 1.13(a). The precession mode of the sample has a natural frequency determined in part by the applied magnetic field. As the applied field strength is swept, the natural frequency of the sample resonates with the injected microwave current. The damping will cause a Lorentzian shape voltage centered at the resonance frequency.
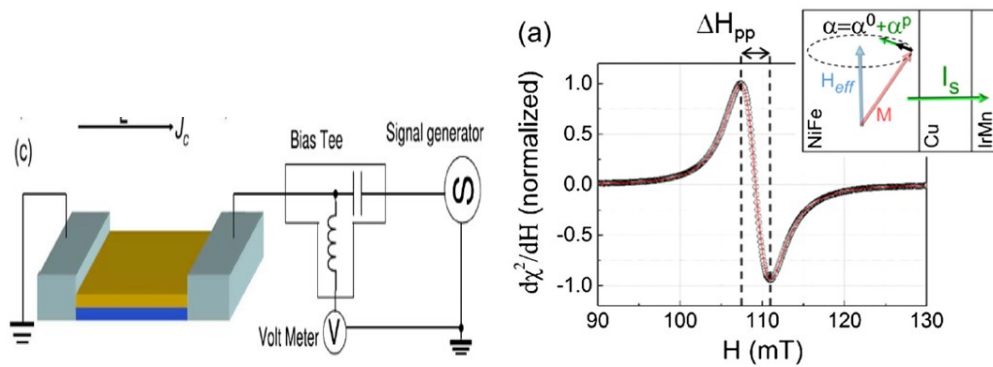
Figure 1.13: (a) the typical experimental setting of ferromagnetic resonance, using microwave probe method. This figure is from Ref. [7]. (b) the experimental data measured by ferromagnetic resonance. This figure is from Ref. [8].

1.5.2 Time Resolved Magneto-Optical Kerr Effect

The time resolved magneto-optical Kerr effect(TR-MOKE) has been a powerful method to study the time-domain measurement of the ultrafast magnetization dynamics of magnetic thin films, multilayers and pattered micro and nanostructures, due to its high accuracy, high temporal and spatial resolution and very fast response. It describes the change of the polarization states of light when reflected at a magnetic sample. In TRMOKE, magnetization dynamics is excited either by a pulsed magnetic field or by a femtosecond laser pulse. The dynamics is detected by a plane polarized femtosecond laser pulse, which probes the Kerr rotation as a function of the time-delay between the pump and probe beams.The general TRMOKE microscope set-up is shown in Fig. 1.14. In the setup, a Ti sapphire oscillator is used to generate a train of ultrashort laser pulses, whose duration of each pulse is around 100 fs. The laser beam is then divided into two beams, probe beam and pump beam. The pump beam will be modulated with a sinusoidal wave by an electro-optical modulator, then passed through a linear moving stage to achieve a variable time delay between pump and probe beams. The pump and probe beams are focused on the top surface of the sample by one objective lens. The reflected probe beam is divided into two orthogonal polarizations by a Wollaston prism, before being monitored by a balanced detector. A

magnet is used to magnetize the magnetic layer on the sample. Through a two color collinear and micro-focused pump-probe geometry, a spatial resolution of 700nm combined with a time resolution of 100fs can be achieved.
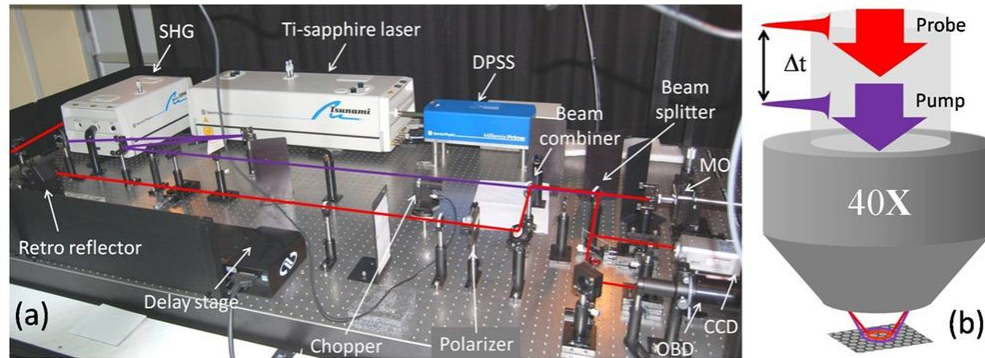
Figure 1.14: (a) A photograph of the all optical TRMOKE set up with collinear micro focused pump-probe geometry. (b) The collinear pump-probe geometry is shown schematically.

1.6 Physical Origins of Damping

The damping term, mentioned in the previous spin dynamic sections, represents the energy dissipation rate of the magnetic system. Magnetic damping occurs because the magnetic modes of a system (predominantly the electron spins) couple to the non-magnetic modes of the system (the electron orbits and lattice vibrations), allowing energy to be transfered back-and-forth. Since the magnetic modes are typically excited to a higher temperature than the other modes of the system, energy predominantly flows from the magnetic modes to the non-magnetic modes.

It has been a perennial problem for decades to understand the many coupling mechanisms and quantify their contributions to damping. Researchers have been working on this problem since Landau and Lifshitz published their phenomenological equation of motion in 1935. However, this damping problem still remains unexplained. Several experimental techniques can be used to measure the magnetization dynamics and damping constant, e.g. ferromagnetic resonance(FMR) and time-resolved magnetic-optic Kerr effect. Measured damping values vary in these different measurement techniques, and I will talk about the comparison between these techniques and the sources of the damping in this section.

The sources of damping can be divided into extrinsic effects, due to the sample imperfections and inhomogeneities, and intrinsic effects, due to the interactions between magnetic and non-magnetic modes existing in the system. Extrinsic effects are caused by the sample fabrication process and vary from sample to sample. The inhomogeneity of the sample is a typical extrinsic effect that results in a large damping value through various means, such as producing a distribution of local resonance field. Intrinsic damping effects are primarily from fundamental and natural interactions between the magnons and the electron orbits. These interactions include eddy currents and spin-orbit coupling. Summary of the intrinsic and extrinsic damping sources is shown in Fig. 1.15.

In this section, I will focus on the intrinsic effect that is caused by spin-orbit
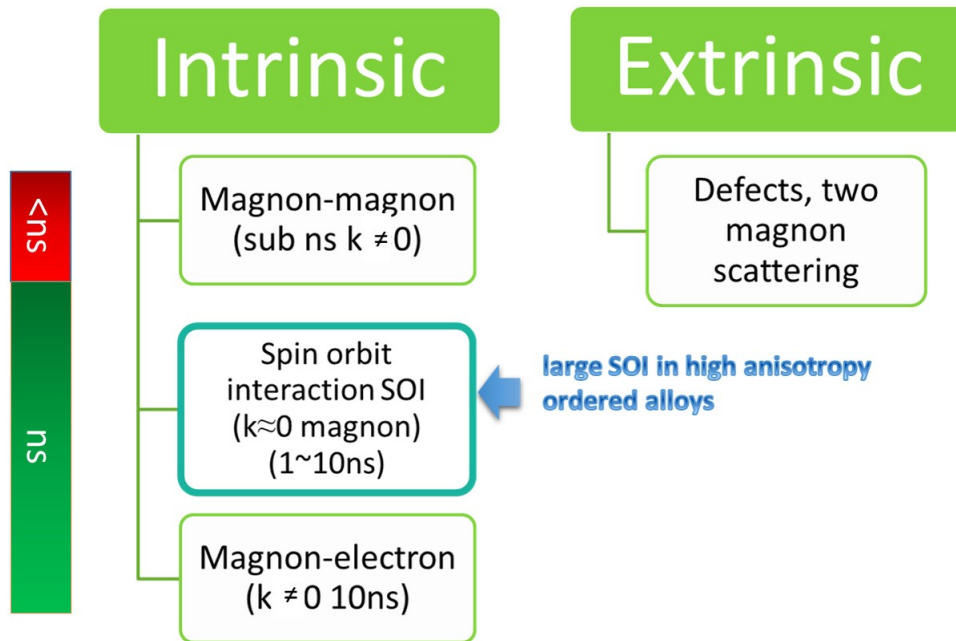
Figure 1.15: Summary of different damping sources for both extrinsic and intrinsic effects. The left time bar is the time scale of the damping mechanism, representing roughly at which time the mechanism is dominant.

interaction. I will also introduce how to experimentally separate the intrinsic effects from the extrinsic ones.

1.6.1 Extrinsic Effects

Extrinsic damping arises from sample inhomogeneities. These inhomogeneities include differences in the magnetocrystalline anisotropy, variations in surface anisotropies associated with step edges, local defects, deviations in sample thickness, magnetostriction paired with variable strains due to substrate imperfections

and other possibilities. It is complicated to have an exact treatment of the sample inhomogeneities, but it gives some physics insight into the system when we consider the limiting cases of strong inhomogeneities and weak inhomogeneities. In the strong inhomogeneity limit, different areas of the sample interact weakly and the sample behaves as though having a distribution of local resonance fields. On the other hand, the magnetization of the sample maintains long range order and precesses nearly uniformly. Inhomogeneities introduce the non-uniform modes coupling with the uniform mode. This is referred to as two-magnon scattering, because the uniform mode magnon decays into non-uniform magnons[9].

Local Resonance

The limiting case of the local resonance model is an ensemble of non-interacting magnetic grains that are measured simultaneously. Although the applied magnetic field can be uniform in the whole area of the sample, each grain still feels different effective field due to the variation in the orientation of the magnetocrystalline axes, magnetocrystalline anisotropies and other effects, and thus has an unique resoance field. Therefore, even if every resonance was perfect, a delta function response with respect to the applied frequency, these local resonances will still be dispersed around the mean resonance field. This produces an effective broadening of the measured resonance. At a simple level, when the magnetization is mostly

aligned with the applied field, the effect of the local resonance on the measured linewidth is

$$\Delta H \;=\; \Delta H_0 + \frac{2\alpha\omega_0}{\sqrt{3}|\gamma|} \; . \tag{1.31}$$

The inhomogeneties cause a nonzero intercept of the linewidth when extracting the linewidth versus the resonant frequency. This non-zero intercept is not caused by the damping with the uniform precession, but is a measure of the spread of the local resonance fields arising from the inhomogeneties. This linear behavior of the linewidth, with non-zero intercept, is often observed[28].

Surface Roughness Scattering

It is well known that inhomogeneities in ferromagnets induce 2-magnon scattering, which contributes to ferromagnetic relaxation[29, 9]. The long-range fluctuations of the film thickness result in nonuniform dipole-dipole fields, which couple the uniform mode with the non-uniform magnons, thus introducing the 2-magnon scattering. The scattering in the linear response region of the system is studied and corresponds to the time-resolved magnetodynamics experiment. Initially ($t < 0$), the external magnetic field $\mathbf{H}_0$ is applied in plane to orient the initial equilibrium magnetization at an angle ϕ_0 with the x axis. At $t = 0$, the direction of the field is suddenly switched to align with the x axis. In experiment, the evolution of the average magnetization of the film, as the $k = 0$ magnon, is observed.

The non-uniform magnetostatic field scatters the uniform $k = 0$ magnons into the nonuniform $k \neq 0$, thus inducing experimentally measured ferromagnetic damping.

Applying the Holstein-Primakoff transformation, the Hamiltonian can be rewritten as:

$$\mathscr{H} = \hbar \sum_{\boldsymbol{k}} \omega_{\boldsymbol{k}} b_{\boldsymbol{k}}^{\dagger} b_{\boldsymbol{k}} + S_{\boldsymbol{k}} b_0 b_{\boldsymbol{k}}^{\dagger} + S_{\boldsymbol{k}}^{\dagger} b_0^{\dagger} b_{\boldsymbol{k}}; \tag{1.32}$$

The surface roughness perturbation introduces terms of the type $b_{\boldsymbol{k}'}^{\dagger} b_{\boldsymbol{k}}$ into the Hamiltonian. These terms correspond to a 2-magnon process, in which one magnon is annihilated and another is created via interaction with surface defects. Only the scattering happens between the uniform k=0 magnon and the nonuniform k≠0 magnon is kept. The secondary process that nonuniform magnons scatter into other nonuniform magnon is neglected.

This time evolution of the uniform mode shows that the decay owing to the surface roughness is not exponential. This is confirmed by simulation results of a FeCo film with a Gaussian roughness correlation function, in Fig.1.16. The decay of the uniform mode follows the $exp\{-|t/\tau_{3/2}|^{3/2}\}$ law, while the angle decreases by an order of magnitude. The decay time $\tau_{3/2}$ has a dependence on the extrinsic parameters(applied field H_0, film thickness D_z, roughness standard deviation σ and correlation length R), which is also proved by the micromagnetic simulation, shown in Fig. 1.17.
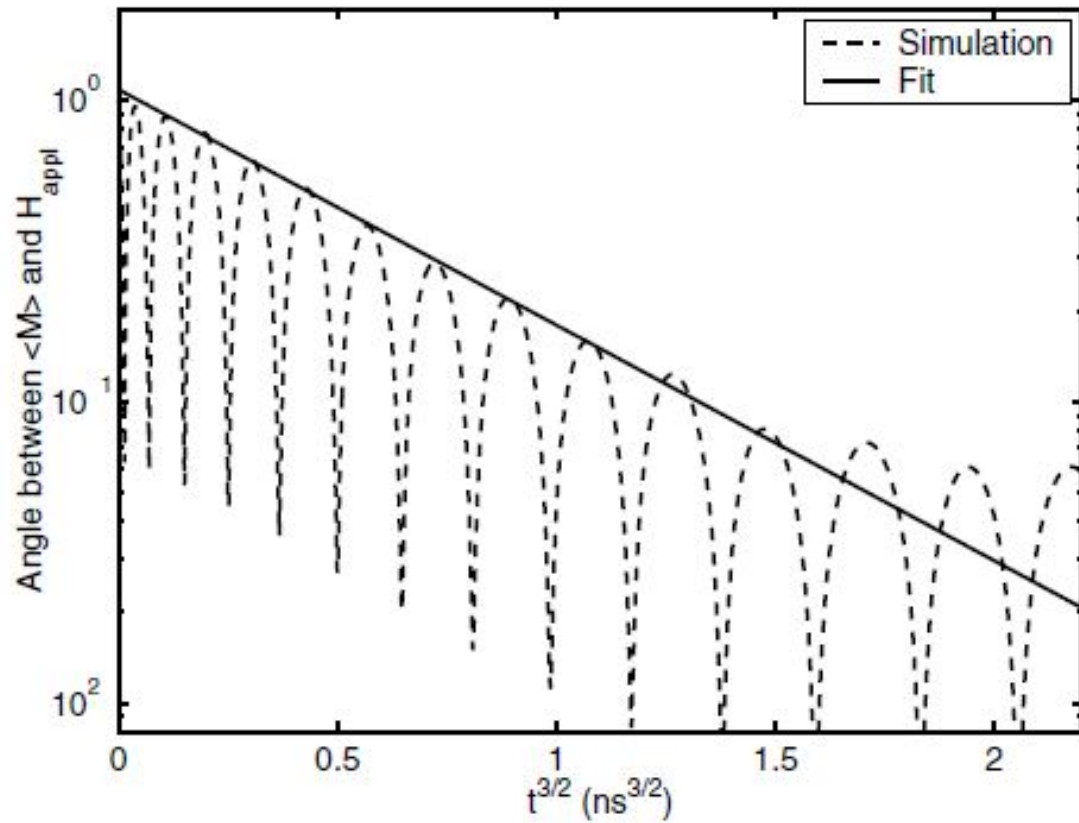
Figure 1.16: Time evolution of the angle between the average magnetization of the FeCo film and the applied field direction. The figure is from Ref. [9].

1.6.2 Intrinsic Effects

Intrinsic effects can induce damping, even for crystallographically perfect samples. The spin system has multiple ways to interact with the other degrees of freedom and thus this coupling can transfer energy from the spin system to the other systems, such as electrons and phonons. The magnons of uniform and nonuniform modes interact very strongly through the exchange interaction, which prefers

aligned spins, and the dipole interaction, which prefers the misaligned spins. The scattering between these magnons transfers energy from the uniform mode to the non-uniform mode , but the total energy of the spin system is conserved. The magnon propagating in the magnetic film causes a temporal and spatial electric field, which induces a motion of electrons. Thus the energy of the spin system is lost to the electrons due to this magnon-induced electric current. The spin is also coupled to the lattice through spin-orbit interaction, thus the spin energy can also transfer to the phonon. I will talk about these three mechanisms in detail below.

Four Magnon Scattering

The intrinsic four magnon scattering, which transfers energy from initially excited uniform precession mode to k $\neq$ 0 magnons, is a very important mechanism in large angle magnetization dynamics, in contrast to the linear FMR case. The damping rate for large angle rotation can be strongly enhanced with respect to the linear FMR values.

The number of magnons with wave vector $\boldsymbol{k}$ is given by $N_{\boldsymbol{k}} = b_{\boldsymbol{k}}^{\dagger} b_{\boldsymbol{k}}$. Following Suhls approach, only the 4th order terms which couple k = 0 with k $\neq$ 0 magnons is kept:

$$\mathscr{H} = \hbar \sum_{\boldsymbol{k}} \omega_{\boldsymbol{k}} b_{\boldsymbol{k}}^{\dagger} b_{\boldsymbol{k}} + \Psi_{\boldsymbol{k}} b_0 b_0 b_{\boldsymbol{k}}^{\dagger} b_{-\boldsymbol{k}}^{\dagger} + \Psi_{\boldsymbol{k}}^{\dagger} b_0^{\dagger} b_0^{\dagger} b_{\boldsymbol{k}} b_{-\boldsymbol{k}} . \qquad (1.33)$$

The $\Psi_{\boldsymbol{k}}$ terms correspond to the four-magnon scattering process (two k = 0

magnons annihilate, k and -k magnons are created). This term is strongly related with the exchange and magnetostatic interaction. The equation of motion $i\hbar\dot{b}_{\boldsymbol{k}} = \partial\mathcal{H}/\partial b_{\boldsymbol{k}}^{\dagger}$ can be solved the time evolution of the magnon number $N_{\boldsymbol{k}}(t)$:

$$for \ k \ \neq \ 0: \qquad N_{\boldsymbol{k}}(t) \ = \ \bar{N}_{\boldsymbol{k}}exp[\Gamma_{\boldsymbol{k}}t]; \qquad\qquad (1.34)$$

$$\Gamma_{\boldsymbol{k}} \ = \ \sqrt{16\bar{N}_0^2|\Psi_{\boldsymbol{k}}|^2 - (2\omega_0' - 2\omega_k')^2}.$$

$$for \ k \ = \ 0: \qquad N_0(t) \ = \ \bar{N}_0exp[-\Gamma_0 t]; \qquad\qquad (1.35)$$

$$\Gamma_0 \ = \ \Gamma_{\tilde{\boldsymbol{k}}}/ln\frac{\bar{N}_0}{V\bar{N}_{\tilde{\boldsymbol{k}}}C_{\tilde{\boldsymbol{k}}}\Gamma_{\tilde{\boldsymbol{k}}}}.$$

Here, $\tilde{\boldsymbol{k}}$ is the wave vector which delivers the maximum $\Gamma_{\boldsymbol{k}}$. The initial magnon number $N_{\boldsymbol{k}}(0)$ can be determined from boson distribution: $\bar{N}_{\boldsymbol{k}} = N_{\boldsymbol{k}}(t = 0) = 1/[exp(\hbar\omega_{\boldsymbol{k}}/T) - 1]$ for k $\neq$ 0 magnons, or the initial deviation of magnetization from equilibrium: $\bar{N}_{\boldsymbol{k}=0} = V/(2\hbar\gamma Ms)[M_y(t = 0)/(u_0 - v_0)]^2$. The dependence of decay time on initial k = 0 magnon occupation numbers (and thus on temperature) is very weak:$1/\Gamma_0 \ \sim \ ln[\hbar\omega_{\tilde{\boldsymbol{k}}}/T]$. The numbers of some k $\neq$ 0 magnons grow very rapidly with time, shown in Fig. 1.18. $1/\Gamma_{\boldsymbol{k}}$ represents the $\boldsymbol{k}$ depedent time scale for the the magnon increment and is sub-ns, shown in Fig. 1.19. The total magnon number is conserved, consistent with the four magnon scattering.
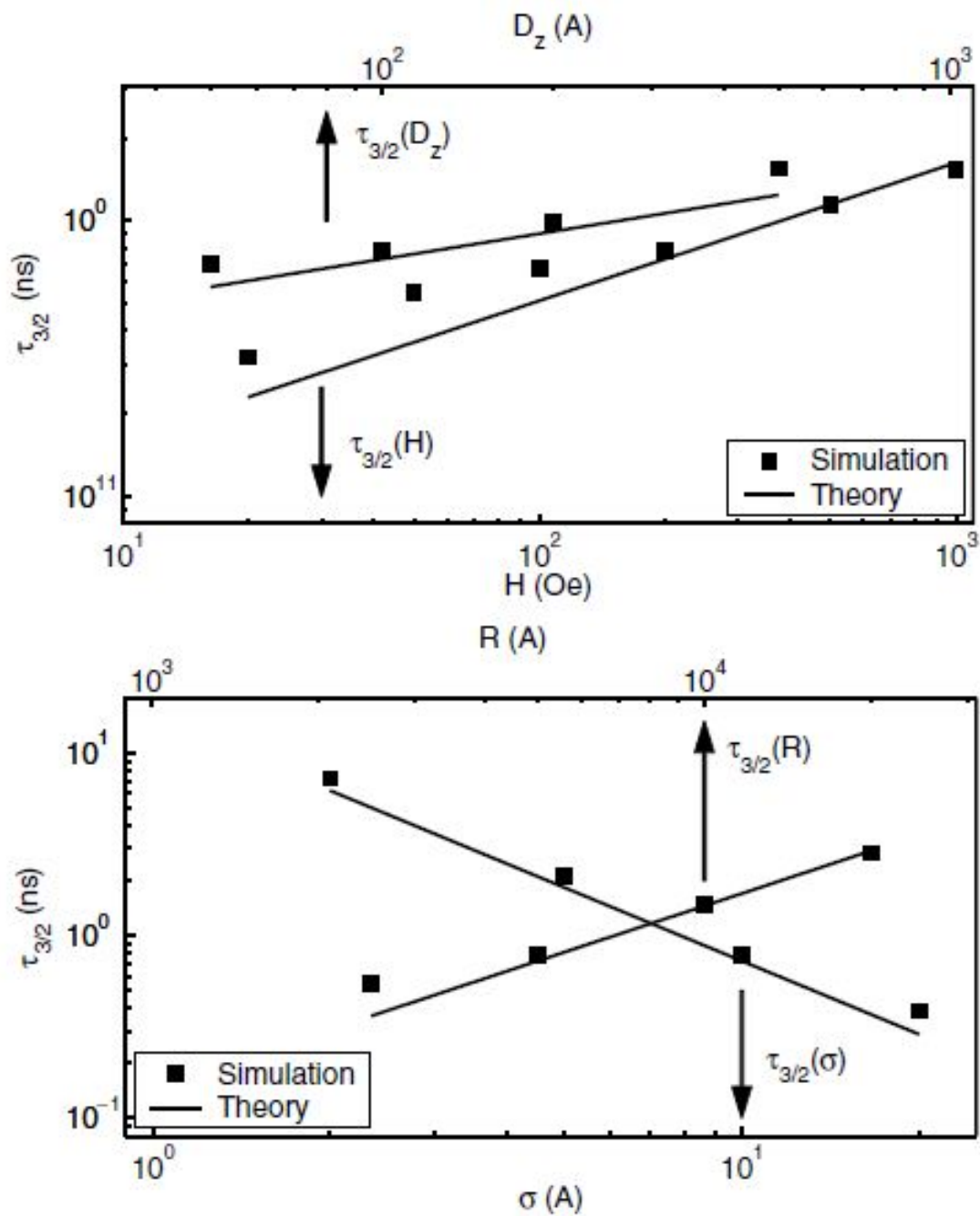
Figure 1.17: The dependence of the decay time $\tau_{3/2}$ on the applied field applied field H_0, film thickness D_z, roughness standard deviation σ and correlation length R. The figure is from Ref. [9].
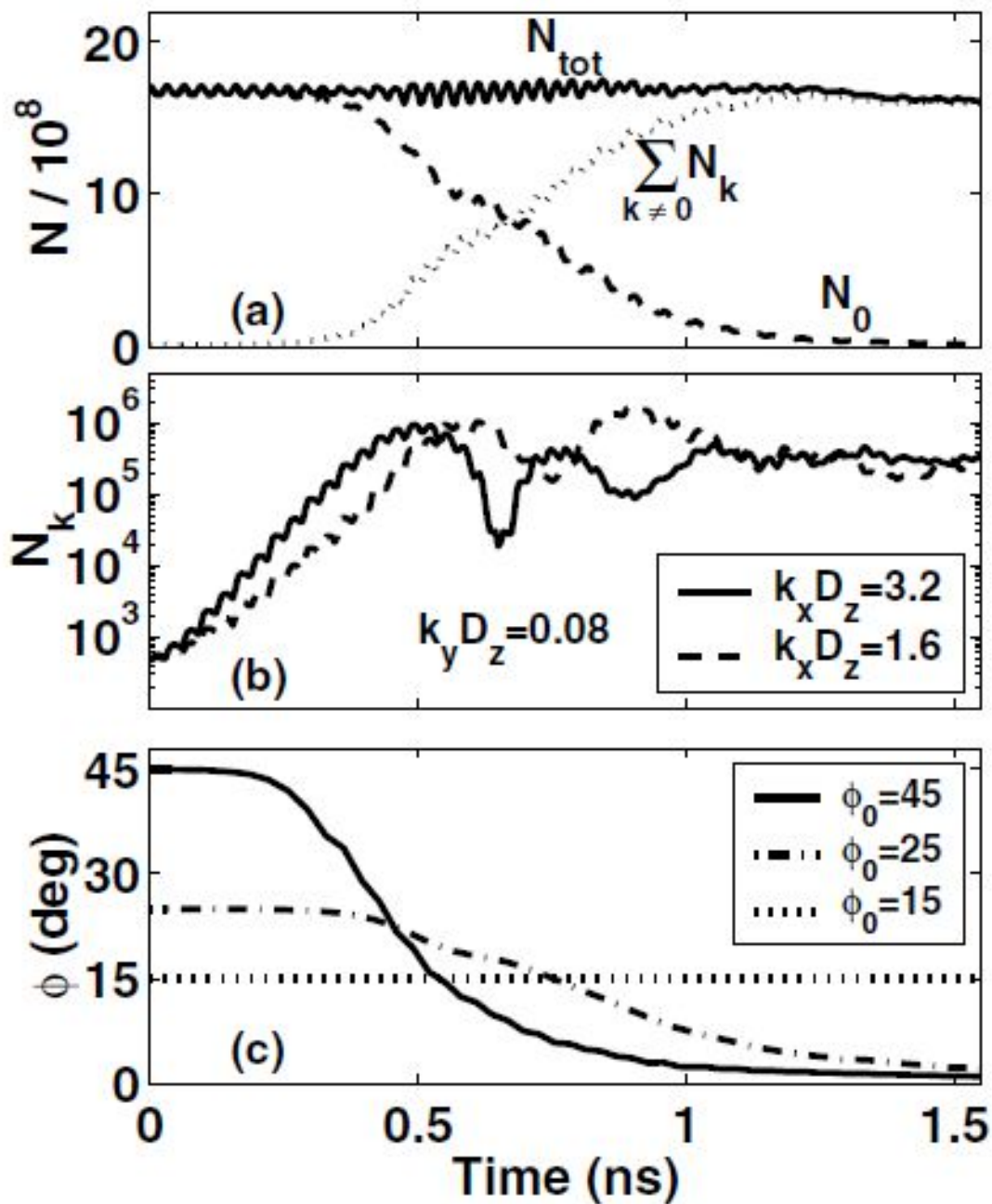
Figure 1.18: Time evolution of (a) number of k = 0 magnons N_0, number of k $\neq 0$ magnons $\sum_{k\neq 0} N_k$ and total number of magnons $N_{tot} = \sum_k N_k$; (b) magnon numbers N_k with different $\boldsymbol{k} \neq 0$ (c) envelope of the angle ϕ between the average magnetization and the applied field. The figure is from Ref. [10].
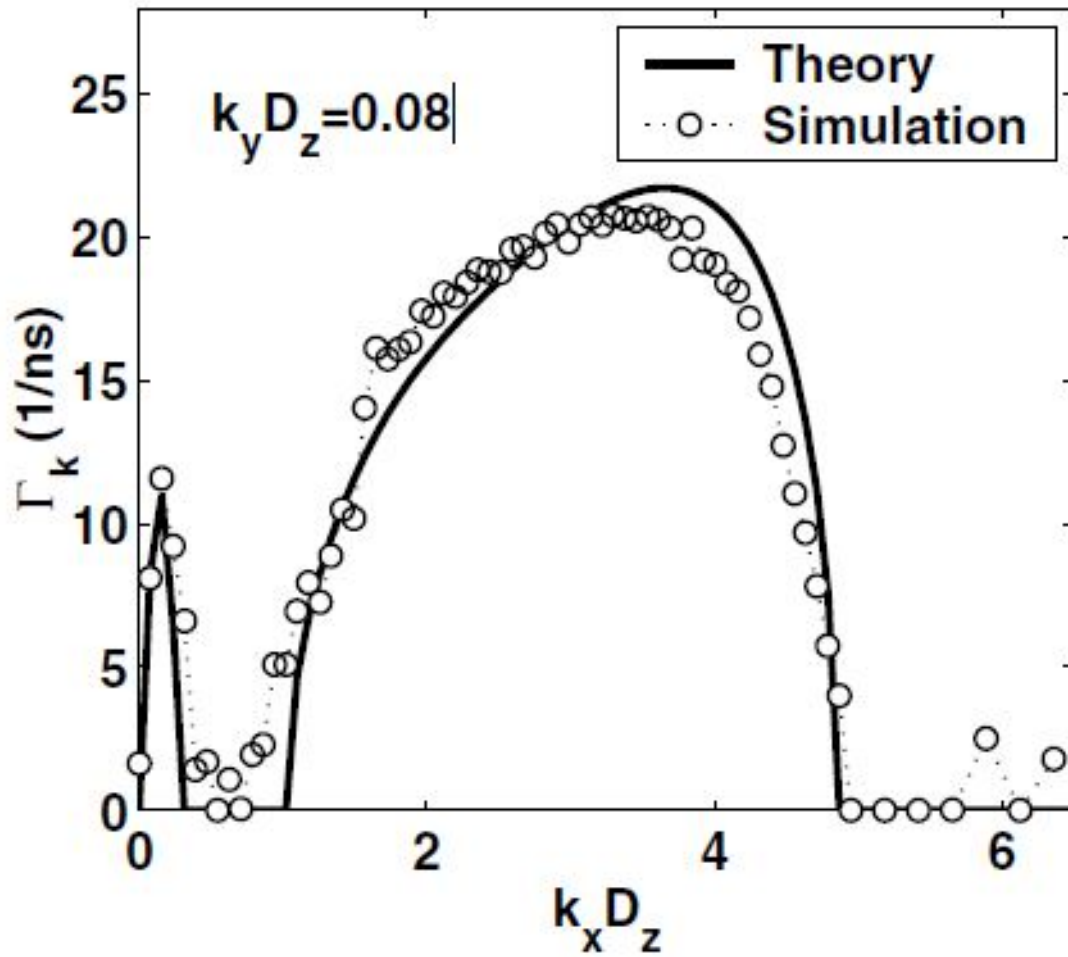
Figure 1.19: The simulation magnon increment rate $\Gamma_{\boldsymbol{k}}^{sim} = ln[N_{\boldsymbol{k}}(t_2)/N_{\boldsymbol{k}}(t_1)]/t$, $t_2 = 0.2ns, t_1 = 0.1ns$, and theoretical $\Gamma_{\boldsymbol{k}}^{th}$. The figure is from Ref. [10].

Chapter 2

Angular-Dependent Giant
Magnetoresistance

There has been great interest in current perpendicular to plane giant magne-toresistance (CPP GMR) in devices composed of ferromagnetic materials and normal metals[30], metioned in chapter I. CPP GMR may be useful for magnetic recording, owing to its large ratio of magnetoresistance and small volume compared to current-in-plane (CIP) GMR. Compared to TMR, it has much smaller resistivity[30] of 10^{-8} Ωm. Therefore, resistances of 10 to 100 Ω are easily achieved for small device diameters. CPP may produce more advantageous [31] signal-to-noise ratios (SNR) for recording densities over 500Gb/in^2 and head sizes below 40nm. It has been shown that GMR can be observed in nanowire structures[32] of

diameter 10nm. Much theoretical work has been done to calculate the maximum CPP MR ratio for particular materials. But little work has been done to calculate non-collinear magnetoresistance. A widely accepted model is the Valet-Fert model[17] that uses transport theory and assumes a continuous chemical potential. However, extension of this model cannot explain the non-linearity of MR dependence[33] on $\beta = \cos^2(\theta/2)$, where θ is the angle between the magnetizations in two adjacent layers.

Slonczewski[27] writes currents J and chemical potential W separately in basis parallel to the local non-collinear magnetizations. However, the symmetry of J and W breaks conservation of spin moment within the current when transporting through an interface of two ferromagnetic layers. Urazhdin et al.[34] writes 22 diagonal matrices of currents $\hat{\mathbf{I}}$ and resistances $\hat{\mathbf{R}}$ in two bases similar to Slonczewski's. They use a 2D rotation operator to transform currents and resistances of the free layer to the fixed layer basis. However, during the transformation, off-diagonal elements of matrix $\hat{\mathbf{I}}\hat{\mathbf{R}}$ are neglected, which also represents non-conservation of spin moment.

We take a different approach to the angular dependence of the magnetoresistance. In particular, we assume spin angular momentum is conserved and include multiple reflections between magnetization layers. We show that this produces the same general form of magnetoresistive angular dependence as Slonczewski or

Urazhdin et al., although very different than Valet-Fert[17]. However, the parameters in our theory depend solely on spin polarization and produce predictions that match experiment closely. We extend the model to a multilayer nanowire 10μm in length and get a similar MR versus applied field dependence as experiment[11].

2.1 Formulation

The difference between anti-parallel and parallel resistance is caused by spin-dependent scattering in the bulk and at the interface. In the model, we use a spin-dependent potential to represent scattering in ferromagnetic layers. Bulk scattering in the normal metal between the two magnetic layers is neglected here. Scattering matrices are calculated from a nearly free electron Hamiltonian. The relation between $\mathbf{S}$ matrices of different magnetic layers should be incoherent, because the calculations are for room temperature. We propose a one-dimensional model, so the conduction electrons are mono-energy and all are at the Fermi energy[27].

$$\mathbf{H} = -\frac{\hbar^2}{2m}\frac{d^2}{dx^2} + \mathbf{U}(x) + h\hat{m}\cdot\vec{\sigma}. \tag{2.1}$$

$\vec{\sigma}$ is the Pauli matrices vector. h (> 0) is half of the exchange splitting between majority and minority electrons. $\hat{m}(\text{x})$ is the unit vector of magnetization of each layer, as shown in Fig. 2.1.
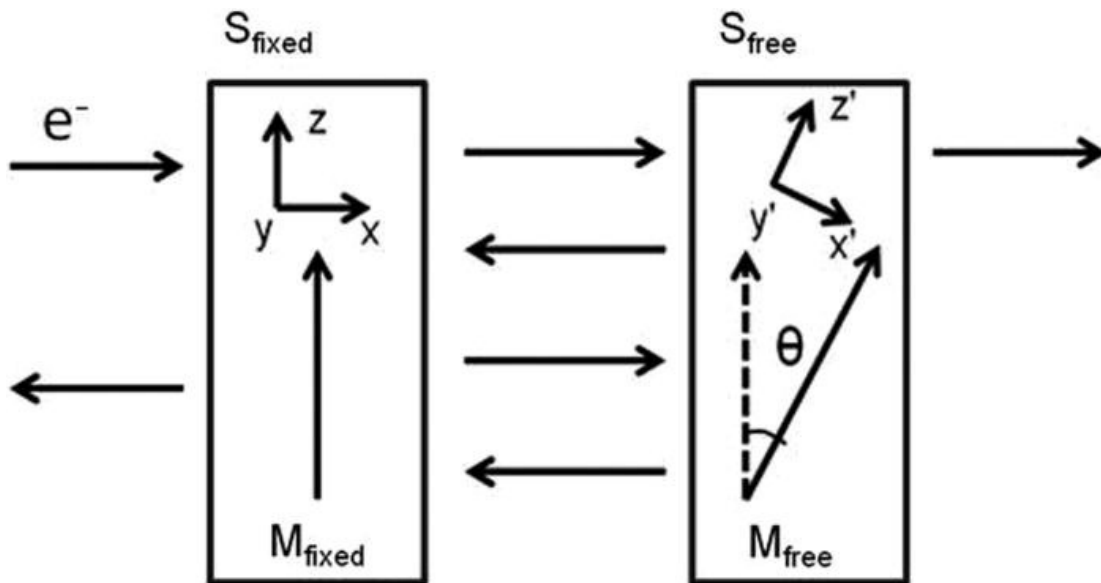
Figure 2.1: Two magnetic layers with noncollinear magnetizations. (x, y, z) and (x', y', z') are the local coordinate systems, such that **z,z'** is parallel with the local magnetization. Arrows into and out of the magnetization layer represent transmitted and reflected electrons.

This spin-dependent potential is expanded in spin space. The basis for the spin space is set separately for different magnetic layers, similar to Slonczewski's and Urazhdin's approach. For the fixed layer, the two spin eigenstates are $|1>=\begin{pmatrix} 1 \\ 0 \end{pmatrix}$ and $|-1>=\begin{pmatrix} 0 \\ -1 \end{pmatrix}$. For the free layer, they are $|1'>=\begin{pmatrix} \cos(\theta/2) \\ \sin(\theta/2) \end{pmatrix}$ and $|-1'>=\begin{pmatrix} \sin(\theta/2) \\ -\cos(\theta/2) \end{pmatrix}$. The Hamiltonians for two layers have the same matrix form in the local spin basis. The dimensions of the **S** matrix are 4×4. In each layer's original basis, scattering matrices of the fixed layer and free layer have the

same form[35]:

$$\mathbf{S} = \begin{pmatrix} R & T \\ T & R \end{pmatrix}. \tag{2.2}$$

S fixed layer basis:$| \pm 1 > \otimes | \pm 1 >$ and S free layer basis:$| \pm 1' > \otimes | \pm 1' >$.

Reflection matrix $\mathbf{R}$ and transmission matrix $\mathbf{T}$ are both 2×2 matrices. The sum

of $\mathbf{T}_{11}(\mathbf{T}_{22})$ and $\mathbf{R}_{11}(\mathbf{R}_{22})$ is 1 for conservation of spin moment. We assume that

the transmission probability of spin $\uparrow(\downarrow)$ electrons equals the proportion of spin

$\uparrow(\downarrow)$ electrons at the Fermi level. Thus, we find ϵ as the minority transmission

probability, while 1-ϵ is the majority transmission probability, where P=1-2ϵ.

$$\mathbf{R} = \begin{pmatrix} 1 - \epsilon & R_{12} \\ R_{21} & \epsilon \end{pmatrix}, \quad \mathbf{T} = \begin{pmatrix} \epsilon & T_{12} \\ R_{21} & 1 - \epsilon \end{pmatrix}. \tag{2.3}$$

Diagonal elements in the $\mathbf{T}$ and $\mathbf{R}$ matrices represent conservation of electron

magnetic moment during the scattering. We take the off diagonal elements as

zero. This implies that we are neglecting spin flip scattering in the middle (non-

magnetic) layer of a trilayer sample. The impact will depend on device structure,

as discussed later. We also assume that the $\mathbf{S}$ matrix has mirror symmetry for

incident currents from either side. To get the final transmission matrix $\mathbf{T}_{final}$

from two scattering matrices, we need to transform them into the same basis. For

incoherent transport, the spin probabilities rather than the wave functions must

be transformed by the operator $\mathbf{O}(\theta)$, as follows.

$$\mathbf{O}(\theta) = \begin{pmatrix} \cos^2(\theta/2) & \sin^2(\theta/2) \\ \\ \sin^2(\theta/2) & \cos^2(\theta/2) \end{pmatrix}. \tag{2.4}$$

This implies

$$\mathbf{R}_{free} = \mathbf{O}(\theta/2)^{\dagger}\mathbf{R}\mathbf{O}(\theta/2), \qquad \mathbf{T}_{free} = \mathbf{O}(\theta/2)^{\dagger}\mathbf{T}\mathbf{O}(\theta/2). \tag{2.5}$$

So, $\mathbf{R}$ and $\mathbf{T}$ matrices in the fixed layer basis are

$$\mathbf{T}_{free} = \begin{pmatrix} \epsilon(1-\beta)^2 + (1-\epsilon)\beta^2 & \beta(1-\beta) \\ \\ \beta(1-\beta) & \epsilon\beta^2 + (1-\epsilon)(1-\beta)^2 \end{pmatrix}, \tag{2.6}$$

$$\mathbf{R}_{free} = \begin{pmatrix} \epsilon\beta^2 + (1-\epsilon)(1-\beta)^2 & \beta(1-\beta) \\ \\ \beta(1-\beta) & \epsilon(1-\beta)^2 + (1-\epsilon)\beta^2 \end{pmatrix}.$$

In a tri-layer CPP structure, some electrons going through the layers may be reflected infinitely between the first and third magnetic layers[36], as in Fig. 2.1. To include multiple reflections between two magnetic layers, $\mathbf{T}_{final}$ is[35]

$$\mathbf{T}_{final} = \mathbf{T}_{free}[\mathbf{I} - \mathbf{R}_{fixed}\mathbf{R}_{free}]^{-1}\mathbf{T}_{fixed}. \tag{2.7}$$

Contact conductance[37] is proportional to the sum over the four $\mathbf{T}_{final}$. Therefore, an analytic equation for tri-layer conductance is

$$\mathbf{G} \sim \sum_{ij} \mathbf{T}_{ij} = \left(-2 + \frac{2 + 4\beta}{1 + (-1+\epsilon)\epsilon + \beta(1 - 2(-1+\epsilon)\epsilon)} \right). \tag{2.8}$$

Converting conductivity to resistivity ρ, we define the MR ratio$=(\rho(\theta)-\rho(\theta=0))/(\rho(\theta=\pi)-\rho(\theta=0))$.

$$MR\ ratio = \frac{1-\beta}{1+\chi\beta}, where\ \chi = \frac{1-2\epsilon+2\epsilon^2}{\epsilon-\epsilon^2}. \qquad (2.9)$$

We also calculate MR angular dependence, not including multiple reflections

$$\mathbf{T}'_{final} = \mathbf{T}_{free}\mathbf{T}_{fixed}. \qquad (2.10)$$

This yields a linear angular dependence, as shown in a previous paper[33] when multiple reflections are not considered.

2.2 Results and Discussions

The same general form of angular dependence is found in different models, although χ is different. Clearly, our approach depends on the polarization in the ferromagnet. Permalloy polarization is sensitive to experimental fabrication. Differences also arise from the measurement method. Using the same definition of polarization as we use, Meservey et al. found a value of 0.25 using the superconductor junctions tunneling method[38] with an Al_2O_3 tunneling barrier at 0.4 K. Another method to measure polarization is point contact Andreev reflection (PCAR)[39] where 0.37 permalloy polarization is obtained. These two values correspond to χ 2.27 and 2.56, respectively. In the model of Urazhdin et al, χ is

equal to the ratio of bulk resistance to interface resistance of the ferromagnetic layer: 2.8 is obtained[34] from the measured CPP GMR of the Valet-Fert model. In Slonczewski's model[27], $\chi = [1/2]AG(R_+ + R_-) - 1$, where $R_+(R_-)$ is the bulk and interface resistance for the different spin moments, A is the nanowire cross-section, and G is related to Sharvin ballistic conductance. With $R_+(R_-)$ from[40] the Valet-Fert model, χ is -0.715. A fit to the data shown in Fig. 2.2 suggests[34] χ is 2.0. Therefore, either of our polarization values produces a better fit to the experimental data than previous theoretical approaches. This can be seen in Fig. 2.2, which shows the three model results that include reflected electrons as well as the simple transmission model without reflected electrons that has sometimes been used previously.

Experimental work[41] suggests that the spin flip scattering length in Cu is about 200 nm. These spin flips will diminish the impact of repeated scattering between ferromagnetic layers. They are probably the major source of our small exaggeration of the curvature of the magnetoresistance curve (Fig. 2.2). We extend our model to a multilayer nanowire 10 μm in length and 90 nm in diameter. One complexity is that the magnetization angle in each ferromagnetic layer is not known from experiment. We use the Landau-Lifshitz-Gilbert equation[42] to simulate the magnetization angles in equilibrium. The effective field includes anisotropy field, magnetostatic interaction field, and external applied field. We
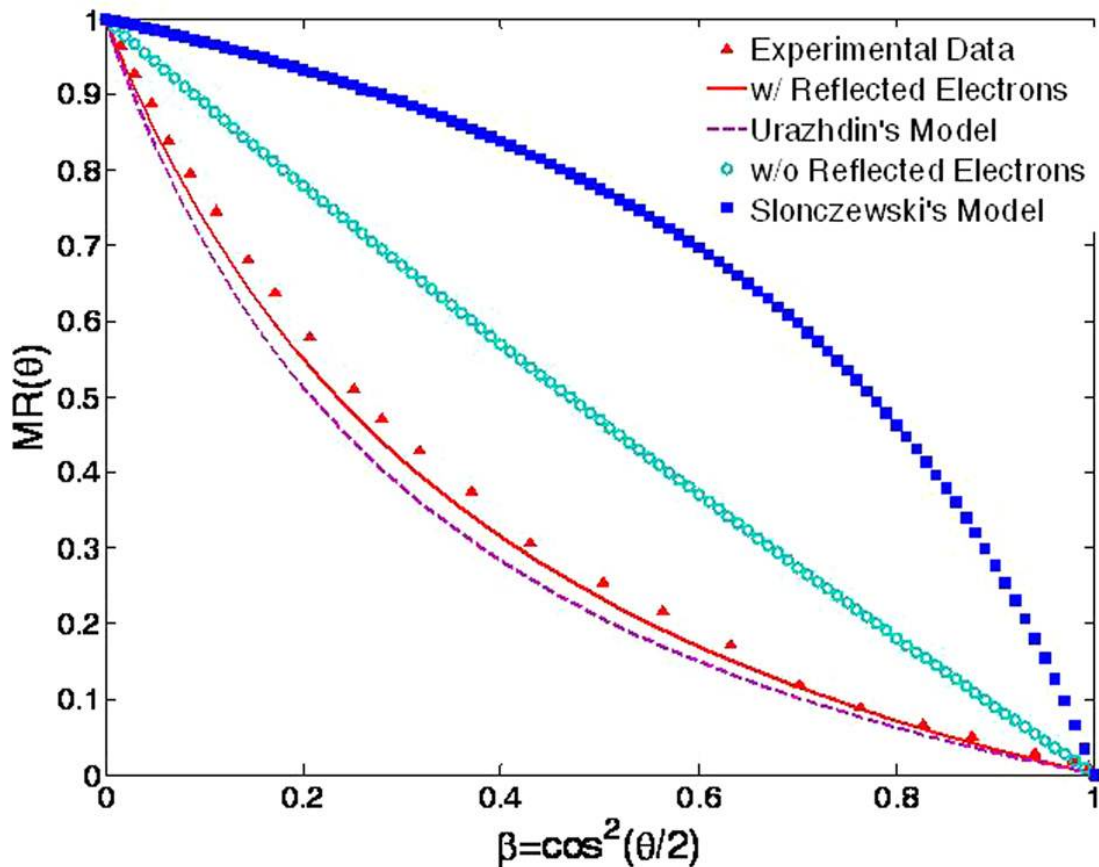
Figure 2.2: Angular dependence of MR vs $\beta = \cos^2(\theta/2)$. Experimental sample structure is Py(6)/Cu(10)/Py(12) in nanometers. CPP resistance is measured at 4.2 K.

take the magnetization of the cobalt to be 1400 emu/cm^3 and the anisotropy to be randomly distributed with magnitude 2.0×10^6 erg/cm^3. We calculate the magnetoresistance of the nanowire considering all reflections between all layers. Fig. 2.3 shows the comparison of our prediction with experimental data[11]. It can be seen that our theory slightly overestimates the magnitude of the magnetoresistance when using the experimental cobalt spin polarization[39] of 0.35. The

difference may be caused by our neglect of spin flip scattering in the copper layers,

which becomes more important for this much longer sample.
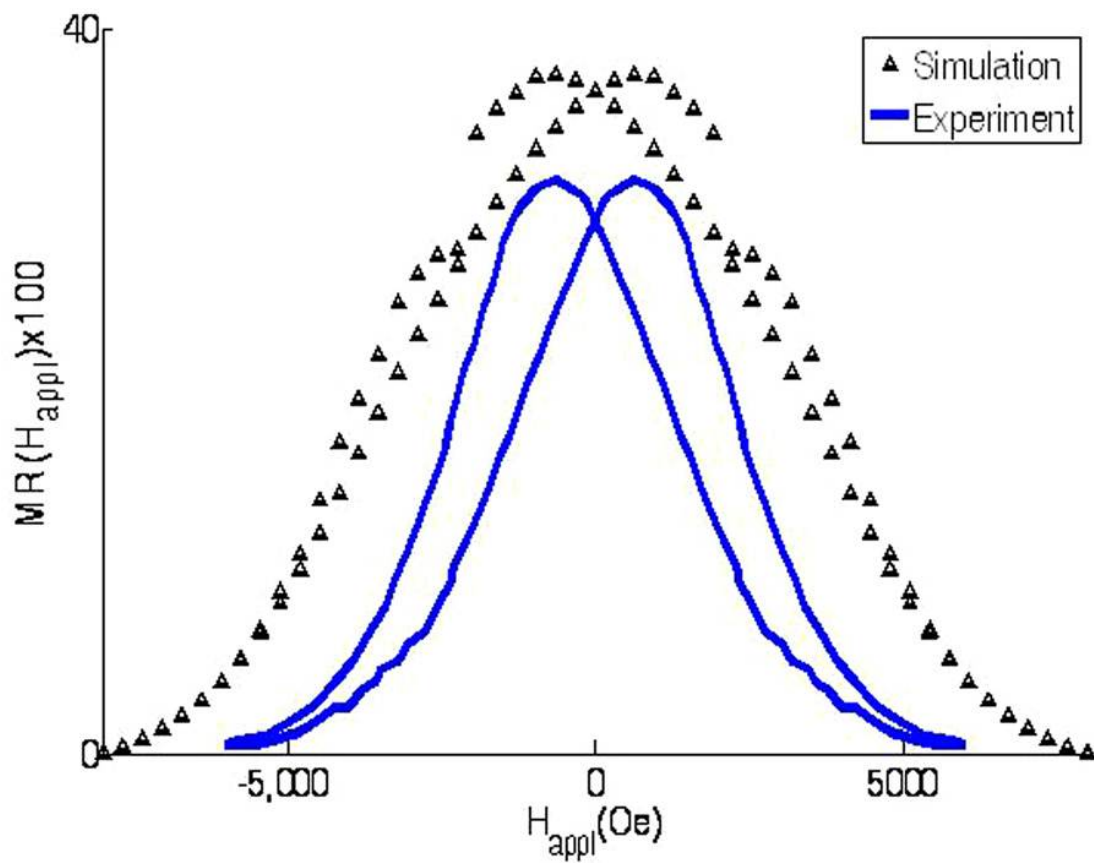
Figure 2.3: Multilayer experimental data (Ref. [11]) and simulation with multiple reflections. MR=$(R(H_{appl})$-$R(H_{sat}))/R(H_{sat})$. The experimental sample structure is $[Co(10\ nm)/Cu(5\ nm)]_{1333}$ measured at 77 K.

2.3   Conclusion

We use incoherent scattering matrices to calculate the angle dependent magnetoresistance and find analytic expressions for a tri-layer current-perpendicular-to-plane nanowire. We find that the non-linearity of magnetoresistance versus $\beta = \cos^2(\theta/2)$ can be quantitatively explained by reflected electrons using only experimental spin polarization as input. We extend this model to a multilayer nanowire and find the simulation approximately matches experiment.In conclusion, an alternate approach for treating multiple reflections is introduced. Benefits include quantitative predictions for MR in complex systems without use of adjustable parameters.

Chapter 3

Synchronization of Spin Transfer Torque Nano-Oscillator

The prediction of magnetization manipulated through a spin polarized electric current[21, 22] has stimulated tremendous research interest in recent years[43]. The current-induced stable magnetization precession device, named the spin torque nano-oscillator (STNO), provides an alternative to a standard LC-tank voltage-controlled oscillator (VCO) and shows intriguing advantages of versatile frequency tunability, nanoscale size, broad working temperature, and easy integration with standard silicon technology over a VCO. These characteristics make the STNO a very attractive novel device for future applications, e.g. chip-to-chip micro-wireless communications.

The system including a single STNO has been studied extensively experimentally[44, 45] and theoretically[46]. However, the power from a single STNO remains in the low nW range[44], but applications would greatly benefit from microwatt power levels. Although a magnetic tunnel junction (MTJ) may produce a large voltage signal benefiting from large magnetoresistance[47] to 400% at room temperature, the maximum bias current is limited by the barrier breakdown voltage ($\sim$1.0V) and thus the power is limited to sub microwatt[48]. Also, the linewidth as a measure of the phase noise in MTJ is rather large($\sim$100MHz). One approach to achieving a narrow linewidth and a large output power simultaneously is the excitation of vortex dynamics in a MTJ or metallic spin-valve but the oscillation frequency is limited to sub-GHz range[49]. Another approach is to synchronize arrays of STNOs by local or non local mechanisms. The spin-wave coupling in point-contact geometry only weakly couples more than two closely spaced STNOs because of the fractional oscillator distance relative to the spin wave length[50, 51]. Besides, the coupling length is only efficient over the spin wave decay length, i.e., around $1\mu m$. Thus, the most promising approach is a long range coupling through STNOs self-emitted microwave currents, predicted by Grollier, Cros and Fert[52]. They argued that the oscillators of an electrically connected network can be mutually phase locked through the microwave feedback current, although they neglected thermal noise and long range magnetostatic interaction. As the

coupling strength is proportional to the microwave current, it is imperative to gain insight into the magnetoresistance(MR) ratio necessary for synchronization. This will allow the design and optimization of the STNO-based spintronic device. The previously neglected thermal noise produces a broadened peak and is detrimental to reaching a phase-lock state, while in contrast, the magnetostatic field can enhance the coupling.

We use the Landau-Lifshitz-Gilbert equation to describe the dynamics of each individual oscillator and study in detail the MR ratio threshold necessary to achieve phase-locking under two common magnetic nonuniformities: variation in the anisotropy and saturation magnetization magnitude. We check the effect of thermal fluctuation on the required minimum MR ratio. The interaction between the microwave current coupling and the long range coupling mechanism provided by the magnetostatic field is also studied. The interaction effect on the MR ratio threshold is obtained.

3.1   Method

Magnetization dynamics in the GMR serially connected nanopillar can be accurately described using the Landau-Lifshitz-Gilbert equation.

$$\frac{d\hat{m}_i}{dt} = -\gamma\hat{m}_i \times (\vec{H}_{eff} + \vec{\eta}) + \alpha\hat{m}_i \times \frac{d\hat{m}_i}{dt} + \frac{I_s(t)P\hbar}{2V_f e M_s}\hat{m}_i \times (\hat{m}_i \times \hat{M}), \quad (3.1)$$

where γ, α, and $\hat{m}_i$ are the gyromagnetic ratio, the damping constant, and the unit vector of the free layer magnetization of the ith STO (i=1:10). The effective field $\vec{H}_{eff}$ includes the external field, the magnetocrystalline anisotropy and any magnetostatic contributions that may be present. Both the external and anisotropy field are in the x direction. $\vec{\eta}$ is the thermal fluctuation field[53], described by a white noise with amplitude dependent on the temperature and the free layer volume V_f. The third term on the right is the spin torque generated by the spin current. The current is polarized by the fixed layer magnetization $\hat{M}$, in the $+\hat{x}$ direction. $\hbar$ is Plancks constant, e is the magnitude of the electron charge, P is the polarization constant and M_S is the free layer saturation magnetization. $I_S(t)$ includes the dc source current and ac self-generated current. Under the first order estimation of the circuit[52],

$$I_S(t) \;=\; I_{dc}(1 + \frac{1}{R_{load}/N\bar{R}+1} \frac{\sum \cos(\theta_i)}{N} \frac{MRratio}{2.0 + MRratio}), \qquad (3.2)$$

where N is the number of oscillators. θ_i is the angle between the magnetization in the free layer and fixed layer. R_{load} is 50Ω for the bias tee in the circuit[54]. $\bar{R} = (R_P + R_{AP})/2$ is the average resistance of the parallel and anti-parallel states of a single STNO where R_P=10Ω. The material parameters for Co in the following calculations are α=0.007, P=0.35, M_S=1352emu/cm^3, H_{an}=500Oe. H_{ext}=2000Oe and the current is 9mA. The current density is in the order of

$10^7 \ A/cm^2$ to $10^8 \ A/cm^2$.

The geometry of serially connected STOs can be implemented in the type of nanowires which have been developed for CPP-GMR experiments[55]. The standard structure is a multilayer nanowire composed of ferromagnetic(FM) and normal metal(NM) layers, such as $\{\text{FM1(fixed)/NM1/FM2(free)/NM2}\}_N$, where N is the number of oscillators. When the magnetization in FM2 layer is excited to a stable oscillation state, FM1 functions as both a polarizer of injected charge current depolarized by NM2 and as an analyzer to record the generated voltage signal. Positive injected dc current is defined as electrons flowing from the free to the fixed magnetic layer. The free layer is assumed to be a typical Co thin film patterned with a thickness of 3nm and an elliptical shape of dimensions 130nm×70nm, shown in Fig. 3.1. In this case, at least 10 coupled oscillators are required to produce power approaching μW, for a reasonable MR range of 1~10%.
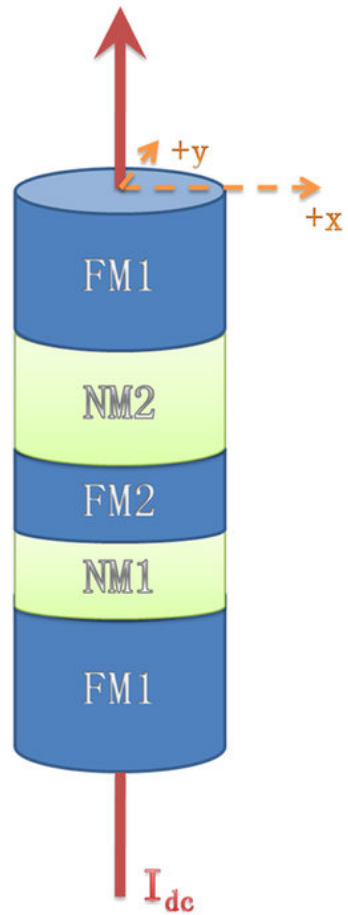
Figure 3.1: This structure is repeated to implement a serial array of STOs. The current is perpendicular to the plane. The x axis is along the major axis and y axis is along the minor axis of the ellipse.

3.2   Results and Discussion

Fig. 3.2(a,b) shows the sharp transition from distinct oscillation states to synchronized states, occurring for dispersed anisotropies or dispersed saturation magnetizations in stacked STNOs. The anisotropy and magnetization dispersion follows the same rule: $H_{an} = H_{an0} + (i1)/(N1) \times \delta H_{an}$ (or $M_S = M_{S0} + (i1)/(N1)\delta M_S$), with i varying between 1 and 10. $\delta H_{an}(\delta M_S)$ is defined as the amount of anisotropy(saturation magnetization) difference between consecutive free layers. Under both conditions, the synchronization process begins when the MR ratio is above 5%. The MR ratio threshold MR_{th} to achieve the completely synchronized state is 8%, while below this threshold, the total oscillation state is partially synchronized with individual adjacent peaks merged into several multiple peaks. The frequency increases monotonically in the MR ratio range where the synchronization mechanism occurs. This trend may be caused by the positive dc component in the self-generated microwave current. In the synchronized state, the peak is similar to a delta function in that its linewidth is nearly zero. The amplitude has a small oscillation with MR ratio caused by the finite integration time (8.4ms). The time scale of the dynamics for the transition from the static state to synchronization is about one nanosecond for the different MR ratios above the threshold. We also check the MR_{th} as a function of δH_{an} and δM_S as shown

in Fig. 3.2(c,d). The threshold is linearly dependent on δH_{an} and δM_S. The frequency range Δf, defined as the intrinsic frequency difference of N oscillators, is induced by the non-uniform properties of H_{an} or M_S: it is found that the MR_{th} is also linearly dependent on Δf. Although the coupling appears to be more difficult under the condition of saturated magnetization variation, considering its influence on both the excited oscillation energy and the microwave feedback, the MR_{th} can be viewed as determined only by the resulting frequency range. Based on this prediction, the observed experimental frequency dispersion[50] of 1.25% needs about 4.7% MR ratio to achieve phase-lock, which is achievable in a CPP-GMR structure.

While the noise in the magnetic system caused by thermal fluctuations is detrimental to phase locking, the self-generated ac current reduces the incoherent phase found in multiple oscillator states. This helps to enhance the peak height and reduce the peak linewidth, as shown in the inset of Fig. 3.3(b). The linewidth decreases to a minimum value when the array of oscillators achieves a completely synchronized state, in Fig. 3.3. The threshold MR obtained increases with temperature under both conditions of M_S and anisotropy dispersion, as shown in Fig. 3.4(a). The dependence on temperature is approximately linear for the volume considered ($\sim 2.1 \times 10^5$ μm^3). The MR_{th} for $\delta H_{an}/H_{an0}$=1.8 and $\delta M_S/M_{S0}$=0.03 is 13% and 14% respectively at room temperature 300K. We inquire into the peak
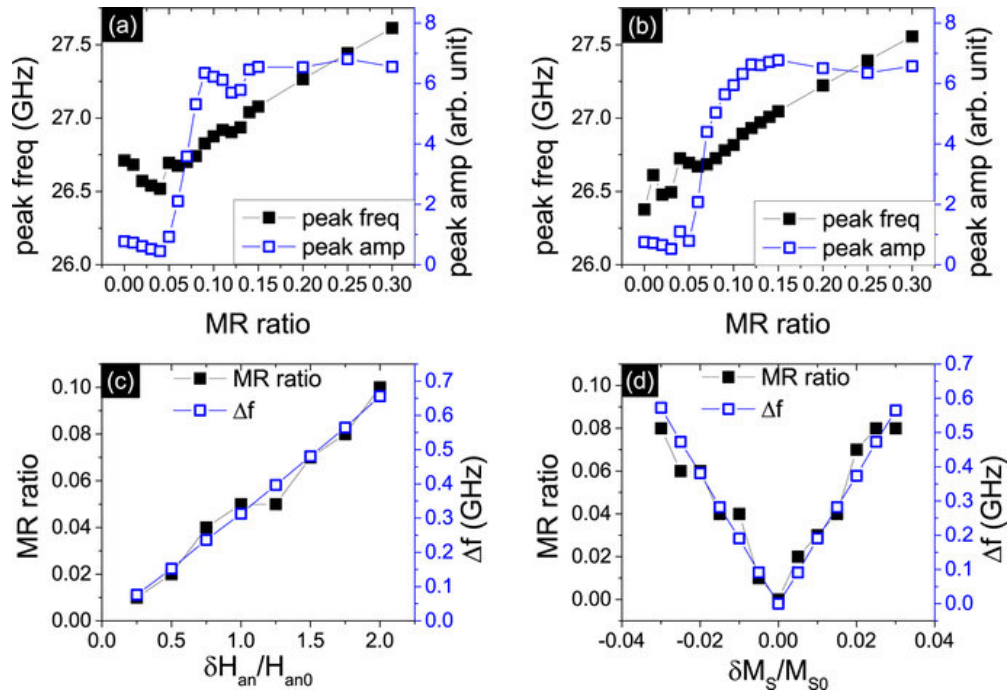
Figure 3.2: (a,b) The peak frequency and peak amplitude of the voltage signal versus MR ratio for the 10 non-uniform serial STNOs under the conditions of (a) $\delta H_{an}/H_{an0}$=1.8 and (b) $\delta M_S/M_{S0}$=0.03 without thermal fluctuation. Both the MR ratio thresholds are 8%. The peak frequency and amplitude at MR ratio=0% are the mean values from 10 separate peaks. (c,d) The MR ratio threshold and frequency dispersion versus (c) $\delta H_{an}/H_{an0}$ and (d) $\delta M_S/M_{S0}$.

profile at these threshold points and compare the phase-locked state of N oscillators with one single oscillator, in Fig. 3.4(b). This self-generated microwave is quite efficient in decreasing the noise at room temperature, and the peak of the array of oscillators is tremendously narrowed compared with the single STNO.

Magnetic feedback from the time dependent dipole field between the STNOs
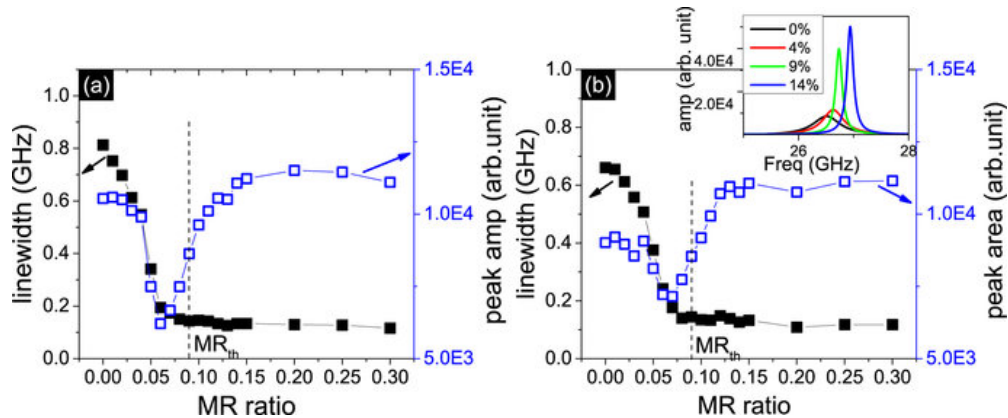
Figure 3.3: (a,b) The linewidth and peak area of the maximum peak in the voltage signal spectrum versus MR ratio for the 10 non-uniform serial STNOs under the condition of (a) $\delta H_{an}/H_{an0}$=1.8 and (b) $\delta M_S/M_{S0}$=0.03 at T=50K. The corresponding MR ratio thresholds are both 9%. The inset of (b) shows the spectra of the amplitude versus frequency for the set of 10 oscillators when the MR ratio is 0, 4%, 9% and 14% for the first order excitation frequency.

can enhance the coupling at a proper distance and reduce the MR ratio requirement for the phase locked state. We use the finite difference integration technique (per oscillators are divided into more than 7000 elements in simulation) to calculate the magnetostatic interaction. We study the coupling between two non-identical oscillators with $\delta H_{an}/H_{an0}$=1.8 at T=0K. When only microwave current is included, the MR ratio threshold is 24% in Fig. 3.5(a). This is higher than the case of 10 oscillators because 2 oscillators generate less ac current. When the ac dipole field between two oscillators is included at a distance d of 22nm (d is the distance between two oscillation layers in the two STNOs), the phase locked state can be achieved at a low MR ratio of 2%. Under this MR ratio, the ac current is
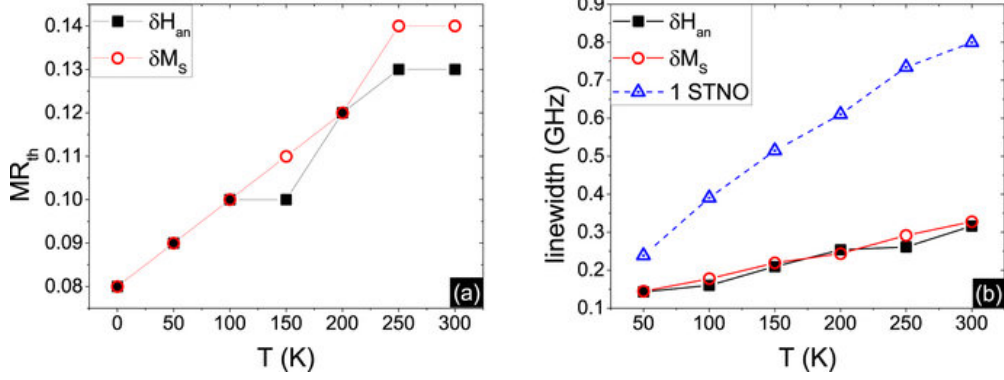
Figure 3.4: (a) MR ratio threshold for the array of 10 non-uniform serial STNOs under the conditions of $\delta H_{an}/H_{an0}=1.8$ and $\delta M_S/M_{S0}=0.03$ at variable temperatures. (b) The linewidth of the voltage signal generated by 10 oscillators at the MR_{th} at variable temperature under the corresponding anisotropy and magnetization saturation conditions. The linewidth of a single oscillator is shown for comparison.

not sufficient to reach synchronization using only the current coupling mechanism. Thus the assistance from the ac dipole field is important to the in-phase synchronization. However, the combined mechanisms of magnetic and electric feedback is more complicated than the electric feedback mechanism alone. We observe oscillatory behavior in Fig. 3.5(b) of the predicted peak amplitude versus MR ratio at a fixed d of 22nm under the combined mechanisms, while for the electric feedback alone, the two oscillations stay coupled in phase after overcoming the MR ratio threshold. This oscillatory behavior also happens when varying d at a constant MR ratio of 0.05, shown in Fig. 3.5(c).

To analyze the complex oscillatory behavior, we investigate the out-of-plane oscillation modes $\hat{m}_i = (r_i \cos(\phi_i), r_i \sin(\phi_i), m_{iz})$, where r_i and ϕ_i is the amplitude
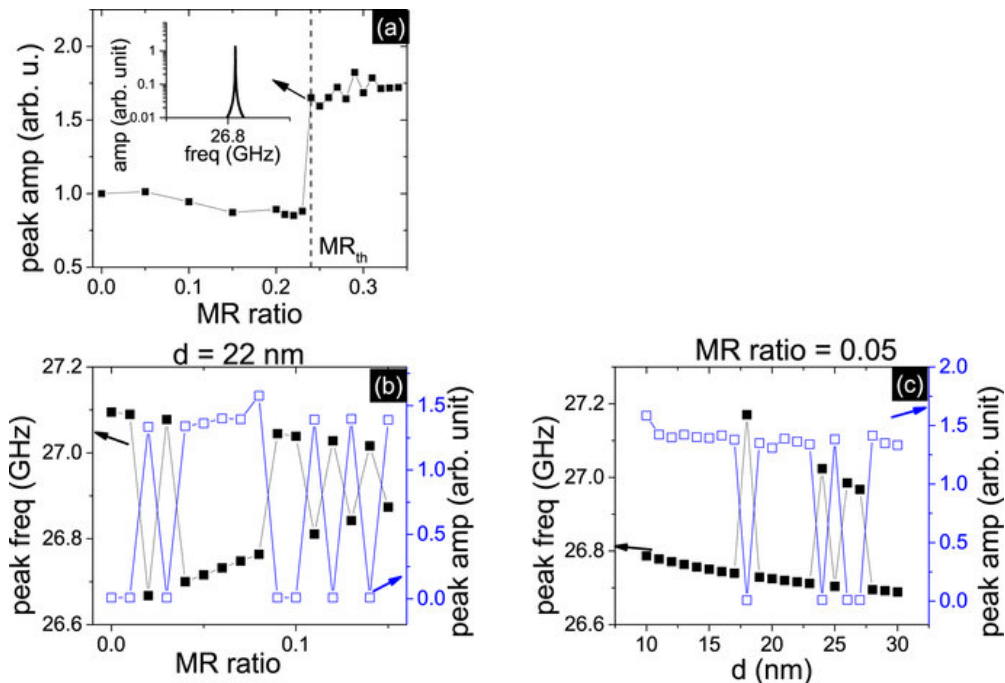
Figure 3.5: (a) The peak amplitude of the voltage signal versus MR ratio for 2 non-uniform serial STNOs under the condition of $\delta H_{an}/H_{an0}$=1.8 at T=0K, when only the current feedback mechanism is included. The inset is the spectrum of the amplitude vs frequency at the MR ratio threshold of 24%. (b)The peak frequency and amplitude versus MR ratio when the distance d between two free layers is fixed at 22nm. (c) The peak frequency and amplitude versus distance d when MR ratio of the STNOs is fixed at 0.05. In both (b,c), the combined mechanisms of current and magnetic feedback are considered.

equal to and the phase of the i (i=1,2) oscillator and m_{iz} is a constant. By Fourier transform of $m_i^+ = m_{ix} + \imath m_{iy}$, we obtain the polarization of the out-of-plane oscillation mode. The polarization is defined as +1 for counterclockwise rotation, and the polarization is 1 for the converse case. We find that for small output power, the two oscillators are in the same polarizations, while for large power, the two oscillators have opposite polarizations, shown in Fig. 3.6(a,b).

Small generated power, which decreases nearly to 0, implies the mix oscillation is out of phase, as shown in the insets. We examine the phase difference $\phi_1 - \phi_2$ and it closely equals to π when the two oscillators have the same polarization in Fig. 3.6(d). For the opposite polarization states, the phase sum $\phi_1 + \phi_2$ is approximately 0 in Fig. 3.6(c), which implies that the mix component is in phase and the m_{iy} component is out of phase.

To illustrate the synchronization via the ac dipole field and self-generated microwave current, we study the phase dynamics of the STNOs in the extended Kuramoto model[46, 56]. The energy E_i injected into the individual oscillator from the feedback mechanisms is computed in one period. Here, the spin torque field produced by the ac current is neglected, because its amplitude is less than 0.01 of the dipole field $\vec{H}_{dip}$ amplitude.

$$
\begin{aligned}
E_i &= -\frac{1}{2}M_sV_f \oint \vec{H}_{dip}d\hat{m}_i; \\
&= +\frac{1}{2}M_sV_f \oint r_ir_j(-T_x\sin\varphi_i\cos\varphi_j + T_y\cos_\varphi\sin\varphi_j)d\varphi_i; \\
&= \pm E_0\frac{T_y \mp T_x}{2}\sin(\varphi_1 \pm \varphi_2). \quad i \neq j
\end{aligned}
\tag{3.3}
$$

Here, $E_0 = \frac{1}{2}M_s^2V_fr_ir_j$. T_x and T_y are the diagonal elements of the magnetostatic tensor. The sign of $\pm$ corresponds to the opposite (same) polarization. Following references [46] and [55], energy E_i can be treated as a perturbation, compared to the excited state energy $E_{0i} \sim 2\pi(M_sm_{iz})^2$. The modified frequency δf_i due to
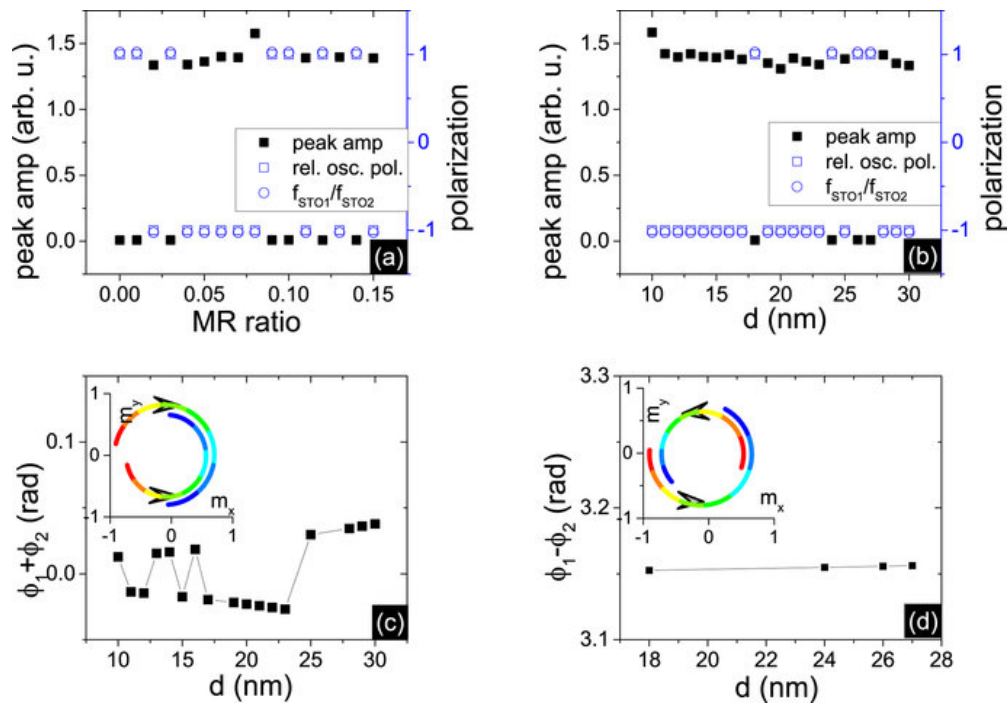
Figure 3.6: The peak amplitude, relative oscillation polarization of the output voltage signal and the ratio f_{STO1}/f_{STO2} of estimated intrinsic frequencies of 2 non-uniform STNOs. (a) versus MR ratio at d=22nm (b) versus distance d at MR ratio=0.05 under the condition of $\delta H_{an}/H_{an0}$=1.8 at T=0K. The relative oscillation polarization is calculated as polarization of STO_1 over polarization of STO_2. (c) the phase sum $\phi_1 + \phi_2$ versus d when the polarization state in fig(b) is opposite. (d) the phase difference $\phi_1 - \phi_2$ versus d when the polarization state in fig(b) is the same. The insets shows the time evolution projection into the xy plane of the normalized magnetization vector of 2 STNOs for nearly one period. The color depicts the time: red refers to the initial time while blue refers to the final time. The projection of STO_2 is reduced to reveal the phase difference of the two oscillators.

$E_i = (\partial f_i / \partial E_{0i}) E_i$. Thus the phase dynamics for the STNOs are

$$\frac{1}{2\pi} \dot{\varphi}_1 = +f_1 + \frac{f_1}{E_{01}} E_1; \tag{3.4}$$

$$\frac{1}{2\pi} \dot{\varphi}_2 = \mp f_2 \pm \frac{f_2}{E_{02}} E_1. \tag{3.5}$$

For the synchronized STNO array, both oscillators are in resonance frequency f_{res}. Thus the coupling parameter, which controls the frequency range consistent with synchronization, is

$$\Lambda_{\mp} = \frac{f_2 - f_1}{2} = \pm \frac{\partial f}{\partial E} E_0 \frac{T_y \mp T_x}{2} \sin(\varphi_1 \pm \varphi_2). \tag{3.6}$$

$(\partial f_i / \partial E_{0i})$ is treated as the same constant for the two STNOs in the first order estimation. From the $\Lambda_{\mp}$ in Fig. 3.7(a), we deduce a conclusion that the case of opposite polarization has weaker coupling than the case of same polarization because of the opposing effects of T_y and T_x. So if the intrinsic frequency difference $\delta f = f_2 f_1$ exceeds the coupling strength for opposite polarization, the same polarization is chosen to achieve the resonant but anti-phase state. Λ_{-} also predicts that the opposite polarization state is impossible for a STNO array of circular shape. It has no capability of coupling the non-uniform oscillators as T_x completely cancels T_y. We find that in the resonant state of two STNOs of circular shape, anti-phase out-of-plane oscillation is always preferred.

To confirm the coupling parameters analysis, we estimate the intrinsic frequency difference Δf. The approximate intrinsic frequency f_i equals to $\frac{\gamma}{2\pi}| -$
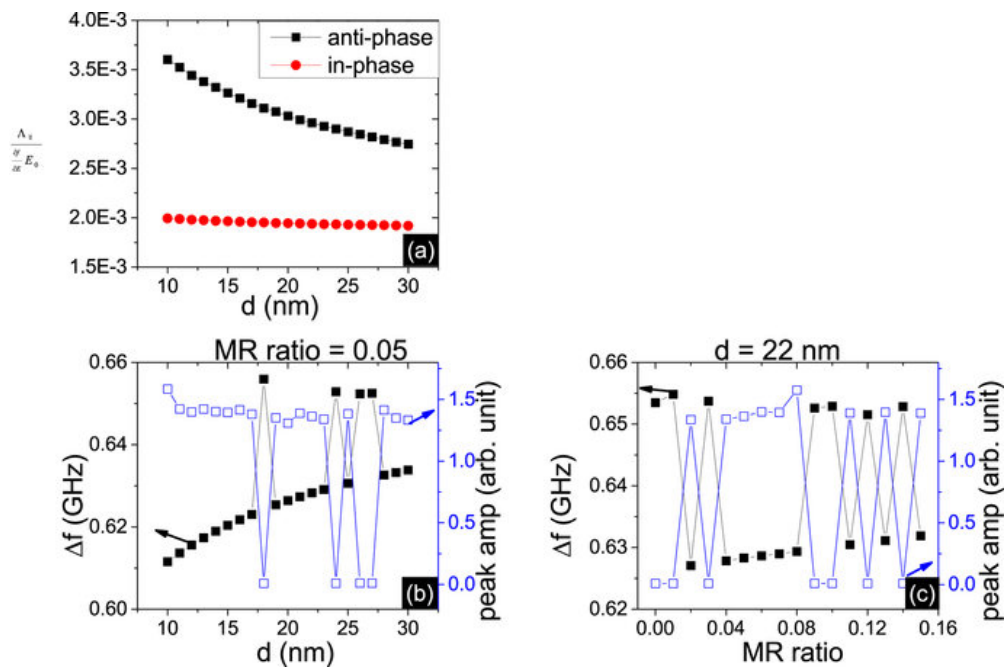
Figure 3.7: (a) Calculations of coupling parameters $\Lambda_{\mp}$ using Eq.(4) for the two polarization states, taking the phase data from the simulation result. Estimated intrinsic frequency difference Δf and the peak amplitude of the output voltage signal (b) versus d at MR ratio=0.05 (c) versus MR ratio at d=22nm.

$4\pi M_s m_{iz} - T_z M_s m_{jz}|$. Here, T_z is the diagnonal element of the magnetostatic tensor and is chnegative. If the z components of two STNOs have opposite signs, which represent the out-of-plane direction of the oscillation modes, Δf equals to $\frac{\gamma}{2\pi}(4\pi + T_z)M_s\Delta m$. For the same sign of m_{iz}, Δf equals to $\frac{\gamma}{2\pi}(4\pi - T_z)M_s\Delta m$. It is reasonable to treat Δm unchanged in both polarization states in the perturbation scheme. Thus the oscillation state with the same sign of m_{iz} has larger intrinsic frequency difference. From the simulation results, Δf under the same sign of m_{iz} is in the range of 0.65 to 0.67GHz and needs more coupling to lock phase, compared with Δf under the case of the opposite signs in the range of 0.61 to 0.63, in Fig. 3.7(b,c). Thus the relative direction of m_{iz} chooses the polarization state directly to be the same or opposite. This connection is verified for both conditions of fixed distance or fixed MR ratio, as shown in Fig. 3.6(a,b). The m_{iz} evolution is determined interactively by magnetostatic and current feedback mechanism and is difficult to predict. Therefore device design may require a technique for selecting the starting point in order to guarantee the same phase locked state for each use.

3.3 Conclusion

In conclusion, we obtain the minimum MR ratio requirement for synchronization subject to the two long range coupling mechanisms of self-induced microwave current and dipole field. The MR ratio threshold is determined by the frequency dispersion (caused by non-uniform properties). It increases linearly as thermal fluctuations induce dephasing in the serial array of STNOs. At room temperature, the MR ratio requirement is achievable in GMR devices for physical frequency dispersion. Synchronization occurs with a MR ratio 14% and volume $\sim 2.1 \times 10^5 \mu m^3$ at room temperature for an experimental frequency dispersion. When the interaction between self-induced dipole field and microwave current is included, the set of oscillators shows an oscillatory phase between π and 0 when the dipole field or MR ratio is varied. The proper coupling interaction benefits the synchronization so that the required MR ratio for synchronization is below the value for coupling by current alone.

Chapter 4

Ferromagnetic Damping in

Multiple Systems

The determination of the ferromagnetic damping α is both a fundamental scientific problem and technologically important for spintronic devices. It reflects the elimination of the magnetic energy and determines the dynamics in magnetic systems, e.g., switching [57, 58]. The speed of the magnetic state change is generally proportional or inversely proportional to α based on the state manipulating method. In magnetic recording controlled by the magnetic field [59, 60], large α is preferred to increase the writing speed. In electrically manipulated spintronic devices [61, 62], the magnetic configuration can be changed by the spin-torque

70

effect that is produced by the electric current through the device. The minimization of α is required to increase the energy efficiency. Materials with small α substantially reduce the critical current required to switch the stored state.

It is imperative to gain insight into the many sources of α, including magnon-magnon interaction mediated by defects[9], four-magnon scattering[10] and magnon-electron interaction[63]. The most intrinsic source is Kambersky damping[64], representing magnetic energy lost to the lattice through the spin-orbit interaction(SOI). This mechanism is mostly explored in traditional bulk[65, 66, 67, 68] and thin film[69] transition materials: Fe, Co, and Ni. Calculation of α has been approached in torque-correlation theory[64], linear response theory[70], and scattering theory[71], respectively. The Kambersky mechanism is especially prominent in the high magnetocrystalline anisotropy materials because high magnetocrystalline anisotropy implies strong SOI.

In this chapter, we first introduce our method to implement method of Kambersky torque-correlation damping model and apply this method to multiple ferromagnetic systems. We start with a traditional ferromagnetic material: bulk body-centered-cubic(bcc) Fe, to verify the accuracy of our method. Results for damping dependence on material properties and spin orientation are shown in bulk bcc Fe. We then extend this method to $L1_0$ ordered and disordered alloys FePt, FePd, CoPt and CoPd. These materials have high magnetocrystalline anisotropy.

Thus Kambersky damping mechanism plays a key role in the energy dissipation process in these materials. We investigate the effect of defects, which is unavoidable in experimental fabrication, on damping. Since the study of damping has recently shifted towards ferromagnetic thin metallic films [72, 73, 74, 75, 76, 77], due to their wide application in both advanced spintronic and magnetic recording devices, we study the damping in superlattices with high magnetocrystalline anisotropy. An extra interfacial damping, due to the broken symmetry of the electronic structure at the interface of the layered structures, contributes to the total damping observed in experimental measurement. Detailed analysis and discussions are presented for different systems.

4.1 Kambersky Damping Model

The static Hamiltonian H_0 consists of the spin-independent paramagnetic Hamiltonian H_{para} taken in the tight-binding approximation, the Hartree-Fock approximation of the ferromagnetic exchange Hamiltonian H_{HF}, and the spin-orbit interaction (SOI) Hso. The Hamiltonian H0 can be written as

$$H_0 = H_{para} + H_{HF} + H_{SO};$$

$$= \sum_{\sigma,\mu_1,\mu_2 \in \{3d,4s,4p\}} \epsilon_{\mu_1,\mu_2,\sigma}(\vec{k})c^{\dagger}_{\mu_1,\sigma}(\vec{k})c_{\mu_1,\sigma}(\vec{k}) + \sum_{\sigma,\mu \in \{3d\}} J < n_{\mu}, -\sigma > \hat{n}_{\mu,\sigma}(\vec{k})$$

$$+ \ \xi \sum_{\sigma_1, \sigma_2, \mu_1, \mu_2} < \sigma_1, \mu_1 | \vec{L} \cdot \vec{S} | \sigma_2, \mu_2 > c^{\dagger}_{\mu_1, \sigma_1}(\vec{k}) c_{\mu_1, \sigma_2}(\vec{k}). \tag{4.1}$$

The Slater-Koster TB parameters ϵ of Fe and Co in the body-centered-cubic(bcc) and face-centered-cubic (fcc) structure are taken from the first principles calculations of Moruzzi et al[78]. As the band structures of fcc Pd and Pt are similar to fcc Fe and Co, the TB parameters of these two elements and the interaction between the 3d and non-3d transition elements are treated by scaling with the d-band width. The Hamiltonian is solved self-consistently using exchange interaction parameters that produce the experimentally observed spin moment: an exchange integral J, an on-site direct Coulomb integral U between d orbitals of the same symmetry , and an integral U' between d orbitals of different symmetry. The ratios between these exchange parameters are based on atomic symmetry[79] and Herring's work[80]. The exchange integral values of Fe and Co are taken from fcc bulk Fe and Co. The values of Pd and Pt are adjusted to produce the separate spin moments of Pd and Pt referred to another computational method[81] and also to preserve paramagnetism and the correct orbital occupancies in the fcc bulk materials. By analogy with Kambersky's derivation of damping for spin along $< 100 >$, we consider a damping tensor under arbitrary spin orientations

$$\alpha_{ij} = \frac{2\mu_B^2 g^2}{\gamma M \hbar} \sum_{n,m} \int \frac{d^3 k}{(2\pi)^3} \Gamma^{ij}_{nm}(k) W_{nm}(k), \tag{4.2}$$

$$\Gamma^{ij}_{nm}(k) = \langle n, k | [\sigma_i, H_{SO}] | m, k \rangle \, \langle m, k | [\sigma_j, H_{SO}] | n, k \rangle \,. \tag{4.3}$$

Here, i and j represent x, y, and z. H_{SO} and $\sigma_{i,j}$ are both expanded in spin and orbit space through the Kronecker product of two distinct atoms. The SOI strength is calculated to fit the experimentally observed orbital moments of both elements. The matrix elements $\Gamma_{nm}^{ij}(k)$ measure transitions between states in bands n and m induced by the spin-orbit torque. When n=m, this intraband damping, i.e., relaxation from the non-equilibrated population, has a conductivity-like behavior. The opposite resistivity-like behavior corresponds to interband damping when n$\neq$m: it is caused by the SOI induced electron-hole relaxation combined with a magnon annihilation. These scattering events are weighted by the spectral overlap of the phonons $W_{nm}(k) = \frac{1}{pi} \int dE \eta(E) A_{nk}(E) A_{mk}(E)$. The electron spectral functions A_{nk} are Lorenztians, with centers at the band energy E_{nk} and width $\hbar/\tau$, which represents the electron-phonon scattering frequency. The $\eta(E)$ function is the negative derivative of the Fermi function and peaks at the Fermi energy. γ is the gyromagnetic ratio and M is the saturation magnetization magnitude. The Hamiltonian is solved self-consistently to produce the experimentally observed spin and orbital moment. Details of the computational method are published elsewhere[64, 68].

The damping is mostly asymmetric in the transverse directions. This tensor can only be reduced to a scalar when the spin is in highly symmetric directions, for example, [001]-a fourfold or [111]-a threefold symmetric axis in bcc Fe. For

example, a rotation angle of $\pi/2$ about z exchanges x and y:

$$< n, \vec{\boldsymbol{k}}_1|\Gamma_x|m, \vec{\boldsymbol{k}}_1 > \quad = \quad < n, \vec{\boldsymbol{k}}_2|\Gamma_y|m, \vec{\boldsymbol{k}}_2 >;$$

$$< n, \vec{\boldsymbol{k}}_1|\Gamma_y|m, \vec{\boldsymbol{k}}_1 > \quad = \quad < n, \vec{\boldsymbol{k}}_2|\Gamma_x|m, \vec{\boldsymbol{k}}_2 > . \tag{4.4}$$

Thus, $\alpha_{xx} = \alpha_{yy}$ following integration over the full Brillouin zone. It implies that the scalar α at spin orientation of $[001]$ can be modified to be:

$$\begin{aligned}
\alpha \quad &= \quad \frac{1}{2}(\alpha_{xx} + \alpha_{yy}); \\
&= \quad \frac{\mu_B^2 g^2}{\gamma M \hbar} \sum_{n,m} \int \frac{d^3k}{(2\pi)^3} \{\Gamma_{nm}^{xx}(k) + \Gamma_{nm}^{yy}(k) + \frac{1}{2}\imath\Gamma_{nm}^{xy}(k) - \frac{1}{2}\imath\Gamma_{nm}^{yx}(k)\}W_{nm}(k); \\
&= \quad \frac{\mu_B^2 g^2}{\gamma M \hbar} \sum_{n,m} \int \frac{d^3k}{(2\pi)^3} W_{nm}(k)|\Gamma_{nm}^{-}(k)|^2. \tag{4.5}
\end{aligned}$$

where

$$|\Gamma_{nm}^{-}(k)|^2 = \{< n, k|[\sigma^-, H_{SO}]|m, k >< m, k|[\sigma^+, H_{SO}]|n, k >\}. \tag{4.6}$$

Thus, the result of Kambersky is recovered at spin orientation of $[001]$. When treating the experimental defects in the $L1_0$ alloys, We introduce one to four substitutional defects through exchanging the positions of 3d and non-3d transition elements in 36 atom supercells, to meet the degree of chemical order found in experimentally disordered structures. The substitution is created randomly 20 times, and an average is taken to obtain the damping for the respective degree of order.The degree of order is calculated from the atomic scattering factor with

the wave length and scattering angle found in the X-ray experiment[82]. The L10-type ordered structure is represented by 1, and 0 is the completely disordered structure.

4.2   bcc Fe

Gilmore[65] computed the Kambersky damping[64] for Fe, Co, and Ni and the results quantitatively agree with existing FMR measurements. Following their technique, we examine the dependence of damping on various material properties such as Fermi energy EF and spin orbit interaction strength in the highly symmetric direction [100]. Steiauf and Fahnle[83] have suggested a new approach to predict damping dependence on spin orientation and demonstrated a substantial variation for α in the bulk materials and reduced dimension systems. Their computation was limited to intraband damping, which make their conclusions only valid at low lattice scattering frequency $1/\tau$ ($\sim 1e^{13}s^{-1}$), i.e., temperatures below room temperature, where interband damping can be neglected.

We implement Kambersky's torque-correlation model, within the tight binding method, on bcc Fe. We first describe the damping tensor calculation method based on Kambersky's model. Numerical results for damping dependence (both interband and intraband) on material properties and spin orientation are shown.

Fig. 4.1(a) shows our predictions for damping as a function of wavevector sampling. It shows that $(64)^3$ wavevectors provide sufficient convergence near room temperature where $\hbar/\tau = 0.0265$ eV corresponds to experimentally measured conductivities of several MS/m. It can also be seen that low temperature prediction would require additional wavevectors owing to the enhanced sharpness of the spectral functions. Fig. 4.1(b) shows the predicted damping dependence on spin-orbit interaction strength ξ. The results imply that high anisotropy materials, which typically have large spin orbit interactions, will also typically have high damping. It can be seen that the intraband damping shows a cubic dependence on ξ, while the interband damping has a quadratic dependence on ξ. Although, the spin-orbit interaction for the p-orbitals is stronger than for the d-electrons, we find that the p electrons make little contribution to the damping. The damping from p orbitals with SOI strength of 180 meV is less than 1% of that from d orbitals with interaction strength of 50 meV. The reason is that the relaxation sources for both intraband and interband damping are electron-hole pairs around the Fermi energy and these are generally d electrons.

In contrast to first principle theories that typically underestimate orbital polarization, we set our spin orbit interaction to generate orbital polarizations matching the experimentally measured value of 0.11. This may account for our enhanced damping relative to Gilmore and Stiles for Fe oriented along the [001] axis. Fig.
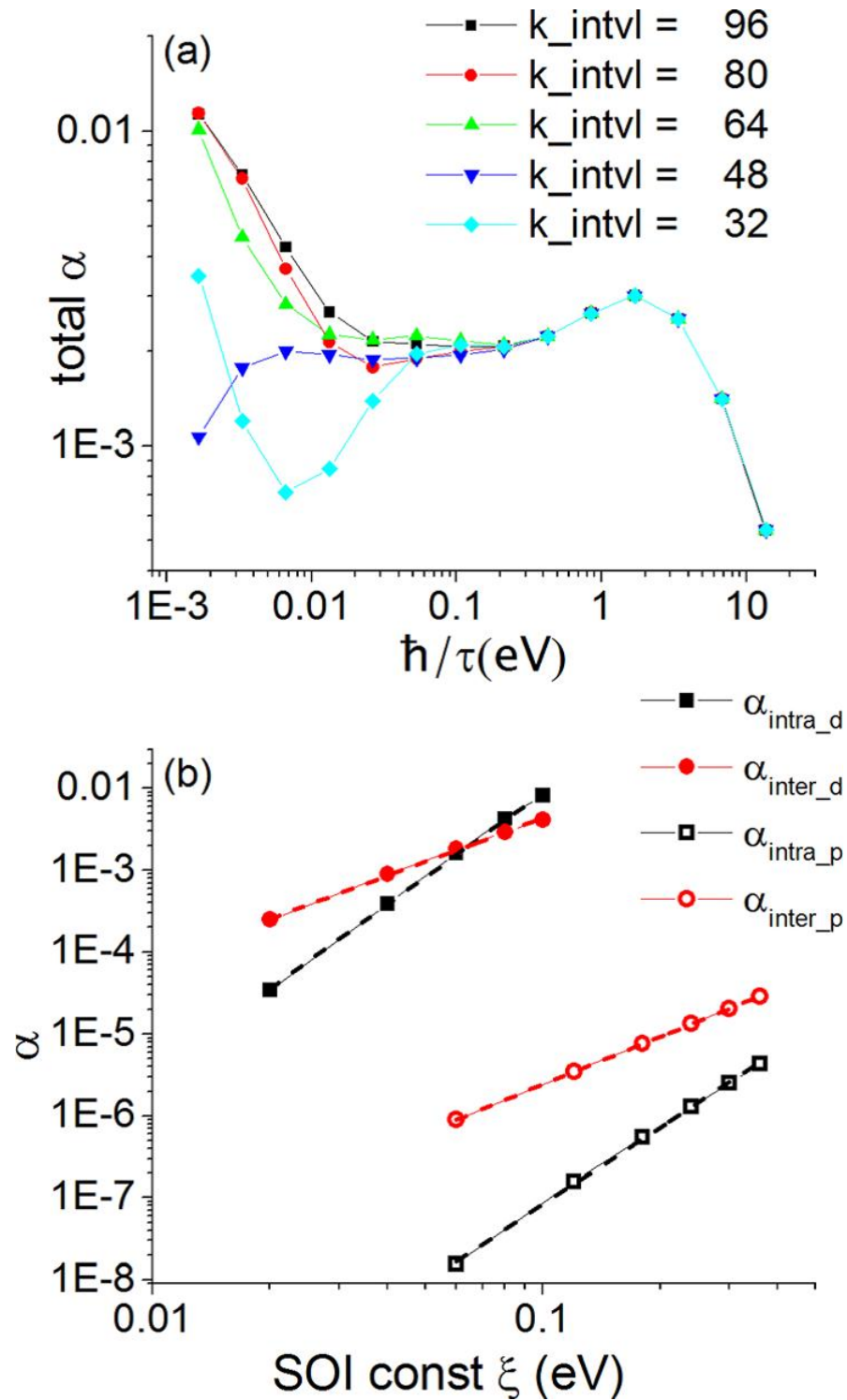
Figure 4.1: (a) Convergence of the damping parameter with wave-vector, (b) intraband and interband damping versus SOI constant ξ of d orbitals and p orbitals at the lattice scattering frequency $\hbar/\tau = 0.0265$ eV.

4.2(a) reveals our room temperature prediction to be 0.002 versus their prediction of 0.0013. The variation of α when we artificially shift the Fermi energy is larger than 100 times. The dependence of both intraband and interband α on E_F is generally proportional to the exponential of the density of states (DOS) at the Fermi level as shown in Fig. 4.2(b), similar to Sakuma's result[84], because the damping is mainly from the integral over the electron states around Fermi energy. The peak of damping is located in the same energy as the peak of DOS. Movement of the Fermi level can be accomplished by doping with elements such as Mn or Co. This relation also suggests that intrinsic damping in low dimension systems may be quite different from the bulk value because the DOS at the E_F differs for the distorted band structure of low dimensional systems.

At $\hbar/\tau$ =0.0265 eV, i.e., room temperature, the intraband and interband damping are comparable; thus, the breathing Fermi surface model[83] is not accurate under these conditions. Both affect the total damping dependence on spin orientation, shown in Fig. 4.3. The larger damping constant α_2 shows a variation of 54% and the smaller damping constant α_1 shows a variation of 35%. The damping is most anisotropic (the ratio of two damping eigenvalues $\alpha_1/\alpha_2 \sim 1.57$) when he magnetization is pointing along the hard axis $< 110 >$. Both intraband and interband show obvious anisotropic behavior for spin along the $< 110 >$ axis. The interband damping is less sensitive to the spin angle than the intraband damping.
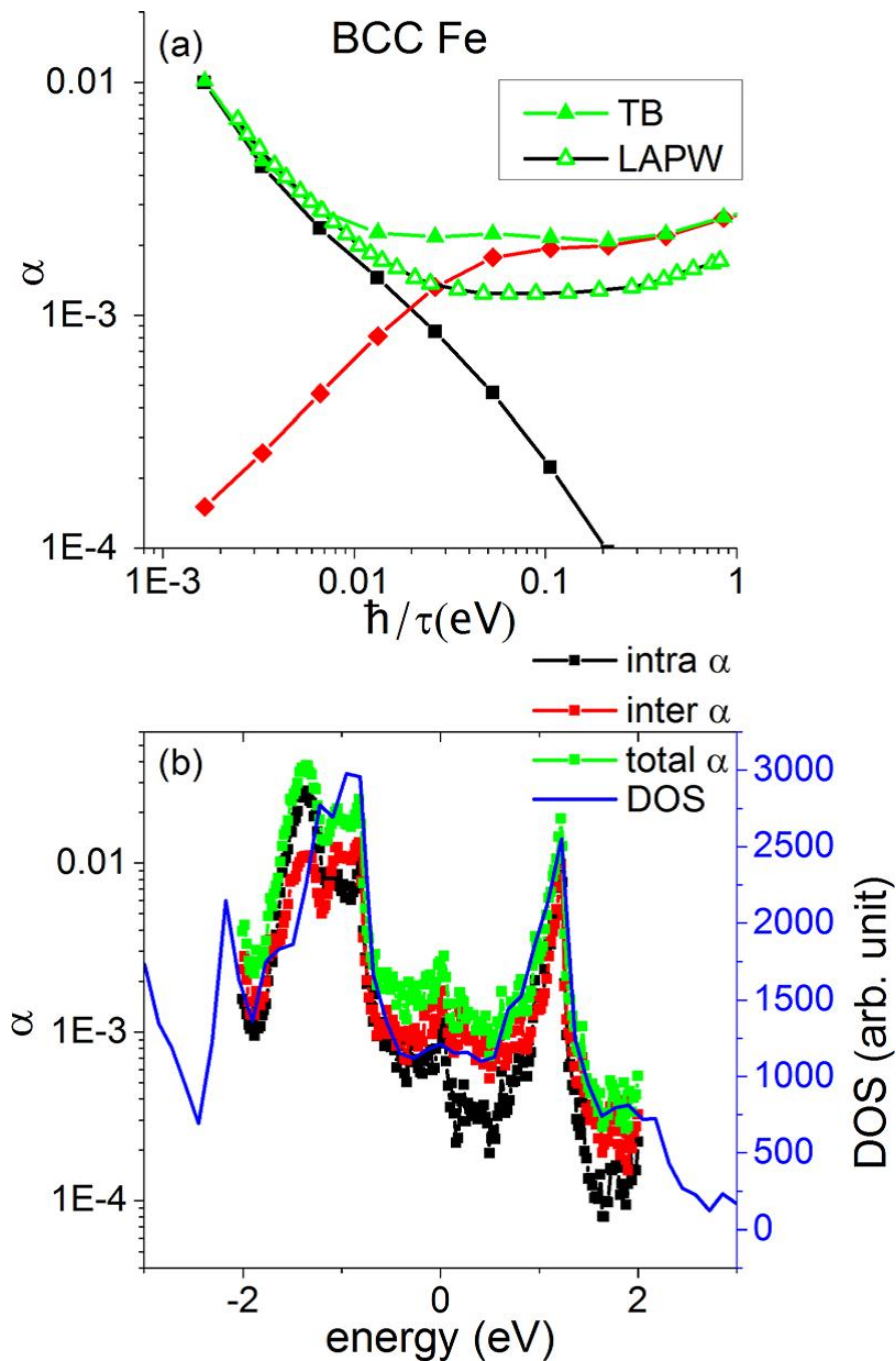
Figure 4.2: (a) Damping vs $\hbar/\tau$ in solid triangle and comparison with Gilmore and Stiles's LAPW method in open triangle. Solid squares represent the intraband damping. Solid diamonds represent the interband damping. (b) α dependence on Fermi energy and DOS vs energy. The Fermi energy is set to 0 for bulk Fe.

The ratio of the maximum to minimum intraband damping eigenvalues is 2.20 (α_1) and 2.73 (α_2), while for interband the ratios are only 1.29 (α_1) and 1.23 (α_2). This may be explained by the integration over more scattering events when two different bands are involved (interband) than within a single band (intraband). It is also noted that the intraband damping dependence on spin orientation tends to oppose that of the interband damping. Thus, the total damping response to spin orientation is the compromise of the two damping mechanisms.

4.3 $L1_0$ Ordered And Disordered Alloys

In both advanced spintronic and magnetic recording applications, high magnetic anisotropy materials play a key role because they are stable against thermal fluctuations, even at the nano-scale[85]. The $L1_0$-ordered alloys, such as FePt, CoPt, FePd, and CoPd, exhibit a very large uniaxial magnetic anisotropy energy above $1 \times 10^7 erg/cm^3$ and a moderate saturation magnetization Ms=1140 emu/cm^3 (for FePt and FePd) or 800 emu/cm^3 (for CoPt and CoPd) in bulk[86, 81]. The Kambersky mechanism is especially prominent in the listed $L1_0$ ordered alloys as high crystalline anisotropy implies strong SOI. Also, Pt has obviously larger SOI strength ξ of 0.5 eV (Ref. [87]) than the 3d transition metals such as Fe and
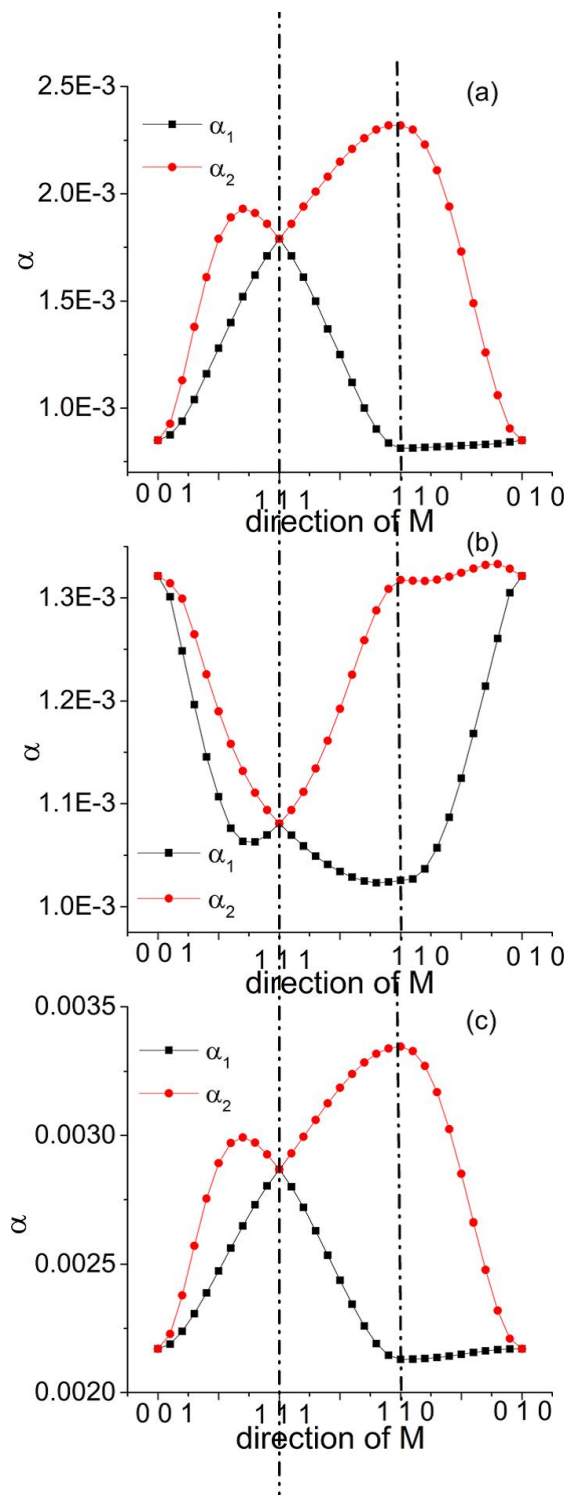
Figure 4.3: The intraband (a), interband (b) and total damping (c) eigenvalues for different orientations of spin at $\hbar/\tau$ =0.0265 eV.

Co. Studies show that high perpendicular anisotropy magnets including Pt possess large α, like Co/Pt multilayers[69, 88], ultrathin CoFeB/Pt (Ref. [89]), and Pt/Co films[90]. However, the reported experimental damping values in $L1_0$ alloys differ among investigators[91, 92, 93, 94]. Besides, the spin-flip scattering due to the random arrangement of atoms is infrequently investigated although the magnetic materials fabricated are mostly disordered systems. Sakuma's calculation[84] of α in $L1_0$ FePt assumes cubic symmetry, which may account for the apparent discrepancy with experiment.

We apply Kamberskys torque correlation model, within the tight binding (TB) method, to $L1_0$ ordered and disordered alloys FePt, FePd, CoPt, and CoPd. Damping values and magnetic properties of these alloys versus temperature, room temperature (RT) included, are calculated and compared with experimental data. Numerical results for damping dependence on material properties such as Fermi level E_F and ξ of 3d and non-3d transition elements are shown. The damping vs degree of chemical order in disordered structures is explored and analyzed. The degree of order is calculated from the atomic scattering factor with the wave length and scattering angle set in the X-ray experiment[82]. The L10-type ordered structure is represented by 1, and 0 is the completely disordered structure.

Fig. 4.4 shows our predictions for the intrinsic damping of four $L1_0$ ordered

high anisotropy materials-FePd, FePt, CoPd, and CoPt. The wave vector $\vec{k}$ sampling convergence of the damping computation is verified and $\vec{k}$ sampling including 64^3 points is chosen to produce the required accuracy (relative error less than 2%) in the full Brillouin zone. The intraband damping α_{intra} in these four materials decreases linearly versus $1/\tau$, while the interband damping α_{inter} shows the opposite behavior in the range of $\hbar/\tau$ below 0.42 eV. These opposite behaviors yield a minima around $\hbar/\tau=0.1$eV, where the scattering rate($\sim 10^{14}s^{-1}$) corresponds to experimentally measured conductivities of several MS/m at room temperature. We list the damping values and compare the calculated magnetic moments and the experimental data in Table 4.1. The total and orbital moment calculated is in good quantitative agreement with experiment [81, 95]. The damping value of FePt 0.02 also agrees with the measurement by Iihama and Ando et al[96].The distinctly larger damping of Pt-based to Pd-based alloys is caused by the stronger SOI strength in Pt (0.5 eV) than Pd (0.15 eV). We verified the damping computation is robust to the TB orbit parameters. The damping changes less than 20% when the s and p parameters are shifted rigidly between -1.36 eV and 1.36 eV.

Although the spin-orbit interactions from both constituent atoms contribute to the damping of the alloys collectively, the damping is more sensitive to the 3d transition elements (Fe/Co), caused by the noticeable difference in the orbital
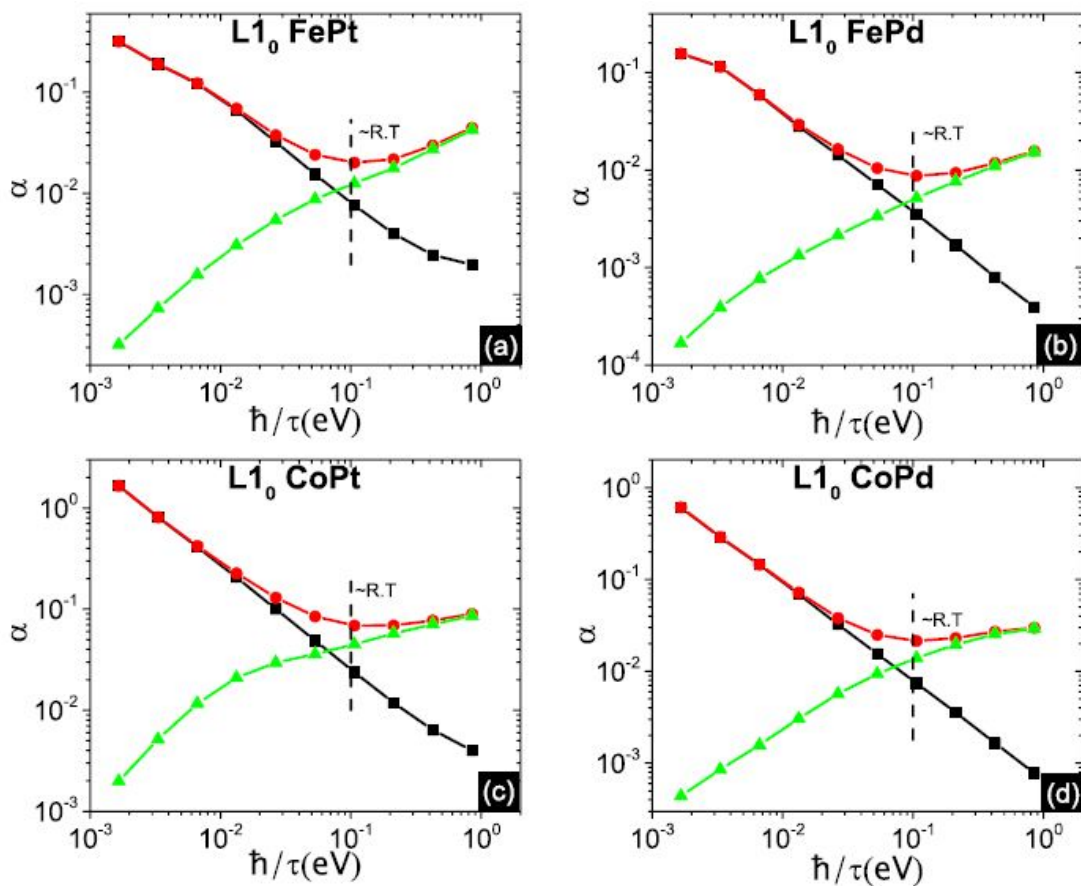
Figure 4.4: Damping α versus $\hbar/\tau$ in the ordered alloys ((a) FePt, (b) FePd, (c) CoPt, (d) CoPd) in the $L1_0$ phase. The solid circles, squares, and triangles correspond to the α_{total}, α_{intra} and α_{inter} separately.

	$S_{Fe/Co}$	$S_{Pd/Pt}$	$L_{Fe/Co}$	$L_{Pd/Pt}$	M_t	M_{exp}	α_{RT}
FePt	2.663	0.454	0.18	0.06	3.358	3.4	0.02
FePd	2.668	0.426	0.196	0.023	3.313	3.3	0.009
CoPt	1.668	0.424	0.161	0.091	2.344	2.4	0.069
CoPd	1.626	0.457	0.178	0.036	2.297	2.3	0.021

Table 4.1: Calculated and measured magnetic moment and damping values at RT of the four ordered alloys. Values in the first four columns indicate calculated spin and orbital moment for 3d and 5d elements constituting the alloys. The fifth and sixth columns are the total magnetic moment and experimental data. All the columns of the magnetic moment are in the unit of Bohr magneton μ_B. The last column shows the calculated damping values at RT.

moment. The large L_{3d} implies strong effective coupling to the spin moment, while the coupling in non-3d atoms is reduced by the abundant and symmetric spin polarization states around the Fermi level that introduce less contribution to damping. To quantitatively describe the damping sensitivity difference to the element types, we analyze the $\alpha_{intra/inter}$ dependence on $\xi_{3d/non3d}$, setting the SOI strength of the other element as zero. We describe the dependence using an equation $\alpha_{intra/inter} = \Lambda\xi^x$, while Λ characterizes the damping sensitivity to SOI strength and x is the exponent. All the α_{intra} show a cubic dependence and all the α_{inter} show a quadratic dependence on $\xi_{3d/non3d}$, as shown in Figs. 4.5(a) and 4.5(b). These scalings are similar to a previously calculated bcc-Fe case[66, 68] and $L1_0$ FePdPt case[91]. A small deviation in the exponent, e.g., $\alpha_{inter} \sim \xi_{Co}^{1.96}$ in CoPd, is caused by the complex mixed electronic states of 3d and non-3d elements. For both intraband and interband mechanisms, Λ_{non3d} are all smaller than those of

3d elements. As the total damping at RT is mainly determined by the interband

mechanism, Λ_{Fe} is 0.211 and Λ_{Pd} is 0.047 in FePd. This implies that the SOI of

the non-3d element will dominate the damping when ξ_{non3d} is over 0.29 eV, under

the quadratic estimation. Based on the estimation of the main damping source,

the conclusion that spin-orbit interaction from Pd has a minor effect on damping,

while the interaction from Pt is significant to damping, is verified in Fig. 4.5(c).

There is also strong correlation between density of states (DOS) at the Fermi

level and the damping. This suggests one approach to tune the damping is through

adding impurity atoms. Artificially shifting Ef shows that α_{total}, α_{intra} and α_{inter}

follow the shape of the DOS at E_F, in Fig. 4.5(d). Although the exponential

dependence, found in bcc-Fe (Ref. [68]) does not describe the relation in these

ordered alloys, the numerous spin states around the Fermi energy in Co-based al-

loys lead to a larger damping than Fe-based alloys. Under a linear approximation,

the ratio of DOS in CoPd to that in FePd at the original Fermi energy is 1.9, and

the ratio of the CoPd damping to FePd damping is 2.3.

When substitutional defects are introduced in the supercells, the damping at

RT increases when the degree of order of the four alloys decreases, as shown in

Fig. 4.6. The computational accuracy of the 36-atom supercell is confirmed by

showing that the calculation with no defects yields the same total, intraband, and
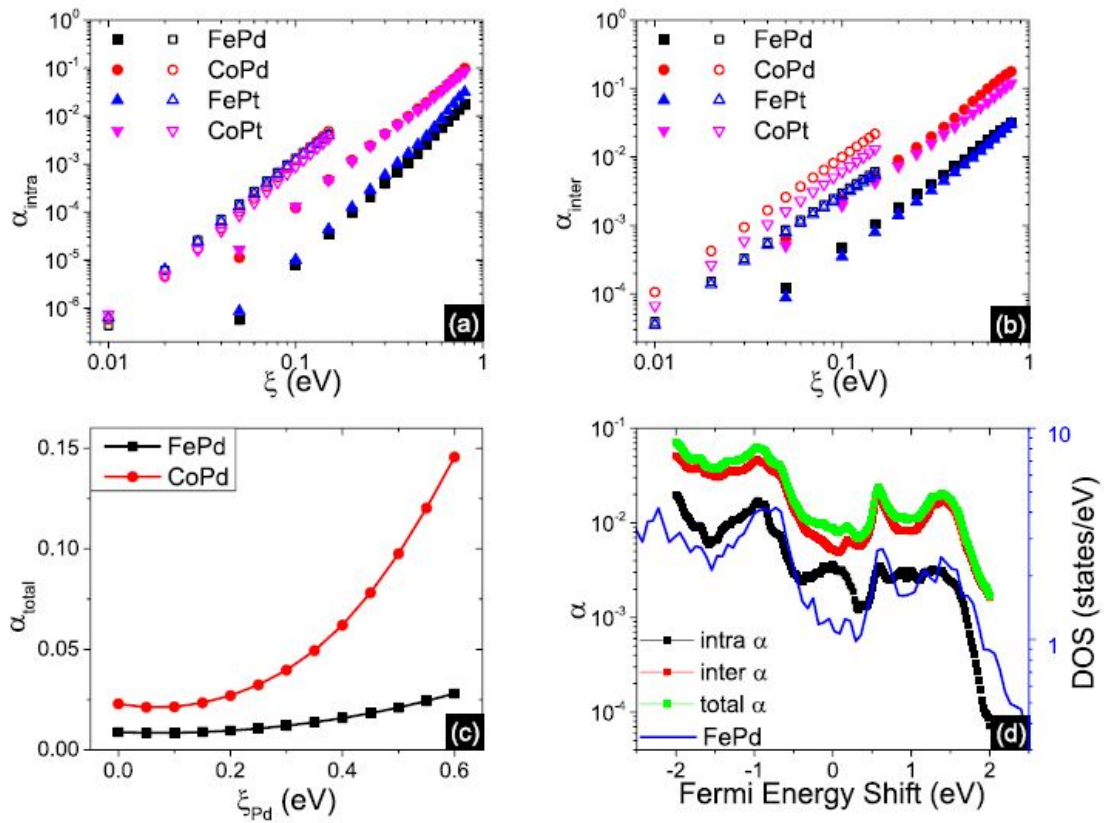
Figure 4.5: (a) The intraband damping and (b) the interband damping vs ξ when SOI strength of the other constituent element in the four alloys is set as 0 eV. The solid points are computed varying non3d SOI and the hollow points are varying ξ_{3d}. (c) The total damping vs ξ_{Pd} computed for FePd and CoPd band structures when $\xi_{Fe/Co}$ retain their original value. The curve is flat in the ξ_{Pd} range of 0.0 to 0.20 eV and rapidly increases after 0.20 eV. (d) The damping α_{total}, α_{intra} and α_{inter} and DOS versus Fermi level in the alloy FePd. The left axis is the damping, and the right axis is the DOS. The damping values in all figures here are computed at RT.

interband damping values as the previous results for the single cell. The damping value of FePd at chemical degree of order S=0.31 is 0.013. This value matches a ferromagnetic resonance measurement done on the partially ordered FePd thin film with the same degree of order[97], although the accuracy of the experimental results may be affected by the anisotropy. An analysis of the electron states shows that there are dense spin scattering channels in the energy range of -0.1 eV to 0.1 eV, which dominates the contribution to damping at RT. In the DOS spectra, as shown in Fig. 4.7, the ordered phase has large fluctuations with steep peaks. The formation of ordered alloys allows the E_F to sit in the bottom of the valleys. By contrast, the DOS of disordered alloys is smeared into a smoother shape and the E_F can be located randomly because of the broken symmetry. The DOS difference produces more spin scattering channels around E_F in the disordered phase and also explains that the damping is more sensitive to degree of order in Fe-based alloys. As the Co-based alloys already have many states at E_F in the ordered phase, the spin channel increase is not as distinct as the increase in Fe-based alloys. The ratio of damping of the disordered structure (degree of order is 0.31) to the ordered structure in Fe-based alloys is more than 1.44 and the ratio is less than 1.17 in Co-based alloys.

We also observe that the two mechanisms in Kambersky damping: intraband
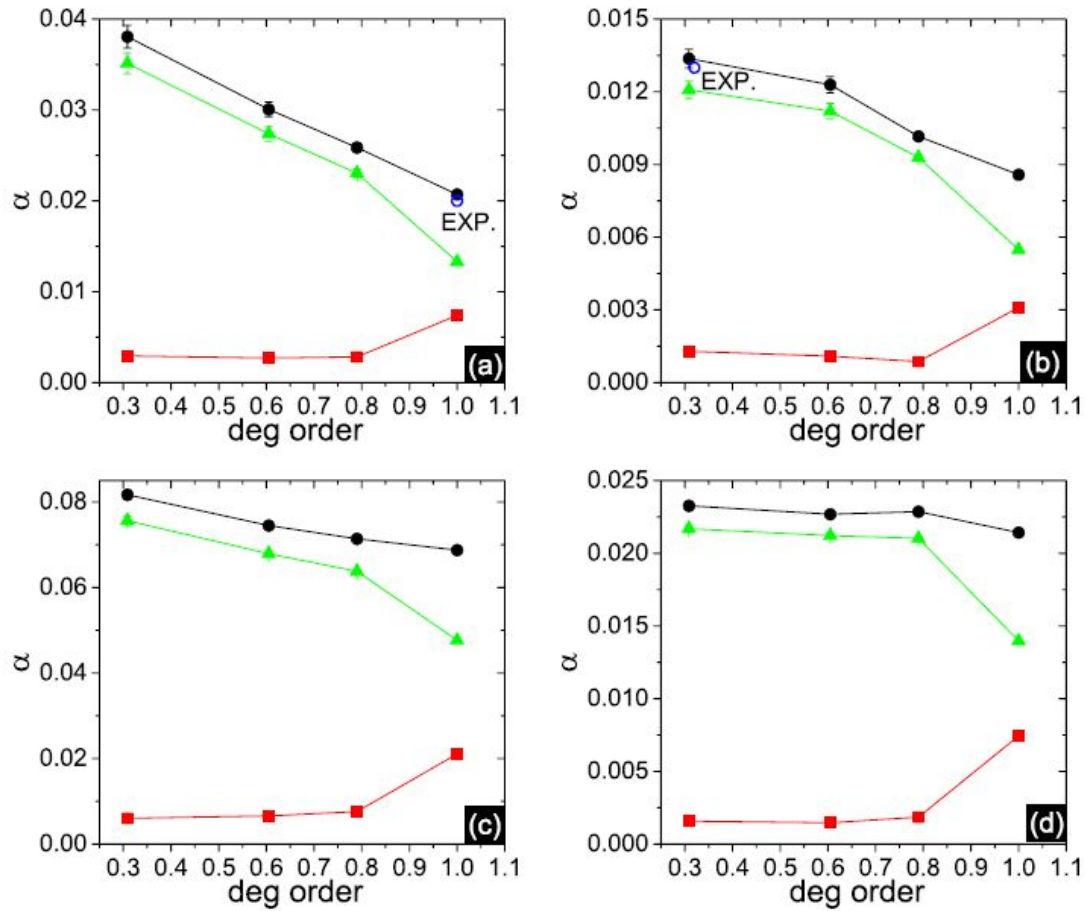
Figure 4.6: Total (solid circle), intraband (solid square), and interband (solid triangle) damping at room temperature vs chemical degree of order in disordered (a) FePt, (b) FePd, (c) CoPt, and (d) CoPd with varying number of substitutional defects.

and interband scattering behave oppositely versus the degree of order. The interband damping monotonically increases when more defects are included. As the scattering happens in different states, the scattering events increase roughly as the spin channel number squared. This brings progressively more contribution to the damping. However, the effect of spin channel on the intraband mechanism is not important, as the scattering only happens in the same electron state. To analyze the fast decrease of the intraband damping from ordered to disordered phase, we consider the torque operator $\Gamma^- = L^{-1}\sigma^Z - L^Z\sigma^-$ that partly determines damping rates. The torque operator consists of spin flip and orbital excitation. In the intraband mechanism, the spin flip term is neglected as the majority electron states can be treated as pure spin states perturbed by spin-orbit interaction. The torque matrix elements are dominated by the orbital excitation term. In Fig. 4.8, there are long tails representing large values of Γ^- in the ordered phase. This differs from the three disordered structures. Also, these k points in the tail have large weight in the damping as their energies mostly are very near to the E_F (less than 0.014 eV).
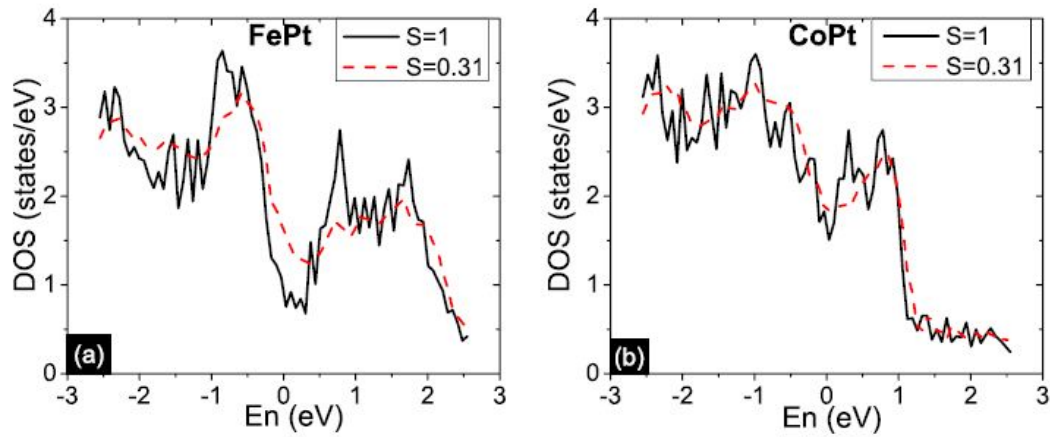
Figure 4.7: DOS spectra of (a) FePt and (b) CoPt at degree of chemical order S of 1 and 0.31 with varying numbers of substitutional defects.
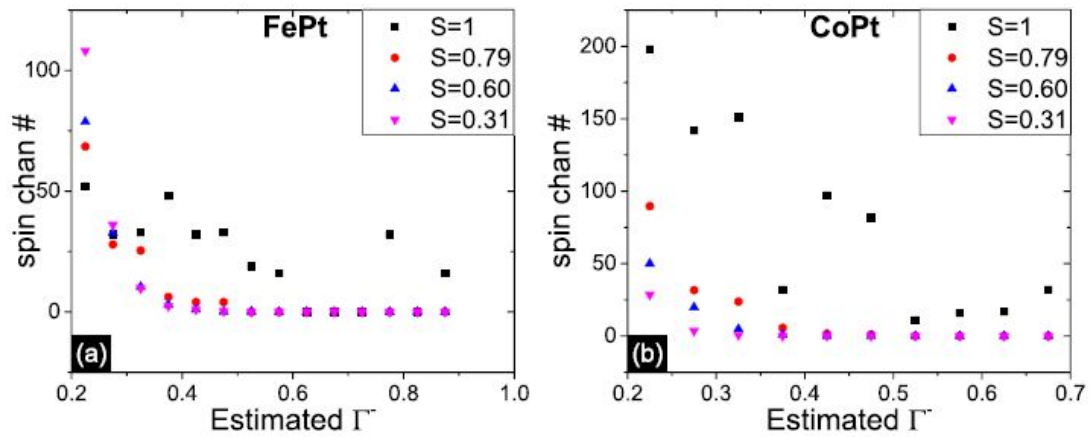
Figure 4.8: Spin channels distribution statistics of estimated torque operator Γ^- values of (a) FePt and (b) CoPt in structures with varying numbers of substitutional defects.

4.4 Superlattices with Perpendicular Magnetocrystalline Anisotropy

Artificially layered magnetic metal structures, such as superlattices, are a topic of intense current interest because of their unusual surface properties and potential application in spintronic devices. These structures have demonstrated a variety of phenomena such as giant tunneling magnetoresistance[98, 99, 100], Ruderman-Kittel-Kasuya-Yosida (RKKY) coupling[101, 102] and most importantly, large perpendicular anisotropy(PMA). Transition-metal superlattices, such as Co/Pt[103, 104] and Co/Pd, deposited by molecular-beam epitaxy or sputtering are good candidates for PMA applications because they exhibit a very large PMA above 1×10^7 erg/cm^3 and a moderate magnetization Ms=800 emu/cm^3 in bulk, along multiple crystal axes. The large PMA guarantees the device stability over a large temperature range even at the nano-scale, in both high density magnetic recording and electrically manipulated spintronic devices. High PMA allows the extension of magnetic recording beyond the superparamagnetic limit and thus offers higher aerial densities. PMA materials substantially reduce the critical current for spin-torque switching relative to the usual in-plane magnetic anisotropy materials that are adversely affected by the demagnetization effect in a thin film structure. While the PMA is explored thoroughly both in experiment

and theory, the damping α has not been fully investigated for superlattices. Both the anisotropy energy and damping in transition-metal superlattices is electronic in origin and predominantly result from the spin-orbit interaction(SOI). Despite the tendency for in-plane anisotropy caused by demagnetization energies, many short period magnetic multilayers exhibit a perpendicular anisotropy, resulting from the influence of the interface. It has been found both experimentally and theoretically that the interfacial anisotropy is independent of the growth direction for Co/Pd superlattices[105, 106, 107], although the bulk contribution can vary according to magnetostrictive effects. However, the effect of the surface and the superlattice orientation on the damping is not clear yet. The investigation of the damping properties in various superlattices can give insight to the surface and growth orientation effect on damping, and enable optimization of superlattice structures exhibiting useful perpendicular anisotropy.

In section 4.3, enhanced damping is shown in $L1_0$ ordered/disordered FePt, CoPt alloys due to the obviously larger SOI strength ξ of Pt(~ 0.5eV) relative to the 3d transition metals such as Co and Fe. Materials containing Pd or tenary alloys substituting Pt with Pd always show reduced damping, which can partially be explained by the weaker SOI strength ξ of Pd(~ 0.15eV). However, the distorted electronic states at the interface of two materials might also cause a difference in damping, although this is rarely explored. Barati[69] calculates the interfacial

effect for superlattices, oriented along the (001) direction; the extracted interfacial damping is negligible or negative, suggesting that surface effect helps minimize the energy dissipation, which is not consistent with experimental measurement. His layer distributed damping shows non-physical negative values, usually associated with non-conservation of magnetic energy. Besides, his bulk damping of Co is larger than 0.01, differing from experimental FMR data[108].

We apply the Kambersky model, to superlattices of Co/Pd and Co/Pt growing in mutiple crystal orientations. We identify the orientation dependent interfacial and bulk contribution to the total damping. We also check the damping dependence on the spin-orbit interaction strength of the non-ferromagnetic metal and infer the origin of the interfacial damping. We expand the damping calculation from the initial spin out-of-plane direction to spins at arbitrary angle and obtain the damping dependence on the spin orientation.

In a superlattice, the broken symmetry at the interface can be the dominant contribution to the total damping. Fig. 4.9 shows our prediction for the intrinsic damping constant of superlattices with different Co layer thickness. The superlattice is oriented along the [001] axis and the spin orientation is perpendicular to the plane. The wave vector $\vec{k}$ sampling convergence of the damping computation is verified and $\vec{k}$ sampling including 32^3 points is chosen to produce the required accuracy (relative error less than 2%) in the full Brillouin zone. The

product of the damping and the layer number of Co is linearly dependent on the number of Co monolayers, in Fig. 4.9. $n\alpha = 2 * \alpha_{interface} + n\alpha_{bulk}$, where n is the number of Co layers, $\alpha_{interface}$ and α_{bulk} are the interfacial and bulk damping respectively. We are fixing the spin orientation to be perpendicular to plane even in the normally in-plane oriented thicker Co layers (this can be accomplished by an applied field), in order to extract the intrinsic interfacial damping. The interfacial damping extracted from the linear fitting for n Co/6 Pt and n Co/ 6 Pd is 0.18 and 0.019. The difference between the interfacial damping of two superlattices originates from the stronger SOI strength in Pt (0.5eV) than Pd (0.15eV). This interfacial source increases the amount of energy lost in the short-period superlattices significantly, compared to the bulk Co damping. The bulk damping is only determined by the Co intrinsic properties and not affected by the deposited non-magnetic monolayers. When the Co layer thickness is below around five monolayers, the damping shows an oscillatory behavior, and the damping increases abruptly at some Co layer thicknesses. This oscillation might be attibuted to quantum well (QW) states with energies at the Fermi level. The occurrence of QW states in metallic films also leads to oscillations of interlayer exchange coupling and magnetic anisotropy with varying thickness of ferromagnetic films or nonmagnetic layers [109, 110, 102, 111]. The oscillation periods associated with QW states are related to the extremal radii of Fermi-surface sheets

of Co films. The magnetic anisotropy (also caused by the spin-orbit interaction) of (001) fcc Co film oscillates with a period around 2 monolayers, confirmed in earlier theorectical prediction [112] and recent experiment [110]. The anisotropy oscillation is dominant at the center of the 2D Brillouin zone where pairs of QW states are degenerate at the Γ point. The oscillation periods for damping of (001) CoPd/CoPt are also around 2MLs, thus it might be the same QW states producing both the oscillation of anisotropy and damping. Edwards [113] has argued that the intraband damping should be absent based on the direct calculation of the dynamical transverse susceptibility. The intraband absence removes the infinite divergence of damping at zero temperature and has significant effect on damping at low temperature. This will change our results slightly, as our calculations are near room temperature and the intraband damping has a negligible contribution to the total damping, as shown in Fig. 4.9.

The interfacial damping varies when superlattices orient along different axes. The linearity of $n\alpha$ remains for all oriented superlattices, shown in Fig. 4.10. When the spin direction is perpendicular to the plane, the bulk contribution to damping α_{bulk} is substantially independent of orientation, as expected for bulk Co. In contrast, $\alpha_{interfacial}$ shows larger values in [111] and [011] directions than [001] direction, especially for the Co/Pd superlattices, shown in Table 4.2. The standard deviation of $\alpha_{interfacial}$ is 45% for Co/Pd, and $\sim$ 14% for Co/Pt. In
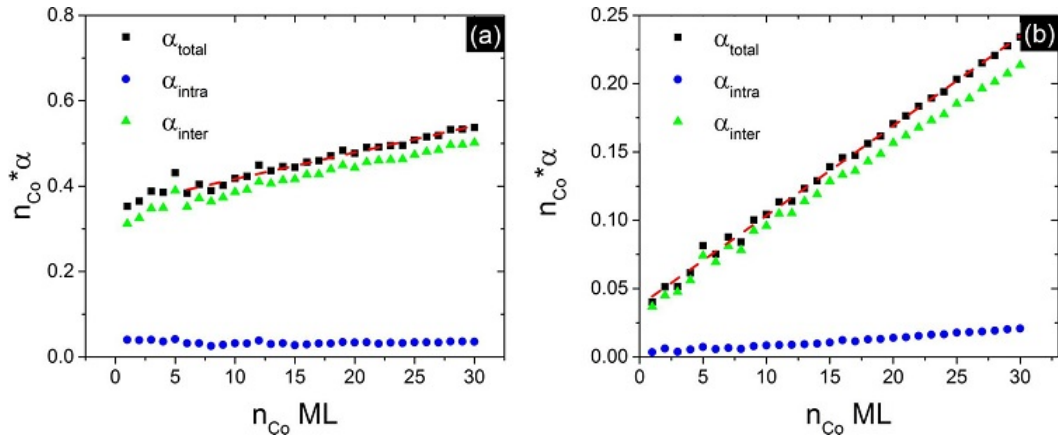
Figure 4.9: The product of the number of Co layers and the damping constant versus the number of Co layers in superlattices (a) n Co/6 Pt and (b) n Co/ 6 Pd. The red dashed line is the linear fitting to the total damping constant. The dots in different shapes refer to the total, intraband and interband damping respectively.

addition to the effect of the changing spin orientation, the interfacial damping is also affected by the altered atomic enviroment at the interface. The nearest and next nearest neighbours vary for superlattices oriented along distinct axes and modify the electronic states markedly, which results in a sensitive dependence of interfacial damping on the superlattice orientation. Furthermore, two sets of interfacial and bulk damping values are shown for spin in the [011] superlattice orientation, which reflects anisotropic ferromagnetic relaxation in the transverse in-plane directions. This anisotropic behavior is caused by the broken symmetry of the electronic states when spin is pointing in directions that are not highly symmetric. This tensor behavior can be reduced to a scalar when the spin is in highly symmetric directions, for example, [001]-a fourfold or [111]-a threefold

symmetric axis.

The interfacial damping dependence on superlattice orientation is explained by the varying electronic states at the interface. We separate each layers' contribution to the damping by manually zeroing the SOI strength of all but one layer in the damping computation. Fig 4.11 shows that non-zero spin-orbit interaction in single magnetic or non-magnetic layers can enhance the damping, compared to the damping value 0.0055 of bulk fcc Co, particularly for the (111) orientations. This damping difference between (111) and (001) orientations is presumably caused by the interfacial electronic state at the Co layer adjacent to Pd/Pt layer, as confirmed by the contour map of the weighted d state in the 2D k-space, in Fig 4.12. The weighted d state is calculated by summing over all d states at one specific k point, weighted by the band energy in the Lorentzian distribution centered at the

Table 4.2: The table shows the extracted interfacial and bulk damping for Co/Pt and Co/Pd superlattices oriented in [001],[111] and [011] axes. The superlattices are multiple Co layers deposited on six Pt or Pd layers. The spins are oriented perpendicularly to the planes.

x Co/ 6 Pt			x Co/ 6 Pd		
Orientation	$\alpha_{interface}$	α_{bulk}	Orientation	$\alpha_{interface}$	α_{bulk}
001	0.18	0.0062	001	0.019	0.0065
111	0.23	0.0069	111	0.049	0.0074
011	0.24	0.0067	011	0.024	0.0067
	0.25	0.0073		0.026	0.0077
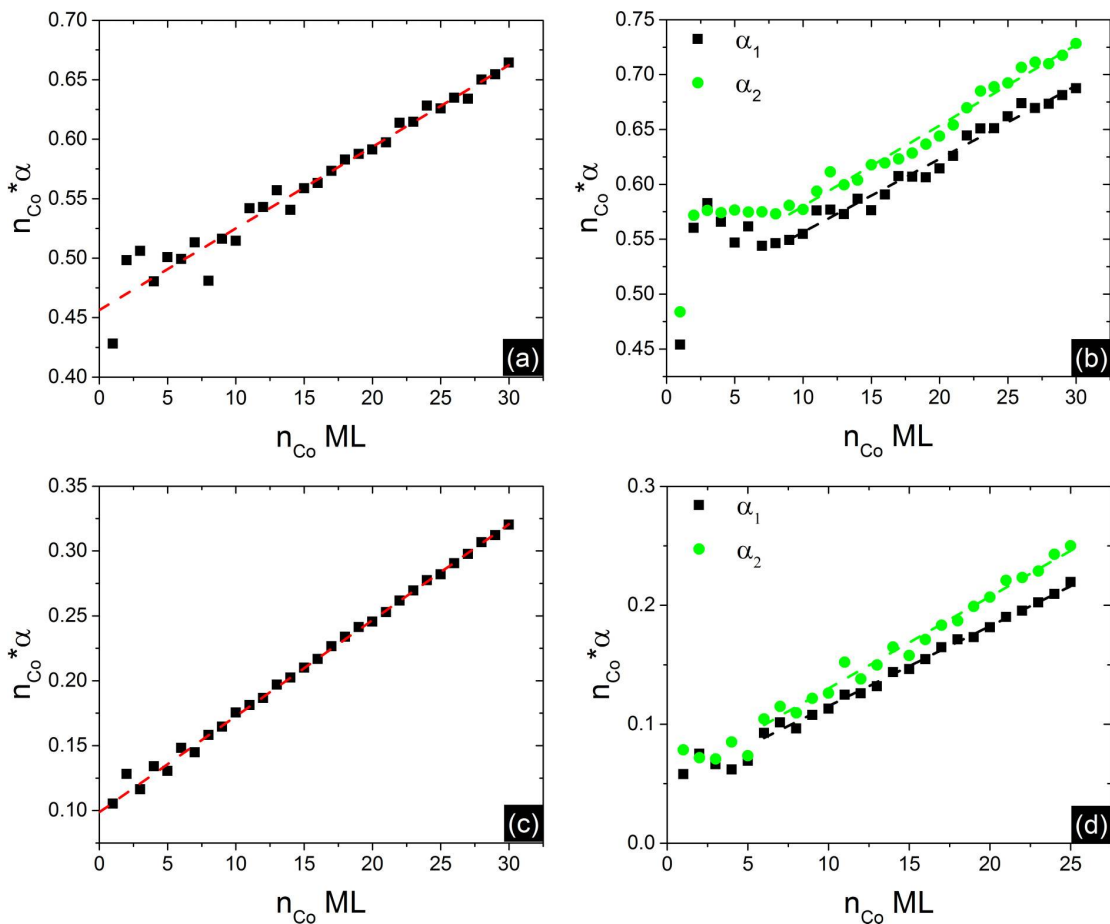
Figure 4.10: The product of the number of Co layers and the damping constant versus the number of Co layers in superlattices of varying orientations (a) Co/Pt[111], (b) Co/Pd [111], (c) Co/Pt[011] and (d) Co/Pd [011]. The dashed lines are the linear fittings to the total damping constant. The superlattices are multiple Co layers deposited on six Pt or Pd layers. The spins are oriented perpendicularly to the planes. α_1 and α_2 in (c), (d) are the eigenvalues of the damping tensor.

Fermi level, similar to the damping computation. In the (001) superlattice orientation, the dominant k points contributing to damping in interfacial Co atom lie along diagonal lines, and show a non-monotonic behavior: the k points around the Γ point have less impact on the damping while the k points with magnitude 20% or 80% of the in-plane k basis vectors have ten times larger impact on the damping. For the interfacial Pt atom, the k points surrounding the Γ point contribute mainly to the damping. In contrast, for (111) interfacial Co atoms, the k points determining the damping are more uniformly distributed in the whole Brillouin zone. The most influential k points for the interfacial Pt atom are far away from the Γ point, opposite to the (001) superlattice. This interfacial electronic state is a mixture of electrons from both magnetic and non-magnetic metals. In the (001) superlattice, for the Co atom at the interface, the nearest neighbours (NN) are four Pd/Pt atoms and eight Co atoms, the next nearest neighbours (NNN) are one Pd/Pt atom and five Co atoms. In contrast for the (111) superlattice, the NN are three Pd/Pt atoms and nine Co atoms, the NNN are three Pd/Pt atoms and three Co atoms. The assorted surrounding atomic environment has distinct impact on the interfacial Co atoms, thus generating superlattice orientation dependent damping. We only focus on the d orbital states, because these states give the spin polarization and possess strong spin-orbit coupling.

The density of states (DOS) at the Fermi level has a significant impact on the
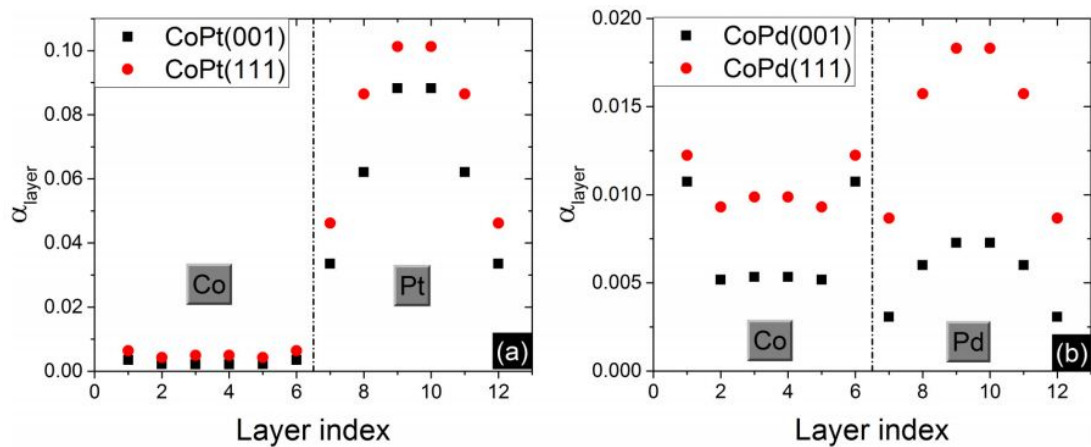
Figure 4.11: Layer contribution to the Gilbert damping constant in superlattices in both (001) and (111) orientations. The superlattices are six Co monolayers deposited on (a) six Pt or (b) six Pd layers

damping because the spin scattering primarily happens in the electronic states around the Fermi level. We artificially shift the Fermi energy and separate the layer contribution to the damping. Fig 4.13 shows that the peak of the layer damping contribution is located at the same energy as the peak of DOS of each layer. Double peaks appear in the Co layers: one below the Fermi level around -0.05Ry and one above the Fermi level around 0.07Ry. The DOS peak of the interfacial Co monolayer is nearer the Fermi level than the DOS peak of the Co layer away from the interface. In the Pt atoms, a sharp peak in the damping is found near the Fermi level. In contrast to the Co layers, the interfacial Pt DOS peak is lower energy than the bulk DOS. The shape of the total damping is more complicated due to the mixture of the DOS of multiple atoms. The sharp change
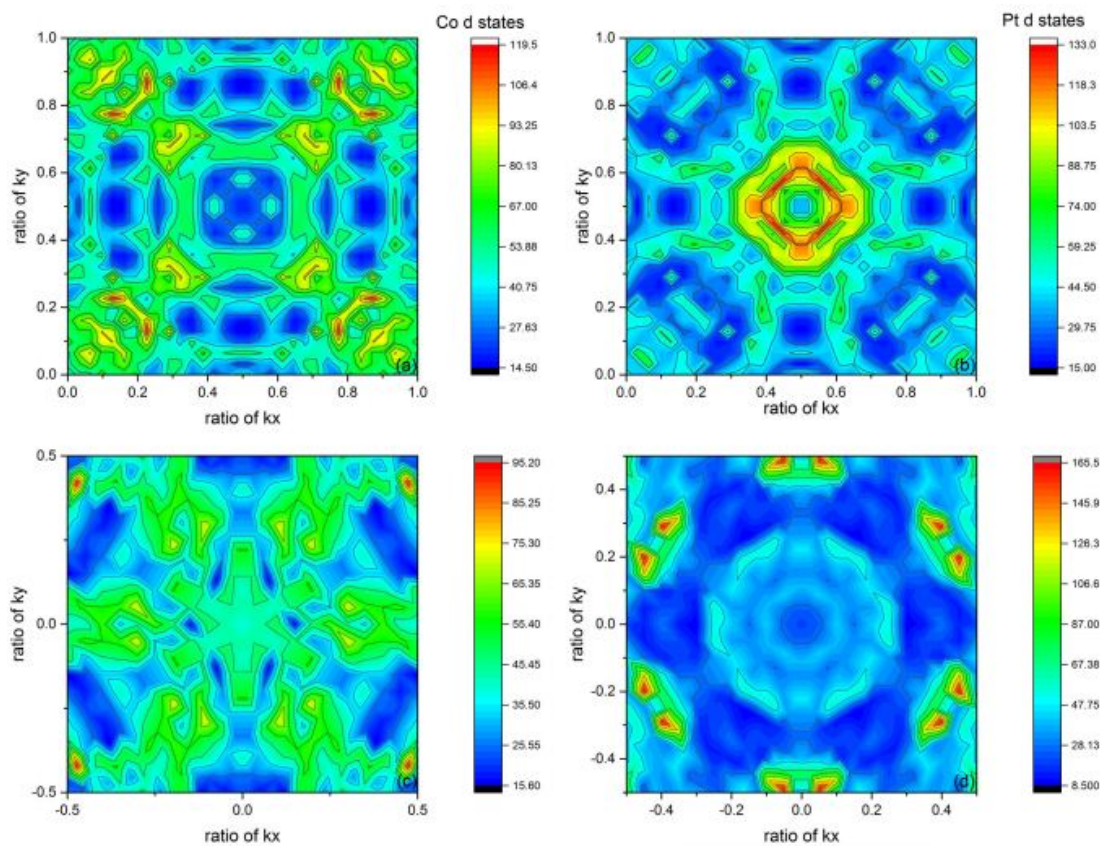
Figure 4.12: Weighted d electronic states distribution in the Brillouine zone for the interfacial atoms (a) Co (b) Pt in the superlattice 6 ML Co/ 6 ML Pt in (001) orientation and (c) Co (d) Pt in the superlattice 6 ML Co/ 6 ML Pt in (111) orientation.

in the damping around the original Fermi level remains. The total damping varies by a factor of 40 near the Fermi level. Experimentally, tuning the damping can be accomplished by adding an amorphous agent such as B, that the DOS can be smoothed.

The interfacial damping is closely correlated with SOI strength ξ because the source of the damping is the coupling between spin and lattice. It is shown that the interfacial damping increases monotonically with the SOI strength of Pd/Pt, as shown in Fig 4.14. The interfacial damping persists when spin-orbit interaction in Pd/Pt $\xi_{Pd/Pt}$ equals zero. This implies that the interfacial damping is caused by both the SOI in the non-magnetic elements (Pd/Pt) introduced by electronic state mixture and the broken symmetry of the electronic state of magnetic element Co at the interface. The [001] and [111] interfacial damping from broken symmetry is 0.01 while the [011] orientation has damping 0.02 in both Co/Pt and Co/Pd systems. Compared to the interfacial damping at the original SOI strength of non-3d transisition elements, the SOI from Pd ($\xi_{Pd} = 0.15eV$) has a minor effect on the interfacial damping, while the broken symmetry at the interface is the dominant source in Co/Pd system. For the SOI values beyond $\xi = 0.15eV$, the interfacial damping increases distinctly for stronger SOI in the non magnetic transition elements. This suggests that the damping can be tuned by depositing heavy metals (Ta, W etc.) for larger damping or light metals (Mn, Cu) for smaller

damping, to adjust the performance of spintronic devices. For Co/Pt system, the interaction from Pt ($\xi_{Pt} = 0.5eV$) significantly affects $\alpha_{interface}$, enhancing the $\alpha_{interface}$ more than ten times, compared with the unavoidable contribution from the interfacial broken symmetry. The minor discrepancy between $\alpha_{interfacial}$ dependence in Co/Pt and Co/Pd might be caused by the subtle difference of the similar band structures between the two seperate superlattice systems. The computation confirms that the bulk damping is not affected by the SOI in non-magnetic elements and is determined by the property of Co layers.

The total damping exhibits asymmetric behavior in the transverse directions for most spin orientations. A tensor is necessary to describe damping. Only in very highly symmetric directions, e.g. spin pointing along the perpendicular to plane axes in superlattices oriented in [001] and [111] directions, the tensor can be reduced to a scalar. Moreover, the tensor is dependent on the spin orientation. In both superlattices (Co/Pd, Co/Pt) oriented in [001], the damping tensor shows more marked difference between different spin directions than found for the other superlattices oriented in [011] and [111] directions, as shown in Fig. 4.15. The ratio of the maximum to minimum damping eigenvalues $\alpha_{max}/\alpha_{min}$ is 1.69 for Co/Pd and 1.21 for Co/Pt in the [001] orientation, while for the other two orientations, the maximum ratios are 1.03 ([111]) and 1.21 ([011]). Furthermore, the interfacial broken symmetry source is more sensitive to the spin orientation variation, rather
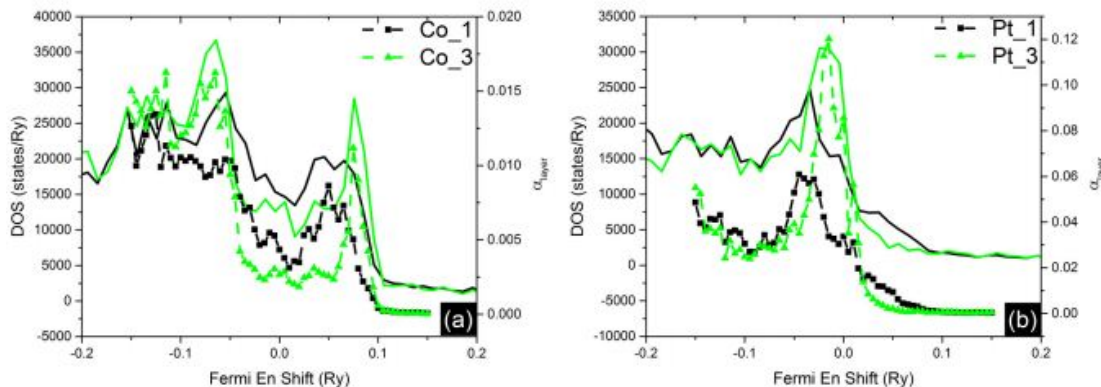
Figure 4.13: The damping layer contribution versus the shifted fermi level of (a) Co MLs (b) Pt MLs. The index of the atom is based on the distance from the interface. 1 represents the interfacial atoms. The superlattice is six MLs Co deposited on six MLs Pt in (001) orientation. The properties of the other Co and Pt atoms in the superlattice are not shown due to the symmetry in the periodic boundary conditions.
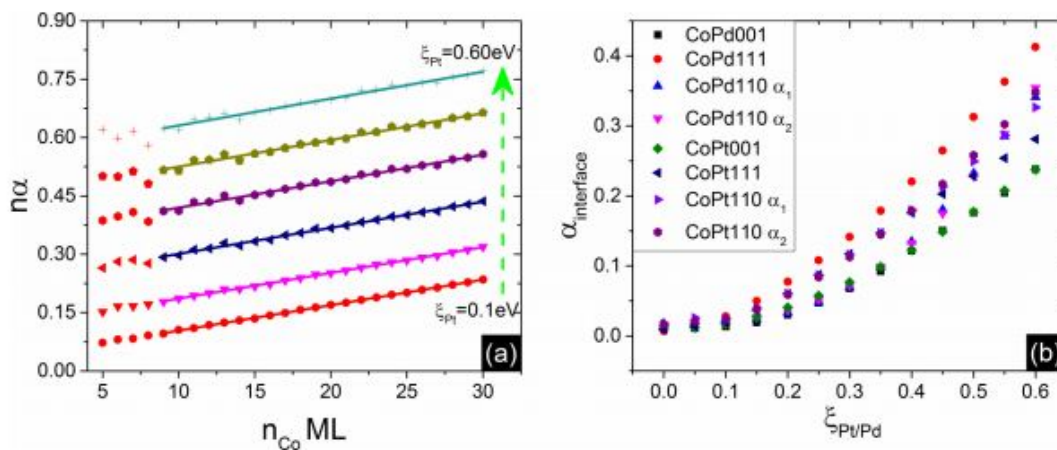
Figure 4.14: (a) The product of the number of Co layers and the damping constant versus the number of Co layers in superlattice Co/Pt[111]. The ξ_{Pt} varies in the range of 0.1eV to 0.60eV with a step of 0.1eV. (b) the summary of the interfacial damping vs the SOI strength in non-magnetic material in superlattices oriented in various directions. The superlattices are multiple Co layers deposited on six Pt or Pd layers.

than the SOI source in non-magnetic metals, as shown in the difference of the two systems Co/Pd and Co/Pt.
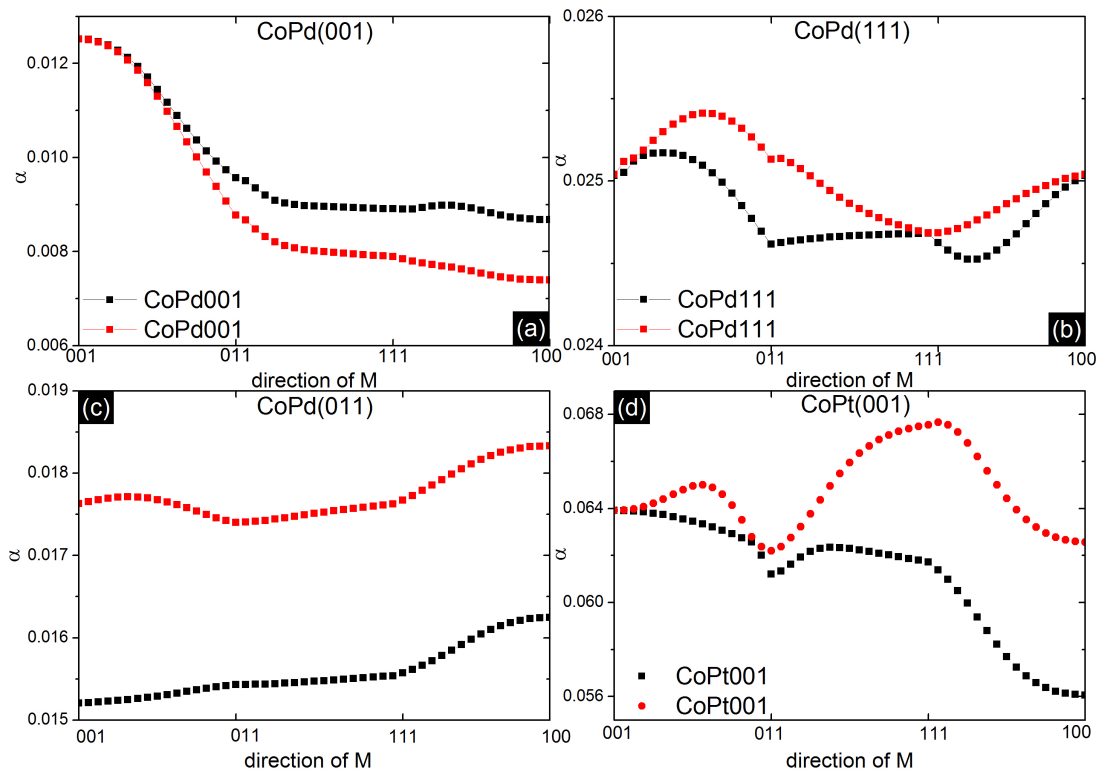
Figure 4.15: The eigenvalues of the damping tensor versus the spin orientation in superlattice (a) Co/Pd[001], (b)Co/Pd[111], (c) Co/Pd[011] and (d) Co/Pt[001]. The superlattices are all six Co monolayers deposited on six Pt or Pd monolayers. The dots of two different colors represent the damping eigenvalues in the two transverse directions perpendicular to the spin orientation.

4.5   Conclusion

For bulk bcc Fe, we extend the calculation of Steiauf and Fahnles to include both intraband and interband damping, which are demonstrated to exhibit very

different angular dependences. We find that the overall damping in the usually examined $< 100 >$ direction is 3/4 the $< 111 >$ direction. Moreover, a tensor is necessary to describe damping in directions other than the two highly symmetric directions above, yielding both parallel and perpendicular torque. We also find that the dependence of α on Fermi level closely follows the exponent of the DOS at the Fermi level.

We calculated the intrinsic damping of the intriguing high anisotropy materials-CoPt, FePt, FePd, and CoPd in both $L1_0$ ordered and disordered structures. In the ordered phase, these four typical alloys all exhibit minimum damping values around room temperature. CoPt has the maximum damping of 0.067 and FePd has the minimum value of 0.009. The calculated damping value of FePt 0.02 agrees well with experiment. The main contribution to the damping is from SOI of the 3d elements in Pd-based alloys. This role changes in the Pt-based alloys because the SOI strength in the non-3d element is larger than 0.29 eV. Artificially shifting E_f, as might be accomplished by doping with impurity atoms, shows that α follows the density of states at E_f in these four $L1_0$ alloys. When defects are introduced, the damping increases with reduced degree of chemical order, due to the increase of spin-flip channels allowed by the broken symmetry. The calculated damping value of partially ordered material FePd is very close to measurement. The intraband damping shows the opposite trend because the ordered phase has

more spin channels at large values of the torque operator Γ^-.

For superlattices Co/Pt and Co/Pd, the interfacial damping is identified, considering typical experimental realizable orientations [001], [111] and [011]. The interfacial damping is related to the lattice orientation: [001] orientation exhibits lower interfacial damping than the other two orientations in both systems. This damping is caused by the broken symmetry at the interface and the spin-orbit interactions of the non-magnetic materials in the superlattice, thus the interfacial damping is inevitable as a consequence of generating high perpendicular anisotropy with ultra-thin film structures for use in spintronic applications. The damping is strongly correlated with the DOS around the Fermi level due to the spin scattering channel. It is also dependent on the spin orientation: the energy dissipation of out-of-plane magnetization can be 1.7 times larger than that of in-plane magnetization. This angular dependent damping can impact the spin dynamics, in both switching and spin oscillation, compared to the classical invariant damping constant.

Chapter 5

Conclusion and Discussion

In the final chapter of this thesis, the results presented in the previous chapters are summarized. We obtained nonlinear angular dependence for the giant magnetoresistance in a trilayer structure with current perpendicular to plane. This nonlinearity can be quantitatively explained by reflected electrons, which could be the origin of the extra noise in common transducers. The extension of the multiple reflection model is consistent with magnetoresistance measurement of multilayer nanowires. We explored the synchronization requirements for non-identical multi spintronic oscillators fabricated in experiment and demonstrated the power enhancement and noise decrease for synchronized states over a temperature range. With the introduction of a combined electric and magnetic coupling effect, an optimized nanopillar structure feasible for thin-film deposition technique was designed.

This optimization can decrease required MR ratio to achieve synchronization. We predicted the energy dissipation constant for many novel spintronic materials and determined the dynamic time scale of spintronic devices for multiple applications, like superlattices and $L1_0$ alloys. We identified the impact of the inevitable experimental defects on the energy dissipation and explained the experimental damping divergence among investigators due to the material degree of order. The defects were found to increase the measured damping value, due to the increase in spin flip scattering channels. We proved the predicted damping constant was consistent with experimental measurement by time-resolved magneto-optic Kerr effect. We explored the interfacial contribution to the energy damping constant in potential superlattices and heterostructures for spintronic devices.

References

[1] R. C. O'Handley. *Modern Magnetic materials: Principles and Applications.* 2000.

[2] Claude Chappert, Albert Fert, and Frdric Nguyen Van Dau. The emergence of spin electronics in data storage. *Nature Materials*, 6:813, 2007.

[3] Y. M. Lee, J. Hayakawa, S. Ikeda, F. Matsukura, and H. Ohno. Effect of electrode composition on the tunnel magnetoresistance of pseudo-spin-valve magnetic tunnel junction with a MgO tunnel barrier. *Appl. Phys. Lett.*, 90:212507, 2007.

[4] P. M. Braganca, I. N. Krivorotov, O. Ozatay, A. G. F. Garcia, N. C. Emley, J.C. Sankey, D.C. Ralph, and R. A. Buhrman. Reducing the critical current for short-pulse spin-transfer switching of nanomagnets. *Appl. Phys. Lett.*, 87:112507, 2005.

[5] S. Sugahara and J. Nitta. Spin-transistor electronics: An overview and outlook. *Proc. IEEE*, 98:21242154, 2010.

[6] A. Brataas, A. D. Kent, and H Ohno. Current-induced torques in magnetic materials. *Nat. Mater.*, 11:372, 2012.

[7] Luqiao Liu, Takahiro Moriyama, D. C. Ralph, and R. A. Buhrman. Spin-torque ferromagnetic resonance induced by the spin hall effect. *Phys. Rev. Lett.*, 106:036601, 2011.

[8] L. Frangou, S. Oyarzún, S. Auffret, L. Vila, S. Gambarelli, and V. Baltz. Enhanced spin pumping efficiency in antiferromagnetic irmn thin films around the magnetic phase transition. *Phys. Rev. Lett.*, 116:077203, 2016.

[9] A. Yu. Dobin and R. H. Victora. Surface roughness induced extrinsic damping in thin magnetic films. *Phys. Rev. Lett.*, 92:257204, 2004.

[10] A. Yu. Dobin and R. H. Victora. Intrinsic nonlinear ferromagnetic relaxation in thin metallic films. *Phys. Rev. Lett.*, 90:167203, 2003.

[11] S. Dubois, J.M. Beuken, L. Piraux, J.L. Duvail, A. Fert, J.M. George, and J.L. Maurice. Perpendicular giant magnetoresistance of NiFe/Cu and Co/Cu multilayered nanowires. *J. Magn. Magn. Mater.*, 165:30, 1997.

[12] F. Schwabl. *Advanced Quantum Mechanics*. Springer, 2008.

[13] W. Heisenberg. Zur theorie des ferromagnetismus. *Z. Phys*, 49(619), 1928.

[14] H. X. Yang, M. Chshiev, B. Dieny, J. H. Lee, A. Manchon, and K. H. Shin. First-principles investigation of the very large perpendicular magnetic anisotropy at Fe|MgO and Co|MgO interfaces. *Phys. Rev. B*, 84:054401, Aug 2011.

[15] K. H. Khoo, G. Wu, M. H. Jhon, M. Tran, F. Ernult, K. Eason, H. J. Choi, and C. K. Gan. First-principles study of perpendicular magnetic anisotropy in CoFe/MgO and CoFe/Mg$_3$B$_2$O$_6$ interfaces. *Phys. Rev. B*, 87:174403, May 2013.

[16] M. N. Baibich, J. M. Broto, A. Fert, F. Nguyen Van Dau, F. Petroff, P. Etienne, G. Creuzet, A. Friederich, and J. Chazelas. Giant magnetoresistance of (001)Fe/(001)Cr magnetic superlattices. *Phys. Rev. Lett.*, 61:2472–2475, Nov 1988.

[17] T. Valet and A. Fert. Theory of the perpendicular magnetoresistance in magnetic multilayers. *Phys. Rev. B*, 48:7099, 1993.

[18] Stuart S. P. Parkin, Christian Kaiser, Alex Panchula, Philip M. Rice, Brian

Hughes, Mahesh Samant, and See-Hun Yang. Giant tunnelling magnetoresistance at room temperature with MgO (100) tunnel barriers. *Nature Materials*, 3:862, 2004.

[19] Shinji Yuasa, Taro Nagahama, Akio Fukushima, Yoshishige Suzuki, and Koji Ando. Giant room-temperature magnetoresistance in single-crystal Fe/MgO/Fe magnetic tunnel junctions. *Nature Materials*, 3:868, 2004.

[20] J. Mathon and A. Umerski. Theory of tunneling magnetoresistance of an epitaxial Fe/MgO/Fe(001) junction. *Phys. Rev. B*, 63:220403.

[21] J. C. Slonczewski. Current-driven excitation of magnetic multilayers. *J. Magn. Magn. Mater*, 159:L1, 1996.

[22] L. Berger. Emission of spin waves by a magnetic multilayer traversed by a current. *Phys. Rev. B*, 54:9353, 1996.

[23] E. B. Myers, D. C. Ralph, J.A. Katine, R. N. Louie, and R. A. Buhrman. Current-induced switching of domains in magnetic multilayer devices. *Science*, 285:867, 1999.

[24] J. A. Katine, F. J. Albert, R. A. Buhrman, E.B. Myers, and D.C. Ralph. Current-driven magnetization reversal and spin-wave excitations in Co /Cu /Co pillars. *Phys. Rev. Lett.*, 84:3149, 2000.

[25] L. Landau and E. Lifshitz. On the theory of the dispersion of magnetic permeability in ferromagnetic bodies. *Phys. Z. Sowjetunion*, 8:153, 1935.

[26] T. L. Gilbert. A phenomenological theory of damping in ferromagnetic materials. *IEEE Trans. Magn.*, 40:3443, 2004.

[27] J. C. Slonczewski. *J. Magn. Magn. Mater.*, 247:324, 2002.

[28] C. Chappert, K. Le Dang, P. Beauvillain, H. Hurdequint, and D. Renard. Ferromagnetic resonance studies of very thin cobalt films on a gold substrate. *Phys. Rev. B*, 34:3192, 1986.

[29] M. Sparks, R. Loudon, and C. Kittel. Ferromagnetic relaxation. i. theory of the relaxation of the uniform precession and the degenerate spectrum in insulators at low temperatures. *Phys. Rev.*, 122:791, 1961.

[30] A. Fert and L. Piraux. Magnetic nanowires. *J. Magn. Magn. Mater.*, 200:338, 1999.

[31] K. Nakamoto, H. Hoshiya, H. Katada, K. Hoshino, and Jeffrey Childress. CPPGMR heads with a current screen layer for 300 Gb/in^2 recording. *IEEE Trans. Magn.*, 44:95, 2008.

[32] X. Huang and B. J. H. Stadler. Magnetoresistance and spin transfer torque in electrodeposited Co/Cu multilayered nanowire arrays with small diameters. *J. Appl. Phys.*, 105:07D128, 2009.

[33] P. Dauguet, P. Gandit, J. Chaussy, S. F. Lee, A. Fert, and P. Holody. Angular dependence of the perpendicular giant magnetoresistance of multilayers. *Phys. Rev. B*, 54:1083, 1996.

[34] S. Urazhdin, R. Loloee, and W. P. Pratt. Noncollinear spin transport in magnetic multilayers. *Phys. Rev. B*, 71:100401, 2005.

[35] S. Datta. *Electronic Transport in Mesoscopic Systems*. Cambridge University Press, 1997.

[36] S. Hernandez and R. H. Victora. Calculation of spin transfer torque in partially polarized spin valves including multiple reflections. *Appl. Phys. Lett.*, 97:062506, 2010.

[37] D. S. Fisher. Relation between conductivity and transmission matrix. *Phys. Rev. B*, 23:6851, 1981.

[38] R. Meservey et al. Correlation between spin polarization of tunnel currents from 3d ferromagnets and their magnetic moments. *Phys. Rev. Lett.*, 37:858, 1976.

[39] R. J. Soulen et al. Measuring the spin polarization of a metal with a super-conducting point contact. *Science*, 282:85, 1998.

[40] L. Bocklage et al. Spin polarization of Ni_2MnIn and $Ni_{80}Fe_{20}$ determined by point-contact andreev spectroscopy. *J. Appl. Phys.*, 101:09J512, 2007.

[41] K. Liu et al. Perpendicular giant magnetoresistance of multilayered Co/Cu nanowires. *Phys. Rev. B*, 51:7381, 1995.

[42] S. Hernandez, L. Tan, B. J. H. Stadler, and R. H. Victora. Micromagnetic calculation of spin transfer torque in Co/Cu multilayer nanowires. *J. Appl. Phys.*, 109:07C916, 2011.

[43] W. H. Rippard, M. R. Pufall, S. Kaka, S. E. Russek, and T. J. Silva. Direct-current induced dynamics in $Co_{90}Fe_{10}/Ni_{80}Fe_{20}$ point contacts. *Phys. Rev. Lett*, 92:027201, 2004.

[44] S. Kiselev et al. Microwave oscillations of a nanomagnet driven by a spin-polarized current. *Nature*, 425:380, 2003.

[45] B. Georges et al. Origin of the spectral linewidth in nonlinear spin-transfer oscillators based on mgo tunnel junctions. *Phys. Rev. B*, 80:060404, 2009.

[46] T. J. Slavin and V. Tiberkevich. Nonlinear auto-oscillator theory of microwave generation by spin-polarized current. *IEEE Trans. Magn*, 45:1875, 2009.

[47] S. Yuasa, A. Fukushima, H. Kubota, Y. Suzuki, and K. Ando. Giant tunneling magnetoresistance up to 410% at room temperature in fully epitaxial Co/MgO/Co magnetic tunnel junctions with BCC Co(001) electrodes. *Appl. Phys. Lett.*, 89:042505, 2006.

[48] Yuasa Y. et al. Spin-torque induced rf oscillation in magnetic tunnel junctions with an Fe-rich CoFeB free layer. *J. Phys.: Conf. Ser.*, 266:012098, 2011.

[49] Ruotolo A. et al. Phase-locking of magnetic vortices mediated by antivortices. *Nature Nanotech*, 4:528, 2009.

[50] Kaka S. et al. Mutual phase-locking of microwave spin torque nano-oscillators. *Nature*, 437:389, 2005.

[51] X. Chen and Victora. Phase locking of spin-torque oscillators by spin-wave interactions. *Phys. Rev. B*, 79:180402, 2009.

[52] J. Grollier, V. Cros, and A. Fert. Synchronization of spin-transfer oscillators driven by stimulated microwave currents. *Phys. Rev. B*, 73:060409, 2006.

[53] W. F. Brown. Thermal fluctuations of a single-domain particle. *Phys. Rev.*, 130:1677, 1963.

[54] C. Bowick. *RF Circuit Design 2nd edn.* Newnes, 2007.

[55] Dubois S. et al. Evidence for a short spin diffusion length in permalloy from the giant magnetoresistance of multilayered nanowires. *Phys. Rev. B*, 60:477, 1999.

[56] H. Sakaguchi and Y. Kuramoto. A soluble active rotater model showing phase transitions via mutual entertainment. *Theor. Phys.*, 76:576, 1986.

[57] G. Bertotti, I. D. Mayergoyz, and C. Serpico. Spin-wave instabilities in large-scale nonlinear magnetization dynamics. *Phys. Rev. Lett.*, 87:217203, 2001.

[58] H. Suhl. *IEEE Trans. Magn.*, 34(1834), 1998.

[59] W. A. Challener, C. Peng, A. V. Itagi, D. Karns, W. Peng, Y. Peng, X. Yang, X. Zhu, N. J. Gokemeijer, Y. T. Hsia, G. Ju, R. E. Rottmayer, M. A. Seigler, and E. C. Gage. Heat-assisted magnetic recording by a near-field transducer with efficient optical energy transfer. *Nat. Photonics*, 3(220), 2009.

[60] Y. Jiao, Z. Liu, and R. H. Victora. Renormalized anisotropic exchange for representing heat assisted magnetic recording media. *J. Appl. Phys.*, 117:17E317, 2015.

[61] S. Okamoto, N. Kikuchi, and O. Kitakami. Magnetization switching behavior with microwave assistance. *Appl. Phys. Lett.*, 93(102506), 2008.

[62] T. Seki, S. Mitani, K. Yakushiji, and K. Takanashi. Spin-polarized current-induced magnetization reversal in perpendicularly magnetized $L1_0$-FePt layers. *Appl. Phys. Lett.*, 88(172504), 2006.

[63] A. Misra and R. H. Victora. Ferromagnetic relaxation by magnon-induced currents. *Phys. Rev. B*, 73:172414, 2006.

[64] V. Kambersky. On ferromagnetic resonance damping in metals. *Czech. J. Phys.*, 26:1366, 1976.

[65] K. Gilmore, Y. U. Idzerda, and M. D. Stiles. Identification of the dominant precession-damping mechanism in Fe, Co, and Ni by first-principles calculations. *Phys. Rev. Lett.*, 99:027204, 2007.

[66] K. Gilmore, Y. U. Idzerda, and M. D. Stiles. Spin-orbit precession damping in transition metal ferromagnets. *J. Appl. Phys.*, 103:07D303, 2008.

[67] K. Gilmore, M. D. Stiles, J. Seib, D. Steiauf, and M. Fahnle. Anisotropic damping of the magnetization dynamics in Ni, Co, and Fe. *Phys. Rev. B*, 81:174414, 2010.

[68] T. Qu and R. H. Victora. Dependence of kambersky damping on fermi level and spin orientation. *J. Appl. Phys.*, 115:17C506, 2014.

[69] E. Barati, M. Cinal, D. M. Edwards, and A. Umerski. Gilbert damping in magnetic layered systems. *Phys. Rev. B*, 90:014420, Jul 2014.

[70] S. Mankovsky, D. Kodderitzsch, G. Woltersdorf, and H. Ebert. First-principles calculation of the gilbert damping parameter via the linear response formalism with application to magnetic transition metals and alloys. *Phys. Rev. B*, 87:014430, 2013.

[71] A. A. Starikov, P. J. Kelly, A. Brataas, Y. Tserkovnyak, and G. E. Bauer. Unified first-principles study of gilbert damping, spin-flip diffusion, and resistivity in transition metal alloys. *Phys. Rev. Lett.*, 105:236601, 2010.

[72] C. H. Back, R. Allenspach, W. Weber, S. S. P. Parkin, D. Weller, E. L. Garwin, and H. C. Siegmann. Minimum field strength in precessional magnetization reversal. *Science*, 285(5429):864–867, 1999.

[73] A. Ghosh, S. Auffret, U. Ebels, and W. E. Bailey. *Phys. Rev. Lett.*, 109(127202), 2012.

[74] H. T. Nembach, J. M. Shaw, C. T. Boone, and T. J. Silva. *Phys. Rev. Lett.*, 110(117201), 2013.

[75] R. Urban, G. Woltersdorf, and B. Heinrich. *Phys. Rev. Lett.*, 87(217204), 2001.

[76] B. C. Choi, M. Belov, W. K. Hiebert, G. E. Ballentine, and M. R. Freeman. Ultrafast magnetization reversal dynamics investigated by time domain imaging. *Phys. Rev. Lett.*, 86:728–731, Jan 2001.

[77] Z. Liu and R. H. Victora. *IEEE Transactions on Magnetics*, PP:99, 2016.

[78] V. L. Moruzzi, J. F. Janak, and A. R. Williams. *Calculated Electronic Properties of Metals.* Pergamon Press, Inc., 1978.

[79] A. M. Oles and G. Stollhoff. Correlation effects in ferromagnetism of transition metals. *Phys. Rev. B*, 29:314, 1984.

[80] G. T. Rado, H. Suhl, and C. Herring. *Exchange Interactions among Itinerant Electrons.* Academic Press, New York, 1966.

[81] G. H. O. Daalderop and P. J. Kelly andM. F. H. Schuurmans. Magnetocrystalline anisotropy and orbital moments in transition-metal compounds. *Phys. Rev. B*, 44:12054, 1991.

[82] N. Inami, G. Kim, T. Hiratsuka, H. Naganuma, M. Oogane, and Y. Ando. Structural, magnetic, and magnetotransport properties of FePt/MgO/CoPt perpendicularly magnetized tunnel junctions. *J. Phys.: Conf. Ser.*, 200:052008, 2010.

[83] D. Steiauf and M. Fahnle. Damping of spin dynamics in nanostructures: An ab initio study. *Phys. Rev. B*, 72:064450, 2005.

[84] A. Sakuma. First-principles study on the gilbert damping constants of transition metal alloys, Fe-Ni and Fe-Pt systems. *J. Phys. Soc. Jpn.*, 81:084701, 2012.

[85] D. Weller, A. Moser, L. Folks, M. Best, W. Lee, M. F. Toney, M. Schwickert, J. U. Thiele, and M. Doerner. High K_u materials approach to 100 Gbits/in^2. *IEEE Trans. Magn.*, 36:10, 2000.

[86] T. Klemmer, D. Hoydick, H. Okumura, B. Zhang, and W. A. Soffa. Magnetic hardening and coercivity mechanisms in L1$_0$ ordered FePd ferromagnets. *Scr. Metall. Mater.*, 33:1793, 1995.

[87] K. M. Seemann, Y. Mokrousov, A. Aziz, J. Miguel, F. Kronast, W. Kuch, M. G. Blamire, A. T. Hindmarch, B. J. Hickey, I. Souza, and C. H. Marrows. Spin-orbit strength driven crossover between intrinsic and extrinsic mechanisms of the anomalous hall effect in the epitaxial $L1_0$-ordered ferromagnets FePd and FePt. *Phys. Rev. Lett.*, 104:076402, 2010.

[88] A. Barman, S. Wang, O. Hellwig, A. Berger, E. E. Fullerton, and H. Schmidt. Ultrafast magnetization dynamics in high perpendicular anisotropy $[Co/Pt]_n$ multilayers. *J. Appl. Phys.*, 101:09D102, 2007.

[89] G. Malinowski, K. C. Kuiper, R. Lavrijsen, H. J. M. Swagten, and B. Koopmans. Magnetization dynamics and gilbert damping in ultrathin $Co_{48}Fe_{32}B_{20}$ films with out-of-plane anisotropy. *Appl. Phys. Lett.*, 94:102501, 2009.

[90] S. Mizukami, E. P. Sajitha, D. Watanabe, F. Wu, T. Miyazaki, H. Naganuma, M. Oogane, and Y. Ando. Gilbert damping in perpendicularly magnetized Pt/Co/Pt films investigated by all-optical pump-probe technique. *Appl. Phys. Lett.*, 96:152502, 2009.

[91] P. He, X. Ma, J. W. Zhang, H. B. Zhao, G. Lupke, Z. Shi, and S. M. Zhou. Quadratic scaling of intrinsic gilbert damping with spin-orbital coupling in

L1$_0$ FePdPt films: Experiments and ab initio calculations. *Phys. Rev. Lett.*, 110:077203, 2013.

[92] S. Mizukami, S. Iihama, N. Inami, T. Hiratsuka, G. Kim, H. Naganuma, M. Oogane, and Y. Ando. Fast magnetization precession observed in L1$_0$-FePt epitaxial thin film. *Appl. Phys. Lett.*, 98:052501, 2011.

[93] Z. Chen, M. Yi, M. Chen, S. Li, S. Zhou, and T. Lai. Spin waves and small intrinsic damping in an in-plane magnetized FePt film. *Appl. Phys. Lett.*, 101:222402, 2012.

[94] X. Ma, L. Ma, P. He, H. B. Zhao, S. M. Zhou, and G. Lupke. Role of antisite disorder on intrinsic gilbert damping in L1$_0$ FePt films. *Phys. Rev. B*, 91:014438, 2015.

[95] A. B. Shick and O. N. Mryasov. Coulomb correlations and magnetic anisotropy in ordered L1$_0$ CoPt and FePt alloys. *Phys. Rev. B.*, 67:172407, 2003.

[96] S. Iihama, S. Mizukami, N. Inami, T. Hiratsuka, G. Kim, H. Naganuma, M. Oogane, T. Miyazaki, and Y. Ando. *Jpn. J. Appl. Phys.*, 52:073002, 2013.

[97] T. Kawai, A. Itabashi, M. Ohtake, S. Takeda, and M. Futamoto. Observation of precessional magnetization dynamics in $L1_0$-FePt thin films with different $L1_0$ order parameter values. *EPJ Web Conf.*, 75:02002, 2014.

[98] M. N. Baibich, J. M. Broto, A. Fert, F. Nguyen Van Dau, F. Petroff, P. Etienne, G. Creuzet, A. Friederich, and J. Chazelas. *Phys. Rev. Lett.*, 61:2472, 1988.

[99] T. Miyazaki and N. Tezuka. *J. Magn. Magn. Mater.*, 139:L231, 1995.

[100] J. S. Moodera, L. R. Kinder, T. M. Wong, and R. Meservey. *J. Magn. Magn. Mater.*, 74:3273, 1995.

[101] P. Grünberg, R. Schreiber, Y. Pang, M. B. Brodsky, and H. Sowers. Layered magnetic structures: Evidence for antiferromagnetic coupling of Fe layers across Cr interlayers. *Phys. Rev. Lett.*, 57:2442, 1986.

[102] S. S. P. Parkin, N. More, and K. P. Roche. Oscillations in exchange coupling and magnetoresistance in metallic superlattice structures: Co/Ru, Co/Cr, and Fe/Cr. *Phys. Rev. Lett.*, 64:2304, 1990.

[103] W. B. Zeper, J. A. M. Greidanus, P. F. Carcia, and C. R. Fincher. *J. Appl. Phys.*, 65:4971, 1989.

[104] C. H. Lee, R. F. C. Farrow, C. J. Lin, E. E. Marinero, and C. J. Chien. Molecular-beam-epitaxial growth and magnetic properties of Co-Pt super-lattices oriented along the [001], [110], and [111] axes of Pt. *Phys. Rev. B*, 42:11384–11387, Dec 1990.

[105] Brad N. Engel, Craig D. England, Robert A. Van Leeuwen, Michael H. Wiedmann, and Charles M. Falco. Interface magnetic anisotropy in epitaxial superlattices. *Phys. Rev. Lett.*, 67:1910–1913, Sep 1991.

[106] R. H. Victora and J. M. MacLaren. Theory of magnetic interface anisotropy. *Phys. Rev. B*, 47:11583–11586, May 1993.

[107] J. M. MacLaren and R. H. Victora. Theoretical predictions of inter-face anisotropy in the presence of interdiffusion (invited). *J. Appl. Phys.*, 76(6069), 1994.

[108] S. M. Bhagat and P. Lubitz. Temperature variation of ferromagnetic relax-ation in the 3d transition metals. *Phys. Rev. B*, 10:179–185, Jul 1974.

[109] J. Li, M. Przybylski, F. Yildiz, X. D. Ma, and Y. Z. Wu. Oscillatory mag-netic anisotropy originating from quantum well states in fe films. *Phys. Rev. Lett.*, 102:207206, 2009.

[110] U. Bauer, M. Dabrowski, M. Przybylski, and J. Kirschner. Experimental confirmation of quantum oscillations of magnetic anisotropy in co/cu(001). *Phys. Rev. B*, 84:144433, 2011.

[111] D. M. Edwards, J. Mathon, R. B. Muniz, and M. S. Phan. Oscillations of the exchange in magnetic multilayers as an analog of de haasvan alphen effect. *Phys. Rev. Lett.*, 67:1476, 1991.

[112] L. Szunyogh, B. Ujfalussy, C. Blaas, U. Pustogowa, C. Sommers, and P. Weinberger. Oscillatory behavior of the magnetic anisotropy energy in $Cu(100)/Co_n$ multilayer systems. *Phys. Rev. B*, 56:14036, 1997.

[113] D M Edwards. The absence of intraband scattering in a consistent theory of gilbert damping in pure metallic ferromagnets. *Journal of Physics: Condensed Matter*, 28(8):086004, 2016.